Delft University of Technology
Design Synthesis Exercise

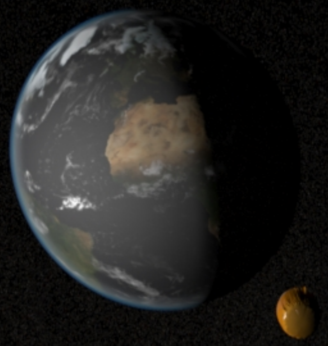

Design of a Controllable Inflatable Aeroshell

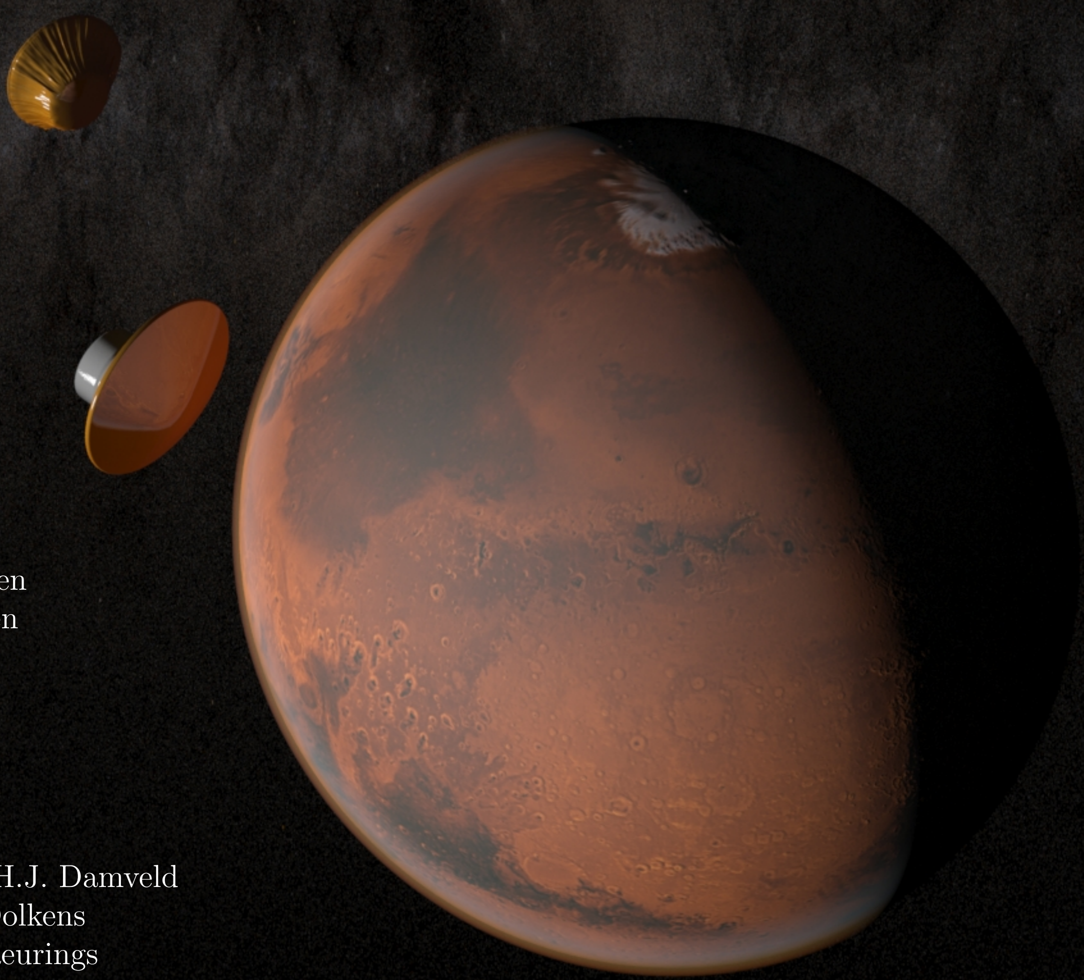

S. Balasooriyan
B.R. van Dongen
D.D. Hage
T. Keijzer
G. van Koppenhagen
L.C.J.M. Mathijssen
J.F. Meulenbeld
A.P. van Oostrum
S.P.C. van Schie

Tutor: Dr. ir. H.J. Damveld
Coaches: Ir. D. Dolkens
Ir. N. Reurings

June 30, 2015

Preface

June 30, 2015

Dear reader,

A growing interest in manned spaceflight and human exploration of Mars requires a new solution. Conventional, rigid entry solutions require a significant decelerator mass to bring the payload to ground. Inflatable concepts, on the other hand, offer significant mass and packaging advantages and their application opens up broad possibilities for interplanetary human spaceflight.

This Final Report centres around the analysis and design of a Controllable Inflatable Aeroshell that is capable of bringing two crew members to the Martian surface with a mere 10% decelerator mass fraction within 10 days. Conceptual and preliminary design have shown the feasibility of such a mission with its corresponding economical benefits and reduced ecological footprint by a decreased required number of launches through increased payload-carrying capability.

We would like to acknowledge dr. ir. H.J. Damveld, ir. D. Dolkens and ir. N. Reurings for their guidance and support. Moreover, we would like to thank all other staff members of the Delft University of Technology that have been of assistance.

Design Synthesis Exercise Group 02

Summary

There is an increasing demand for carrying human payload to the surface of Mars, and inflatable aeroshell concepts hold the key to what is currently unattainable for interplanetary human spaceflight. In the wake of current NASA investigations on the feasibility of inflatable decelerators for hypersonic guidable entry, this study focuses on the preliminary design of a controllable Mars entry vehicle with a payload mass of at least $9000\,[kg]$ using an inflatable aerodynamic decelerator of at most $1000\,[kg]$. Such a solution provides a large economical advantage over conventional solutions by maximizing payload-carrying capability through a lightweight device less burdened by launcher size considerations. Altogether, the objective is to design an Controllable Inflatable Aeroshell (CIA) for a spacecraft capable of carrying human payload to Mars.

To aid in the design of such a vehicle several tools have been developed with the following purposes:

- A tool for parametric structural mass modelling
- A modified Newtonian flow aerodynamic tool for the characterisation of aerodynamic and aero-thermal behaviour and shape optimisation
- A thermal model for Thermal Protection System sizing and analysis
- A trajectory tool with an implemented control system for trajectory control

This results in a vehicle that has an undeployed diameter of $5\,[m]$ and a deployed diameter of $12\,[m]$. It is designed for an entry velocity of $7\,[km \cdot s^{-1}]$ and a final velocity of Mach $5\,[-]$ at $15\,[km]$ altitude within a horizontal precision range of $500\,[m]$. To this extent the $10\,000\,[kg]$ vehicle has an aerodynamic decelerator mass of $928\,[kg]$ including contingency. Due to the human payload the mission is sized for an acceleration below $3g_e$. Furthermore, the maximum aerocapture and entry phase duration is 10 days, where two periods of aerodynamic deceleration exist. During both manoeuvres, aerocapture and entry, the vehicle will spend up to $800\,[s]$ in the Martian atmosphere. In between aerocapture and entry the vehicle will be placed in a parking orbit. The vehicle adheres to Committee on Space Research (COSPAR) regulations and has a control system reliability of $0.9995\,[-]$.

A key feature of the CIA is its asymmetric, skewed shape. The asymmetry follows from aerodynamic optimisation and yields higher lift-generating capability at lower angles of attack to firstly achieve more lift and secondly require smaller angles of attack to keep the crew module from being exposed by the flow. Aerodynamic performance is characterised by a 0.35 lift-to-drag ratio and a $22.5\,[deg]$ trim angle of attack.

The asymmetry is adopted by the structural shape through stitching of ten inflatable toroids at a variable half-cone angle with respect to one another. Structural rigidity under an ultimate aerodynamic pressure of $3500\,[Pa]$ is ensured by the use of a nitrogen blow-down system that inflates five bladder volumes at $169\,[kPa]$, which keeps the flexible bladder material in tension to prevent compressive wrinkling. Resulting loads are carried by woven PBO Zylon® fibres of $0.125\,[mm]$ thickness at a $95\,[kg]$ mass. At a minimum half-cone angle, the structural mass is estimated at $300\,[kg]$.

The Thermal Protection System is exposed to a peak heat flux of $21\,[W \cdot cm^{-2}]$ and a peak temperature of $1376\,[K]$ during aerocapture. This thermal loading is withstood

by a multi-material lay-up 256 $[kg]$ consisting of a state-of-the-art Nicalon^{TM} barrier of 0.51 $[mm]$ thickness and Pyrogel® 6650 insulator of 2.4 $[mm]$ thickness, complemented by dual 25 $[\mu m]$ Kapton gas barriers.

Compatibility of the CIA with a manned Mars mission is ensured by preliminary crew module and mission design. The crew module accommodates two crew members for a 100-day interplanetary mission and its mass is estimated at 9000 $[kg]$. Return from Mars requires two launches prior to crew module launch, which bring the Mars Ascent Vehicle onto Mars and an Earth Return Vehicle in an orbit around Mars. Mission cost is estimated at 44 billion US dollars.

Recommendations are a propagation of design on decelerator and crew module, testing activities, and crew and mission preparation thereafter. Key driver for further design is concept reliability. Deployment, inflation and terminal descent are critical mission phases and inherently unreliable for a CIA design. These therefore require particular attention in future design.

Contents

Acronyms

ADCS Attitude Determination & Control Subsystem.

APC Analytical Predictor-Corrector.

BPSK Binary Phase-Shift Keying.

C&DH Command & Data Handling.

CAD Computer Aided Design.

CG Centre of Gravity.

CIA Controllable Inflatable Aeroshell.

COSPAR Committee on Space Research.

DSN Deep Space Network.

ECLSS Environmental Control and Life Support System.

EDL Entry, Descent & Landing.

ERV Earth Return Vehicle.

ESA European Space Agency.

ESOC European Space Operations Centre.

FEM Finite Element Method.

HDRM Hold-Down and Release Mechanism.

HIAD Hypersonic Inflatable Aerodynamic Decelerator.

IMU Inertial Measurement Unit.

IRVE Inflatable Re-entry Vehicle Experiment.

LEO Low Earth Orbit.

Mars-GRAM Mars-Global Reference Atmospheric Model 2010 v1.0.

MAV Mars Ascent Vehicle.

MEMS Micro-Electro-Mechanical Systems.

MOLA Mars Orbiter Laser Altimeter.

NASA National Aeronautics and Space Administration.

NPC Numerical Predictor-Corrector.

NTO Nitrogen Tetroxide.

QPSK Quadrature Phase-Shift Keying.

RAMS Reliability, Availability, Maintainability and Safety.

SLS Space Launch System.

SPF Single Point of Failure.

SWOT Strengths, Weaknesses, Opportunities and Threats.

TCS Thermal Control System.

THOR Terrestrial HIAD Orbital Re-entry.

TPS Thermal Protection System.

TRL Technology Readiness Level.

US United States.

List of Symbols

Symbol	Unit	Description
A	$[m^2]$	Area
$\mathbf{a}$	$[m \cdot s^{-2}]$	Acceleration (vector)
C_D	$[-]$	Drag coefficient
C_L	$[-]$	Lift coefficient
C_M	$[-]$	Moment coefficient around pitch axis
C_{M_α}	$[rad^{-1}]$	Moment coefficient gradient around y-axis
c_p	$[J \cdot kg^{-1} \cdot K^{-1}]$	Specific heat capacity
C_p	$[-]$	Pressure coefficient
C_X	$[-]$	Longitudinal force coefficient in the body frame
d	$[m]$	Force moment arm
D	$[N]$	Drag
D_o	$[m]$	Deployed diameter
f	$[N \cdot m^{-1}]$	Running load
$\mathbf{F}$	$[N]$	Force vector
h	$[m]$	Height
H	$[N \cdot m \cdot s^{-1}]$	Angular Momentum
I_{sp}	$[s]$	Specific impulse
k	$[W \cdot m^{-1} \cdot K^{-1}]$	Thermal conductivity
l	$[m]$	Length
L	$[N]$	Lift
m	$[kg]$	Mass
M	$[-]$	Mach number
M_{aero}	$[N \cdot m]$	Moment due to aerodynamic forces
$\dot{m}$	$[kg \cdot s^{-1}]$	Mass flow
N	$[-]$	Number of toroids
p	$[Pa]$	Pressure
q	$[Pa]$	Dynamic pressure
$\dot{q}$	$[W \cdot m^{-2}]$	Heat flux
r	$[m]$	Local radius of curvature
$\mathbf{R}$	$[m]$	Radius (vector)
t	$[s]$	Time
T	$[K]$	Temperature
V	$[m \cdot s^{-1}]$	Velocity
V	$[m^3]$	Volume
$\mathbf{V}$	$[m \cdot s^{-1}]$	Velocity (vector)
w	$[m]$	Width
x	$[m]$	Depth
α	$[rad]$	Angle of attack

Symbol	Unit	Description
α_d	$[m^2 \cdot s^{-1}]$	Thermal diffusivity
β	$[rad]$	Angle of sideslip
β_{cone}	$[rad]$	Local cross-sectional surface rotation angle
χ	$[rad]$	Local surface inclination angle
ε	$[-]$	Emissivity
γ	$[rad]$	Flight path angle
κ	$[-]$	Ratio of specific heats
μ	$[rad]$	Bank angle
ρ	$[kg \cdot m^{-3}]$	Density
θ	$[rad]$	Pitch angle
θ_{cone}	$[rad]$	Decelerator half-cone angle

List of Constants

Symbol	Value	Unit	Description
g_e	9.81	$[m \cdot s^{-2}]$	Earth gravitational acceleration
R_m	$3.3899 \cdot 10^6$	$[m]$	Mean radius of Mars
σ	$5.670373 \cdot 10^{-8}$	$[W \cdot m^{-2} \cdot K^{-4}]$	Stefan Boltzmann constant

List of Figures

List of Tables

1 Introduction

There is an increasing need to carry humans to the surface of Mars and other extraterrestrial locations. A Controllable Inflatable Aeroshell (CIA) has high potential to fulfil this need by delivering sufficient aerodynamic deceleration at a significantly lower mass fraction: the conventional solution, a rigid aeroshell, may have a hypersonic decelerator mass fraction of up to 30%. Payload-carrying capability can therefore be increased such that the economic feasibility of extraterrestrial exploration and habitation missions is significantly increased. Human interest in space exploration persists and a large number of planned human space flight missions make such a lightweight solution high in demand.

To this end, the study focuses on designing a CIA that brings a vehicle of 10 000 $[kg]$ in a controlled manner to the surface of Mars, a planet with one of the most challenging environments for aerocapture due to its thin atmosphere. Moreover, the vehicle is designed to have a decelerator mass less than ten percent of the total vehicle mass. Comparing this to the conventional mass fraction, it is clear that this is a game-changer. Therefore, the objective of this study is to design an CIA for a spacecraft capable of carrying human payload to Mars.

This Final Report details the result of the preliminary design phase, following upon the concept selection. The best concept was selected from the five researched concepts presented in the Mid-Term Report and was designed and analysed further during the preliminary design phase. In combination with the decelerator system, mission planning has been performed to give a broad overview of the environment the spacecraft is to endure. This is summarised together with the mission requirements and scope, a market analysis, sustainable development strategy and cost breakdown structure in Chapter 2.

During concept selection the stacked toroid was chosen based on its performance with respect to the trade-off criteria, including a significantly higher Technology Readiness Level (TRL) than the other concepts and a far lower mass than the conventional rigid concept. More details on the concept selection and trade-off can be found in Chapter 3. The definition of the system in terms of functions, requirements and subsystems can be found in Chapter 4. To fully understand the complete system and what requirements are imposed on the decelerator, the crew module is sized as well. The crew module design is detailed in Chapter 5.

The orbit is specified such that the maximum deceleration time can be kept, while allowing time in a parking orbit if required by unfavourable atmospheric conditions on Mars. The Thermal Protection System (TPS) is sized using the 1D heat equation, and using state-of-the-art materials resulted in an extremely light lay-up. The inflation structure is sized using a parametric mass model in combination with a truss-based model to estimate internal loads. Aerodynamic performance was estimated using modified Newtonian flow theory, and the shape was optimised to perform according to requirements. These tools, along with design parameter sensitivity, are presented in Chapter 6.

The tools and sensitivity analyses are required to iterate efficiently towards a design that fulfils the requirements. A final design was formulated that complies with requirements. The iterative approach to design and the final result is detailed in Chapter 7.

Finally, recommendations for future work are made, looking at the planning of activities that have to be performed from preliminary design until the end of mission. Also areas of low TRL that require further research are discussed and a strategy for verification and validation is presented.

2 Mission description

This chapter serves to provide on overview of the general mission layout. The mission outline from launch to final return is discussed in Section 2.1. A full mission outline is provided, but the report focuses around the design of a CIA. Ground operations are covered in Section 2.2. The scope of the design is explained in Section 2.3. A short overview of the top level requirements is provided in Section 2.4. A market analysis, the sustainable development strategy and a cost breakdown are provided in Sections 2.5, 2.6 and 2.7 respectively.

2.1 Mission outline

The mission outline is separated in five phases: Launch, interplanetary transfer, aerocapture and entry, terminal descent and return. The design of the CIA is focussed on the aerocapture and entry phase.

2.1.1 Launch

Launch serves to bring the CIA and mission-required vehicles in a transfer orbit towards Mars. From the top-level requirements as summarised in Section 2.4 an entry velocity of $7\,[km \cdot s^{-1}]$ is desired which is an implicit requirement on the total mission duration. Based on this requirement specific launch operations can be considered and additional mission requirements can be considered. Important factors are payload size, loads and required velocity increments. Launch is important to consider in the CIA design as a lot of the system requirements can be traced down to launch.

In order to reach the Martian atmosphere with the desired approach velocity a total velocity increment of about $19.6\,[km \cdot s^{-1}]$ is required. This velocity increment includes the escape velocity of the Earth to its sphere of influence and an additional velocity increment to reach the Martian atmosphere with the required approach velocity.

The velocity increments are typically divided into two parts: a first velocity increment into Low Earth Orbit (LEO) and a second velocity increment into the transfer orbit. Within the LEO separate payload modules the CIA may be joined [7]. The period in LEO also allows for more precisely controlled arrival conditions at Mars as, to a certain extent, the launch is omitted from the timing sequence. Moreover, it widens the launch window.

Important considerations concerning the launch are the encountered vibrations and loads as well as the total mass required to bring into the interplanetary transfer orbit. Launch vibrations should be considered as the natural frequencies of the subsystems should remain above the launch-induced vibrations. This should, for one, be considered for the inflatable part of the decelerator.

Launch loads are typically in the order of 2.8-4.3g_e in longitudinal and 0.9-3g_e in lateral direction [8], which is above the maximum allowed top level deceleration of $3g_e$ into the Martian atmosphere. For this reason launch loads are an important factor for the structural sizing of the CIA and accompanying elements.

A launcher currently being developed for missions to Mars is the Space Launch System (SLS) developed by National Aeronautics and Space Administration (NASA). The SLS features multiple stages and allows for a $5\,[m]$ diameter in line with the top level mission requirements. The SLS features multiple stages able to deliver the required velocity increments. Its design is tailored to the Orion spacecraft which is being developed to, in the future, go to Mars. For the modules featuring a $5\,[m]$ diameter payload the volume is constrained to $225\,[m^3]$ [9].

2.1.2 Interplanetary transfer

The interplanetary transfer time has a big impact on the design. The interplanetary transfer time determines for instance the mass of food for the astronauts, the amount of radiation to endure, how much they need to exercise and more. Keeping the transfer time short will minimise these problems. However it will also increase the ΔV-budget needed for the launcher.

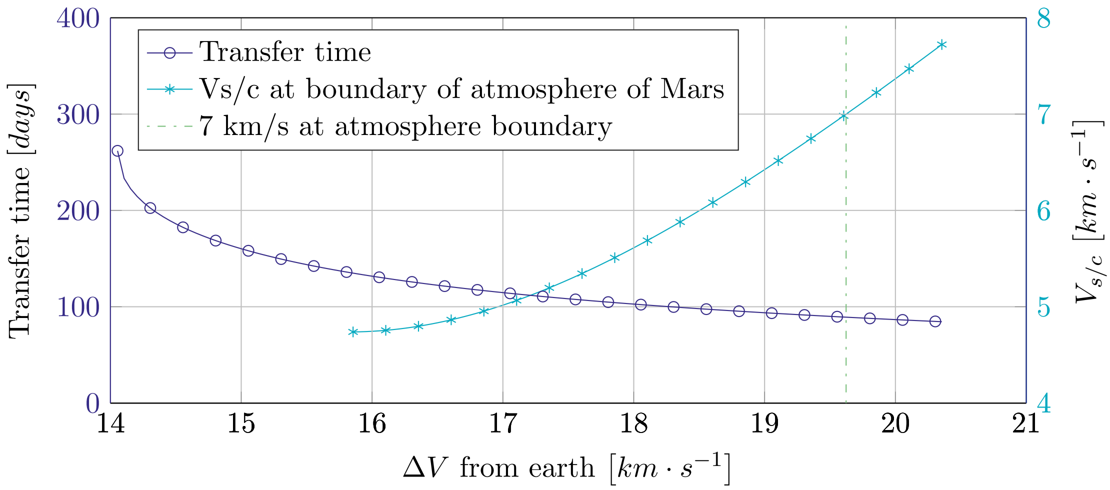

Figure 2.1: Interplanetary transfer time (left) and entry velocity (right) versus ΔV

The most efficient transfer with respect to the ΔV-budget consists of a Hohmann transfer orbit. This would take approximately 262 days. This time is the longest of all orbits to Mars with a direct transfer. One of the mission requirements is the entry velocity of $7\,[km \cdot s^{-1}]$. This velocity is fully determined by the ΔV budget and thereby corresponds to the transfer time. In Figure 2.1 this relation is visualised. As can be seen to arrive with the required velocity a ΔV of $19.62\,[km \cdot s^{-1}]$ is required, which corresponds to a transfer time of 89.3 days. The corresponding orbit is shown in Figure 2.2.

2.1.3 Aerocapture and entry

The third phase of the mission is the arrival at Mars and the deceleration to a velocity of $M = 5\,[-]$ at $15\,[km]$ height above the surface of Mars with an accuracy of $500\,[m]$ in each direction. This deceleration is split into an initial aerocapture, a parking orbit and a final entry. The combined sum of these components should not take longer than 10 Earth days. In this phase of the mission the CIA is used to decelerate the capsule and protect

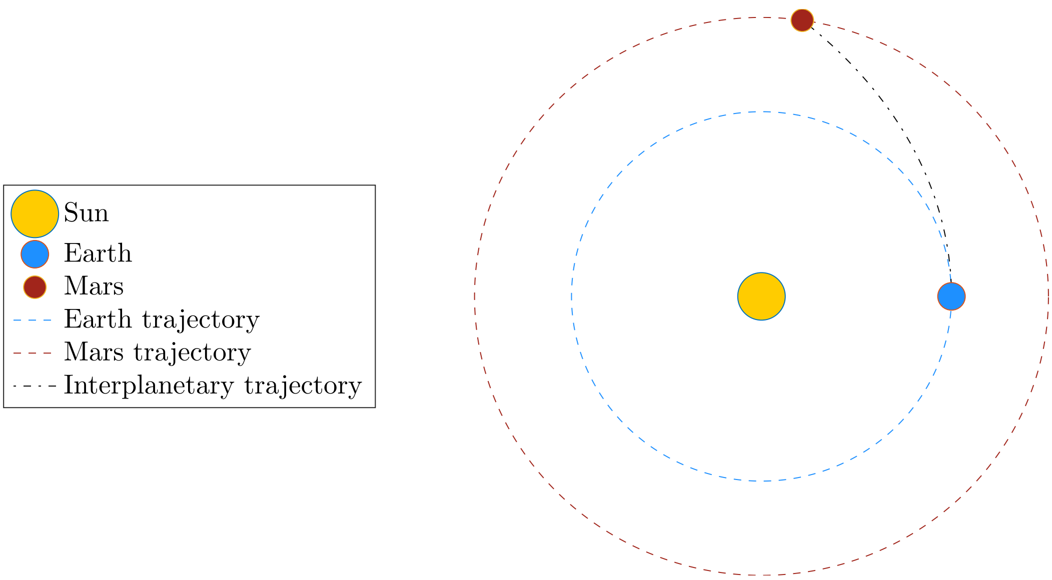

Figure 2.2: Visualisation of the interplanetary transfer orbit. Planets not to scale

it against the thermal loads imposed by the deceleration. In addition, taxation of human crew members requires loads not to exceed $3g_e$.

Upon arrival at Mars the first thing that happens, just before the spacecraft enters the atmosphere, is the deployment and inflation of the CIA.

The entry vehicle then enters the atmosphere for the first time. This first pass through the atmosphere is called aerocapture. The entry vehicle will fly through the atmosphere following a pre-determined path using active bank control. A real-time controller will manage the active control systems to account for unexpected differences in atmospheric properties. The goal of this controller is to keep the kinetic energy lost during the aerocapture equal to what is pre-calculated. This loss of kinetic energy determines the characteristics of the trajectory which the spacecraft will follow once it leaves the atmosphere.

After the aerocapture the spacecraft goes into an elliptic Kepler orbit. When the spacecraft is headed to the apocentre of the orbit it changes attitude so that the thrusters point in the along-path direction to give the spacecraft a velocity change. While in the apocentre the spacecraft produces a ΔV to raise the pericentre altitude of the Mars-centred orbit to a parking orbit at $200\,[km]$ height.

From this parking orbit the atmospheric conditions can be observed and a plan can be made for the entry into the atmosphere in order to get to the intended landing location. The observations made of the atmosphere will help determine a suitable moment to do the final entry and will give information that can be used to predict the final entry trajectory more accurately. For example, in case of a dust storm, characteristic of Mars, Entry, Descent & Landing (EDL) can be delayed until it has passed.

Once the decision has been made to conduct the final entry the spacecraft is given a second boost to decelerate it just enough to get the entry vehicle into the desired trajectory. Here, just as during the first pass through the atmosphere, the spacecraft is controlled using active bank control managed by a real-time controller.

2.1.4 Terminal descent

Terminal descent of the spacecraft commences at $15\,[km]$ altitude and is concluded by landing on the surface of Mars. The velocity is to be brought back to zero at an altitude of zero, from an initial velocity of Mach 5 at $15\,[km]$ altitude. For the terminal descent, several design options are available to decrease the velocity.

The start of this mission phase is given by the end of the aerocapture segment, of which the requirements dictate a Mach number of 5 at an altitude of $15\,[km]$, see Section 2.4. This means the aerodynamic flow regime changes from hypersonic to supersonic, and finally to subsonic during the terminal descent. The speed of sound in the lowest fifteen kilometres of the Martian atmosphere is approximately $220\,[m \cdot s^{-1}]$, which means the velocity of the spacecraft is $1100\,[m \cdot s^{-1}]$ at the beginning of terminal descent. The flight path angle follows from aerocapture and entry as approximately $20\,[deg]$.

Terminal descent can be split up in two parts: the supersonic & subsonic flight segment and final touchdown. For both parts, different design options are available.

The first option for the flight is to use retro-propulsion for every part of the descent. The fuel mass would be 23.3% of the total spacecraft mass if no aerodynamic effects are taken into account. However, the CIA has a large frontal area which produces a significant amount of drag. Also, in numerical simulations and wind tunnel tests the interaction between retro-propulsion and the CIA were found to result in a mass fraction that is approximately half as big as would be expected when considering the thrust and drag forces to act independently of each other [10]. Since a blunt body is unstable at transonic and supersonic speeds, a small drogue parachute is needed to stabilise the spacecraft. Scaling a mass estimate for an inflatable aeroshell from NASA, this stabilisation drogue parachute is approximately $20\,[kg]$.

The fuel mass is estimated assuming a constant deceleration of $3g_e$. This condition in combination with the initial conditions of the terminal descent leads to a specified flight path angle (equal to $38\,[deg]$) and velocity at each height. Using this velocity the drag was calculated assuming the same drag coefficient throughout the whole supersonic regime. This analysis is known to be incorrect to a certain degree, but since this is a preliminary analysis this is taken for granted. The drag at every height leads to a deceleration lower than $3g_e$, and thrust is delivered at a level such that this deceleration is achieved, incorporating the gravitational force.

The resultant drag, thrust and total required force are shown in Figure 2.3. This requires the rocket engines to be sized such that a total thrust of $312\,[kN]$ can be achieved. To this end 3 RL-10A-4 rocket engines are placed at the front of the centre body. The combined mass of these rockets is $504\,[kg]$. The thruster fuel flow is calculated using the specific impulse of the engine, equal to $451\,[s]$, and integrated over time to find the total fuel mass, estimated to be $680\,[kg]$ [8, p.538]. Propellant tank mass is estimated to be $45\,[kg]$ using Equation 16, assuming a density of $1\,[kg \cdot dm^{-3}]$ for the fuel [8, p.543].

The other option is to use a large parachute to decelerate. Since a parachute's performance decreases quadratically with lower velocities, the final landing still requires thrusters to bring the velocity down to an acceptable value for landing [11]. The difference in fuel mass was estimated by using a parachute with a diameter of $30\,[m]$ and a drag coefficient of 0.3, deployed at the moment in time where the added drag of the parachute would make the total acceleration $3g_e$. For these conventional figures, the fuel mass loss was

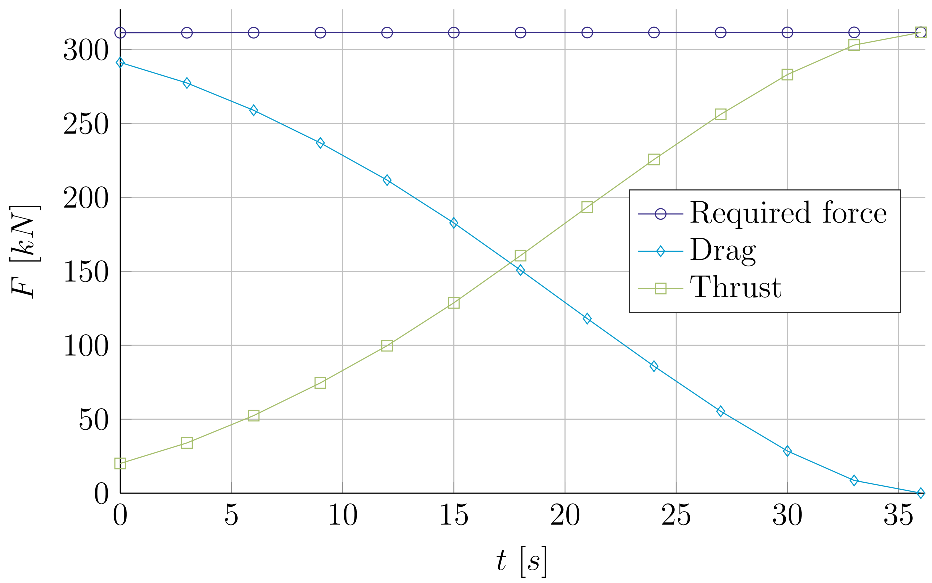

Figure 2.3: Thrust, drag and required force for $3g_e$ deceleration starting from $15\,[km]$ altitude at $M = 5\,[-]$

approximately $200\,[kg]$, while the added mass of a parachute is approximately $280\,[kg]$ per an empiric relation [12]. The absence of mass reduction for adding a parachute, added to the fact that the atmospheric density on Mars offers unacceptable parachute deployment [10], leads to the conclusion that a parachute is not beneficial for the final descent.

Final touchdown can happen by carefully manoeuvring the spacecraft with thrusters to land on legs. These were estimated to have a mass of $200\,[kg]$, as estimated using a structural sizing for a smaller spacecraft to be landing on Mars.[1] The other option is to land using airbags, as was performed by for example the Mars Pathfinder. However, this induces high peak accelerations during the landing and introduces uncertainties in landing location since the airbag bounces before coming to a halt.

2.1.5 Return

The return from Mars will require several systems to already be in place by the time the crew arrives. A Mars Ascent Vehicle (MAV) is required to lift the crew back into an orbit around Mars. An Earth Return Vehicle (ERV) is required to take the crew back from Mars to Earth. To reduce the risk of stranding the crew on Mars without any option to return to Earth, these vehicles should be in place before the crew commences the aerocapture.

The MAV and ERV will need to be part of the cargo sent to Mars ahead of the manned mission. The amount of thrust and propellant required to lift off from the Martian surface makes it infeasible to combine the ascent and descent phases of the mission. The MAV therefore needs to be prepositioned on the surface of Mars, along with the habitat and supplies required for the stay on Mars. The ERV requires a sizeable habitation module for the return to Earth. Due to the mass associated with this size, it should be placed

[1]URL: `http://www.nasa.gov/pdf/458812main_FTD_AerocaptureEntryDescentAndLanding.pdf`. Accessed: 18-06-2015

in orbit around Mars while waiting for the return trip rather than launched from the Martian surface as part of the MAV [13].

2.2 Ground segment

It is important that the ground segment is taken into consideration at this stage to assess mission feasibility and to provide an early impression of the required ground facilities. The ground segment is an essential mission feature to facilitate communication flow between Earth and spacecraft and thereby to monitor mission progress and crew member status as well as take corrective actions if needed and circumstances allow.

To this end the ground segment consists of a missions operations centre and a communications network. This set-up is similar to European Space Agency (ESA) ground operations for deep space missions Rosetta and Venus Express[2] [14]. An alternative would be a decentralised structure, in which control centres are not included in the missions operations centre but linked separately to it.

Operations centre The operations centre is manned continually with the purpose of monitoring and controlling mission progress [14]. It is the ground system element that is in direct contact with the spacecraft via the link established through the ground stations for uplink and downlink [8, p.879]. Downlink data is analysed and formatted, partially sent through to the end-receivers of scientific information and partially used for mission health monitoring and control. The nature of these end-receivers of scientific information depends on the payload activities conducted in-flight and on Mars.

Examples of such an operations centre are the California Institute of Technology's Jet Propulsion Laboratory, responsible for NASA's Deep Space Network (DSN), or the European Space Operations Centre (ESOC), responsible for ESA deep space missions. The former has been used for one for the manned Apollo missions to the moon, the latter for Rosetta and Apollo missions [8, p.883][14]. Both of these operations centres would be suitable for the mission at hand, mainly due to their successful operation in past deep space and manned missions.

Communications network Key feature of the communications network ability for communication between Mars and Earth, over which free space losses are highly significant [8]. While manned missions to Mars have not been flown, a good reference point is a previous unmanned Mars mission, such as the Mars Rover, as both face similar communication requirements. The Mars Rover was reliant on the DSN[3] for its communications on X-band.

The DSN uses three complexes separated by 120 degrees of longitude to provide continual coverage with a rotating Earth. Sensitive 70 $[m]$ diameter antennas are used for maximum sensitivity and complemented by a number of 34 $[m]$ diameter antennas [8]. These antennas would be suitable for the mission at hand by their intended and proven purpose of providing communication in deep space and to and from Mars. While the technology is

[2] URL: `http://www.esa.int/esapub/bulletin/bulletin124/bul124e_warhout.pdf`. Accessed: 10-06-2015

[3] URL: `http://mars.nasa.gov/mer/mission/communications.html`. Accessed: 10-06-2015

thereby sufficient, continuous maintenance of and improvements to the DSN will ensure proper functioning and network availability over the next decades. An alternative would be ESA's ESTRACK, consisting of 10 ESA-operated ground stations for communication support. However, these do not allow for Ka-band transmission [8, p.631].

Bandwidths are required to allow for sufficient signal strength upon reception and additionally follow from the required bit rate. The current standards for deep space missions are S-band, in a frequency range of 2.0-2.3 $[GHz]$, and X-band, in a frequency range of 8.45-8.50 $[GHz]$ [8].

An advancing trend is the use of Ka-band for deep space communication downlink, in a frequency range of 25.5-32.3 $[GHz]$. Ka-band is able to provide more data volume in less DSN tracking time, while continuing automation for DSN ground systems will further increase antenna availability through a reduction of required calibration time [15].

Following requirements on NASA's DSN S-band will be available for both up- and downlink, while Ka-band will be available for high-data-rate science returns [16]. The crew module itself will not necessitate Ka-band for the purpose of science returns, but transmission of detailed system state measured by sensors for the purpose of monitoring will benefit from the use of a Ka-band for downlink by a high required data rate. For the purpose of uplink, limited data flow is present and S-band suffices.

As such, Ka-band is used for downlink telecommunication for its high data link capability, while S-band is used for uplink. Both are supported by the DSN.

Due to the long transfer time between the spacecraft and Earth, it is key that the delay in communication is taken into account and the spacecraft is self-reliant rather than dependent on ground instructions. As such, the on-board computer is autonomous with a manual override for crew members.

2.3 Mission scope

Whereas Section 2.1 covers the entire mission from launch to return on Earth the focus of this report lies with the aerocapture into a parking orbit around Mars, together with the subsequent aerobraking. To achieve this a CIA has been designed, based on the requirements covered in Section 2.4. Even though the mission of the CIA is concerned with the entry procedure described in Section 2.1.3 the other mission elements also carry an effect on its design. From the launch mentioned in Section 2.1.1 follows that the CIA must be able to withstand the launch loads and vibrations.

Following launch, Earth orbit and subsequent acceleration into a heliocentric orbit the interplanetary flight phase of the mission takes place, as described in Section 2.1.2. From this mission phase comes the requirement for the deceleration capability of the CIA, a shorter interplanetary transfer time results in a higher velocity with respect to Mars. This is further covered in Section 2.4.

When the capsule carrying the crew arrives at Mars with its accompanying modules and systems required for interplanetary transfer the actual mission of the CIA takes place. It is this mission segment that forms the scope of this report and is where the CIA performs its function. The aerocapture, parking orbit and subsequent entry and terminal descent procedure can take up to ten days altogether. After the terminal descent & entry procedure has been initiated the CIA will be retained to aid in the final descent and deceleration until touchdown.

As such, the considerations in this chapter on the entire mission and the crew capsule design in Chapter 5 are conceptual suggestions for further design efforts. To this end, their main purpose is to investigate the compatibility of the CIA, crew module and mission. Other design options for the crew module remain possible.

2.4 Mission requirements

In this section the mission requirements for the aerocapture and entry phase as described in Section 2.3 are outlined and their origin is explained. A full list of requirements as defined top level can be found in Table 2.1 and 2.2.

The aerocapture and final EDL starts at the boundary of the atmosphere of Mars. Here the velocity of the entry vehicle is $7\,[km \cdot s^{-1}]$. This requirement is imposed by the transfer trajectory that is taken from Earth to Mars. This trajectory should take as short as possible in order to both shorten the entire mission duration and decrease the physical taxation on the crew. The interplanetary transfer time corresponding to an entry velocity of $7\,[km \cdot s^{-1}]$ is 89 days.

The mission ends at a speed of $M = 5\,[-]$ at $15\,[km]$ altitude. At this point a terminal descent system takes over. The predetermined point at which the mission ends shall be reached with a precision of $500\,[m]$. This requirement is imposed by the distance the final landing position can be from the provision. When the landing position lies too far from the provision a lot of time will be lost relocating the crew or crew members might not even be able to reach the provision.

While decelerating in the atmosphere the maximum deceleration shall not exceed $3g_e$. This requirement is imposed because of the limited capability of the crew to carry high deceleration loads.

The entry vehicle shall attain its final velocity within ten Earth days. This requirement is, just like the interplanetary transfer time, imposed both to shorten the aerocapture and entry phase duration and decrease the physical taxation on the crew. An additional reason for this time constraint is to limit the cost for and strain on the ground control crews that will be active continuously during the aerocapture and entry phase.

Table 2.1: Overview of mission requirements for the aerocapture and EDL

ID	**Description**
CIA-M01	The entry vehicle shall decelerate from a velocity of $7\,[km \cdot s^{-1}]$ at $400\,[km]$
CIA-M02	The entry vehicle shall not exert an acceleration greater than $29.4\,[m \cdot s^{-2}]$ on any crew member for the duration of the mission
CIA-M03	The entry vehicle shall attain Mach $5\,[-]$ at an altitude of $15\,000\,[m]$ Mars Orbiter Laser Altimeter (MOLA)
CIA-M04	The entry vehicle shall reach its final position with a precision of $500\,[m]$
CIA-M05	The entry vehicle shall attain its final velocity within 10 days after entering the Martian atmosphere

Table 2.2: Overview of entry vehicle requirements

ID	Description
CIA-R01	The entry vehicle shall have an undeployed diameter smaller than 5 $[m]$
CIA-R02	The entry vehicle shall have a deployed diameter smaller than 12 $[m]$
CIA-R03	The entry vehicle shall have a mass of 10 000 $[kg]$ at the start of the entry
CIA-R04	The hypersonic decelerator shall have a mass fraction of no greater than 10% of the vehicle mass
CIA-R05	The entry vehicle shall adhere to the Committee on Space Research (COSPAR) regulations
CIA-R06	The entry vehicle shall have control system reliability of at least 0.9995

2.5 Market analysis

Three dimensions are used to define the market for the product: function, technology and customer. The purpose of the market analysis is a minimisation of risk of selecting incompatible function and technology for a selected set of customers. A Strengths, Weaknesses, Opportunities and Threats (SWOT) analysis gives an overview of product characteristics.

2.5.1 Customer base

Prospective customers are scientific or governmental agencies on one hand and private ventures on the other hand. Leading player in the former is NASA, by order of the United States (US) government. The US are in pursuit of human exploration of Mars in the 2030s[4], formulated in the National Space Policy issued in 2010[5]. On the basis thereof, it has been formulated as a goal in the NASA Authorization Act of 2014[6].

The US government is a key player due to the significant budget allocated to planetary science and Mars exploration. Forecasts dating from the Fiscal Year 2013 budget estimates [17] are taken up in Table 2.3. The second row reflects the US government's dedication to extraterrestrial exploration. The third row shows increasing budgets allocated to Mars exploration, reflecting the continuing interest and dedication to Mars exploration.

Table 2.3: NASA budget forecasts

Fiscal year	2015	2016	2017
Planetary science [mln $]	1 102.0	1 119.4	1 198.8
Mars exploration [mln $]	188.7	266.9	503.1

The interest expressed by the US in human exploration of Mars is shared by a number of private ventures, most notably Mars One, the Inspiration Mars Foundation and SpaceX. The former two are non-profit organisations, while SpaceX is a commercial venture. Mars

[4]URL: `https://www.nasa.gov/content/nasas-journey-to-mars`. Accessed 28 April 2015

[5]URL: `https://www.whitehouse.gov/sites/default/files/national_space_policy_6-28-10.pdf`. Accessed 28 April 2015

[6]URL: `http://science.house.gov/sites/republicans.science.house.gov/files/documents/HR%204412.pdf`. Accessed 28 April 2015

One has expressed its goal as the permanent human settlement on Mars with planned departure of the first non-human payload in 2020 and the first human payload in 2026[7]. The Inspiration Mars Foundation, in cooperation with NASA, seeks to transport two humans, a male and female, to Mars for planned launch in 2021[8]. SpaceX is a privately funded venture currently working in close cooperation with NASA to provide launchers for manned missions to Mars[9].

These planned missions illustrate the commercial interest in human spaceflight to Mars. Commercial interest in CIA's is directly coupled to this by the fact that these provide a cost-effective means of entry and re-entry. Along with this commercial interest, ongoing investigations by NASA provide an indication of scientific interest in this field of study. In the end, all interest is fuelled by human curiosity and the desire to explore and habitate extraterrestrial environments. These environments are expected to expand beyond Mars and therefore interest in (re-)entry vehicles is expected to remain.

2.5.2 Function

Primary prospects for the use of a CIA are the following:

- Perform entry for manned spaceflight on Mars;
- Serve as a basis for design extrapolation to perform manned (re-)entry at other sites, for example Earth;
- Serve as a basis for design extrapolation to perform (re-)entry of unmanned spaceflight;
- Further the technology development and application of inflatable technologies in spaceflight.

A direct function or use is the first item: the CIA provides aerodynamic deceleration for (safe) transportation of human payload in a cost-effective manner. While the CIA is designed for entry on Mars, the design can be extrapolated to perform entry or re-entry on a number of sites, for one Earth.

2.5.3 Technology

The CIA will demonstrate predominantly the following technologies:

- An asymmetric stacked toroid structure
- A large-scale inflatable and inflation system
- Bank control for Mars targeted aerocapture and landing
- A multi-layer flexible and foldable thermo-structural design using state-of-the-art PBO Zylon® fibres and Nicalon™

These technologies are firstly of key importance for commercial interest. An inflatable structure in itself has significant advantages over conventional rigid solutions, but in particular the asymmetric shape and the use of state-of-the-art materials provide means by which to increase the cost-effectiveness of (re-)entry solutions. Secondly, the demonstration of these technologies will further their stage of development and gain additional knowledge in the use of CIA technology for (re-)entry.

[7]URL: `http://www.mars-one.com/`. Accessed 28 April 2015

[8]URL: `http://spacenews.com/39714inspiration-mars-sets-sights-on-venusmars-flyby-in-2021/`. Accessed 28 April 2015

[9]URL: `http://www.spacex.com/falcon9`. Accessed 28 April 2015

Table 2.4: Design high-level SWOT analysis

Strengths	Weaknesses
+ <10% decelerator mass fraction + Compact solution	- Development risk - Deployment risk
Opportunities	**Threats**
+ Growing demand + Breakthrough technology	- Catastrophic failure manned mission - Competing concepts

2.5.4 SWOT analysis

Identification of the primary characteristics, in terms of a SWOT analysis[10], of the proposed CIA yields Table 2.4.

Strengths and weaknesses are internal to the design, while opportunities and threats are external factors. The cost at which the significant mass decrease and packaging efficiency increase (with respect to conventional rigid solutions) comes is reflected by an increased development risk and deployment risk. The former is the result of the novelty of inflatable decelerators; the latter inherent to the use of an inflation and deployment system. While the design retains a development risk, being a relatively new concept, this weakness can be mitigated by proper verification activities. Such activities do, however, incur additional time and costs to the design process. As such, risk remains inherent to the design.

2.6 Sustainable development strategy

Increasing awareness with respect to sustainable development makes sustainability an important consideration within the design of the CIA. Masud et al. define development as being sustainable "by ensuring the needs of the present demands without compromising any power or ability of future generations to meet their own needs" [18, p.85].

Within the scope of the mission sustainability is considered where possible. It must however be considered that the production series length is small and less emphasis is given to sustainable development when compared to (for example) a commercial passenger jet. As such the overall environmental impact of the CIA is negligible and the sustainability of the concepts discussed in this report is not taken into account as a strong design driver. Nevertheless important consideration with regards to sustainability may be taken.

Decelerator structural mass reductions directly allow for increases in useful payload or, allow for the use of smaller launchers for the same mission. By doing so the environmental footprint of each launch may be reduced with respect to comparable missions. A conventional rigid solution was investigated in the concept selection phase [19]. Preliminary mass estimates were over a factor three larger than the design presented within this final report. Choosing such a conventional concept would not only violate the mission requirements but would also incur additional emissions during the initial launch.

Sustainability is also taken into account outside of the Earth's atmosphere. Special care will be given to prevent accidental contamination of other orbital bodies with organic lifeforms and other contaminants. For this purpose no parts of the decelerator structure

[10]URL: `http://www.usfca.edu/fac_staff/weihrichh/docs/tows.pdf`. Accessed: 19-06-2015

are separated during the descent towards the surface of Mars. This is in line with article IX of the Outer Space Treaty of 1967 [20], enforced by the COSPAR. Moreover the materials used in the design are considered where possible. One such example is the use of nitrogen as the inflation gas as further detailed in Section 7.3.3. Less sustainable inflation gasses could be considered, such as for example hydrazine, which could achieve marginal mass reductions. From a sustainability point of view such an option was not preferred.

Looking at the full impact of an interplanetary mission of such a scale, environmental impact can never be prevented. However, in line with aforementioned definition of sustainability, the design presented in this report will be able to deliver for present demands while simultaneously working towards a design with less impact on the design than current technologies.

2.7 Cost breakdown structure

Cost can be split up into two sections: Development cost and production cost. Whereas the development-related costs consist of non-recurring expenses, the production cost is dependent on the number of missions to be carried out. The analysis by Wertz et al. [8] will be used to determine the costs associated with these components. Since these are determined in constant 2010 US dollars a factor accounting for inflation is used. This factor was found by looking at the consumer price index ratio between April of 2010 and 2015. From Reference [21] this factor was found to be 1.075, corresponding to an inflation over five years of 7.5%.
For the development and production cost a CIA propellant mass of 153 $[kg]$ was used, conform to the final design presented in Chapter 7. A total CIA mass (including propellant) of 1000 $[kg]$ was assumed, in order to take into account the maximum allowable CIA mass growth. For the crew capsule a total mass of 9000 $[kg]$ was assumed from which 700 $[kg]$ of propellant mass was subtracted. The origin of this propellant mass will be covered in further detail in Chapter 5. In addition to the propellant mass the crew mass was also subtracted in order to arrive at the spacecraft dry mass.
Next to the CIA and accompanying crew module a MAV and an ERV are also needed to complete the mission. These vehicles fall outside of the scope of this report, but in order to estimate their impact on mission cost they will be taken into account in this section. A dry mass of 5000 and 10 000 $[kg]$ was assumed for these vehicles respectively.

2.7.1 Development costs

In contrast to the total mission the development costs consist of those incurred by CIA and capsule development. Atgar [8, p.296] presents the development cost per kilogram of dry mass for various vehicles. These values, together with the total development cost are shown in Table 2.5.

2.7.2 Production costs

The production costs were determined in similar fashion to the development costs presented in the previous section. Table 2.6 shows the corresponding productions costs per kilogram of dry spacecraft mass and for the complete respective component.

Table 2.5: Development costs in 2015 US dollars

Cost component	Development cost per kg dry mass [2015 US$]	Total development cost [2015 million US$]
CIA	2 569 000	2 176
Crew module	1 255 000	10 216
Mars Ascent Vehicle	2 569 000	12 845
Earth Return Vehicle	1 255 000	12 550
Total	-	37 786 854

Table 2.6: Production costs in 2015 US dollars

Cost component	Production cost per kg dry mass [2015 US$]	Total production cost [2015 million US$]
CIA	341 000	289
Crew module	173 000	1 408
Mars Ascent Vehicle	341 000	1 705
Earth Return Vehicle	173 000	1 730
Total	-	5 132

2.7.3 Mission costs

In addition to the costs incurred by the spacecraft themselves the overall mission architecture requires the use of additional resources such as launch vehicles. Assuming that two SLS' are needed to position all required vehicles mentioned in Section 2.1 around Mars (including the mission carrying the CIA and associated crew module) the mission item cost can be determined by summing these launch costs with the aforementioned production costs. For the launch of the SLS no official cost figure exists, though NASA officials have been quoted as mentioning a goal of 500 million US dollars per launch[11]. As such the total launch cost for two launches per mission adds up to 1 billion US dollars.

Table 2.7: Overview of total costs for one mission

Cost component	Cost [2015 million US$]
Vehicle development	37 787
Vehicle production	5 132
Launch	1 000
Total	43 919

By combining the cost figures presented here the results presented in Table 2.7 were obtained. If more than one mission using these spacecraft is to be conducted the average cost per mission will be considerably lower than the total cost presented in Table 2.7 since the development costs are non-recurring expenses. This would also increase the cost-effectiveness of manned spaceflight to Mars.

[11]URL: `http://www.nbcnews.com/id/49019843/ns/technology_and_science-space` Accessed: 18-06-2015

3 Concept selection

This chapter describes the steps leading up to the selection of the stacked toroid concept. This concept has been found to yield the most favourable combination of characteristics and was therefore selected for further analysis. Concepts have been generated in a structured way using a design option tree, as described in Section 3.1. Subsequently, concepts were evaluated for four trade-off criteria, defined in Section 3.2. This yields an overview of relative concept performance, summarised in Section 3.3.

A more detailed overview of the trade-off process is given in the Mid-Term Report [19].

3.1 Concept generation

Concepts were generated on the basis of decelerator configuration, the leading design parameter to distinguish concepts. On the basis of the shape design option tree given in Figure 3.1, five blunt bodies were selected for the trade-off process. Four inflatable concepts were selected alongside one rigid concept to fully appreciate the advantages inflatable concepts offer.

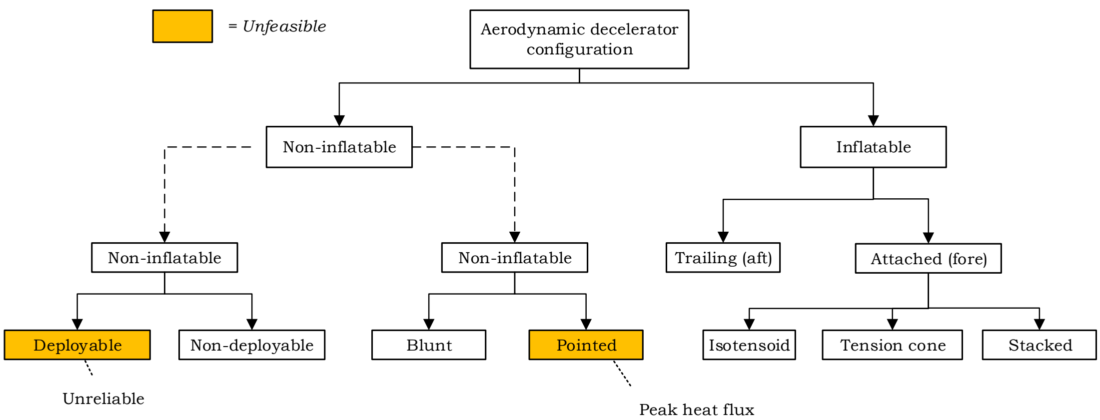

Figure 3.1: design option tree for entry vehicle configuration

Non-inflatable deployable concepts offer a lower reliability than and no particular advantages to inflatable concepts and were therefore discarded. Pointed shapes were found infeasible by the peak heat flux generated. Lastly, combined inflatables were discarded since these add system complexity and mass while offering no additional advantages.

Artist impressions of the resulting five concepts are given in Figure 3.2. The concepts are:

(a) A rigid concept, which is the conventional solution for entry vehicles. Its absence of deployment and its thereby limited diameter necessitates the use of a backshell to prevent the side of the payload capsule from excessive heating [22].

(b) An isotensoid, a flexible bladder encapsulating the crew module that is inflated by ram-air through inlets mounted on it.

(c) A stacked toroid concept, in which multiple flexible rings are stacked on top of each other and inflated by an internal inflation system.

(d) A tension cone concept, which features one internally inflated torus and a flexible membrane that is spanned between the torus and the rigid centre body.

(e) A trailing ballute concept, which is the sole concept with a trailing inflatable. The inflated torus is connected to the payload capsule by multiple cables.

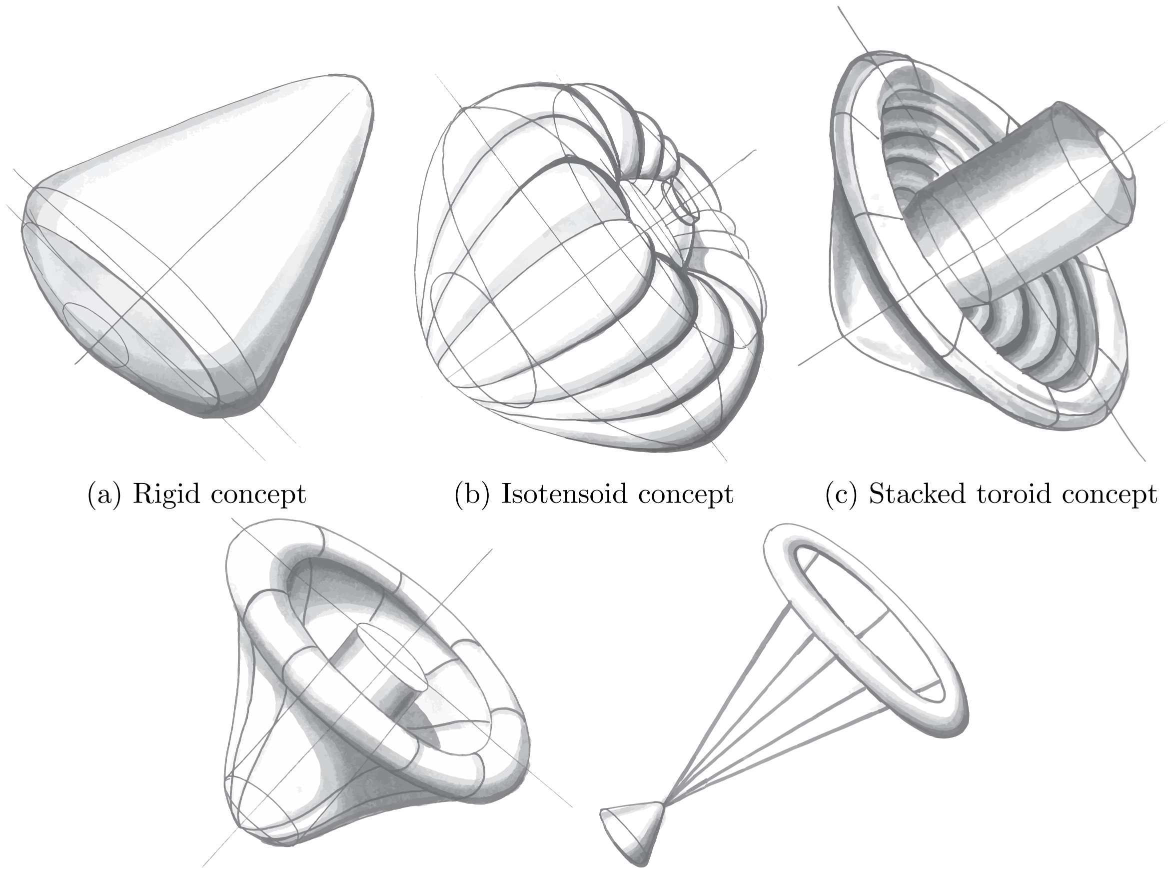

(a) Rigid concept (b) Isotensoid concept (c) Stacked toroid concept

(d) Tension cone concept (e) Trailing ballute concept

Figure 3.2: Overview of design concepts (Courtesy of Irene Heemskerk)

3.2 Concept trade-off criteria

Concepts have been evaluated on the basis of the following four criteria: decelerator mass, deceleration time, stability and development risk. These are discussed hereafter.

3.2.1 Decelerator mass

To take full advantage of launcher capability, the total vehicle mass is kept at its maximum. An increase in decelerator mass then leads to a decrease in payload mass, so it is essential that decelerator mass is kept to a minimum. To this end, the three primary components making up decelerator mass were evaluated for each concept: TPS mass, structural mass and control system mass. Their weighted average was computed to yield a total mass, taking into account their respective significance. The weight factors were determined from a comparable inflatable entry vehicle, namely Inflatable Re-entry Vehicle Experiment (IRVE) [22].

The relative structural mass was determined using the structural mass estimation tool described in Section 6.1.5 and in more detail in the Mid-Term Report [19, p.47-66]. Relative TPS mass is reflected by the estimated peak heat flux, a first-order estimation of the thermal energy to be dissipated and a key design driver for the TPS. Relative control system mass is reflected by the control moment required to be effected by the control system, in the form of the moment coefficient following from the aerodynamic analysis using modified Newtonian flow theory, as described in Section 6.1.2. This was characterised by the lift-to-drag ratio, to account for the difference in lifting capability between concepts. Lower peak heat flux and low moment coefficients are favourable in terms of mass.

3.2.2 Deceleration time

Minimising deceleration time is favourable for minimising ground operations expenses, since ground control is required to be fully active at the time of entry, which is the most critical mission phase. Furthermore, taxation of crew members is then alleviated. The time spent in the atmosphere is reflected by vehicle lift-to-drag ratio. For a given $C_D A$, the maximum deceleration can be chosen by varying the lowest part of the trajectory: the density in lower parts of the atmosphere is higher, which then compensates for a low drag coefficient to produce the same force as a spacecraft with a high drag coefficient at a higher altitude with lower density. Because of the large variation of density in the atmosphere, it is possible to find a trajectory for any $C_D A$. Thus, the drag coefficient itself is not a key driver for the design. However, the spacecraft can influence its deceleration time in the atmosphere by producing lift: if the spacecraft were to fly out of the atmosphere, a downward pointing lift would divert its trajectory more through the atmosphere. The ability of the spacecraft to influence this trajectory through the atmosphere is characterised by the amount of lift that can be produced, with respect to the amount of drag produced at the same α. The dependence on drag is due to the fact that two spacecraft with the same lift-to-drag ratio but a different $C_D A$, will just have the lowest part of the trajectory at a different altitude, where the total lift and drag force will be the same for both spacecraft. Therefore, the deceleration time is characterised by the lift-to-drag ratio.

Lift and drag coefficients follow from the aerodynamic analysis tool, described in detail in the Mid-Term Report [19, p.34-46].

3.2.3 Stability

Vehicle stability is preferable, since a stable vehicle will react to disturbances with a restoring moment to revert to its original equilibrium condition without requiring control system activity. Not only does this reduce required control system activity, thereby limiting the system mass, but in addition the vehicle is more robust and less susceptible to perturbations. Stability is reflected by the static stability coefficient of concepts, following from aerodynamic analysis.

3.2.4 Development risk

It is key that concepts are evaluated for their development risk, an indication of schedule and cost risk. A concept with a high development risk will require extensive investigation to fully explore its capabilities and mitigate risks by technical uncertainty associated with such an underdeveloped concept. These investigation efforts incur additional cost and schedule risk. Development risk of concepts is evaluated by their TRL, denoting the current state of testing and application.

3.3 Concept performance

In terms of decelerator mass, the isotensoid was estimated to be the lightest concept, followed by the stacked toroid, illustrated in Table 3.1. The tension cone and trailing ballute were notably heavier, primarily due to a higher structural mass. From this mass analysis, mass benefits of inflatable versus rigid concepts were clearly identifiable. On the basis of reference missions and scaling of estimated mechanical and thermal loading, decelerator thermo-structural mass was estimated at nearly 3000 $[kg]$. Key contributor was the backshell weighing well over 1400 $[kg]$. Such a backshell is not needed for the inflatable concepts. This mass was far in excess of the 1000 $[kg]$ limit imposed on maximum decelerator mass.

Table 3.1: Concept mass comparison (expressed as percentage of stacked toroid mass)

	Structural mass (20%)	**Thermal mass (50%)**	**Control system mass (15%)**	**Total mass**
Stacked toroid	100	100	100	100
Tension cone	168	100	100	116
Trailing ballute	221	84	67	113
Isotensoid	110	76	96	88
Rigid	Estimated 3000 $[kg]$: Far in excess of 1000 $[kg]$ limit			

In terms of deceleration time, lift-to-drag ratio, performance of the rigid concept was best, that of the isotensoid notably worst and those of the other three inflatable concepts in between and comparable. In terms of concept static stability, the isotensoid again performed notably worst, being unstable. The rigid concept proved neutrally stable and the other three inflatables are stable. These results are illustrated by Tables 3.2 and 3.3.

Table 3.2: Review of concept deceleration time

	Stacked toroid	**Tension cone**	**Trailing ballute**	**Isotensoid**	**Rigid**
Lift-to-drag ratio	-0.176	-0.176	-0.210	-0.072	-0.311
Deceleration performance	Adequate	Adequate	Adequate	Poor	Excellent

Technology readiness, reflected by the TRLs in Table 3.4, is highest for the conventionally tested and flown rigid concept. The stacked toroid concept was flown in multiple NASA (IRVE) missions and prototypes thereof have thus been tested in a relevant environment. The other three inflatables have received notably less attention, having solely

Table 3.3: Review of concept stability

	Stacked toroid	**Tension cone**	**Trailing ballute**	**Isotensoid**	**Rigid**
Static stability	Stable	Stable	Stable	Unstable	Neutrally stable

undergone wind tunnel and laboratory testing. In addition, the difficulty of controlling a trailing ballute using conventional methods necessitates the use of morphing. As morphing is a relatively underdeveloped concept and has only been formulated in theory for trailing ballute configurations, the TRL of the trailing ballute reflects this by being the lowest.

Table 3.4: Review of concept development risk

Concept	**Stacked toroid**	**Tension cone**	**Trailing ballute**	**Isotensoid**	**Rigid**
TRL	7	4	2	4	9

3.4 Conclusion

From the trade-off criteria performance of the different concepts discussed above, the stacked toroid configuration was chosen. The rigid concept is clearly infeasible due to its estimated mass that is far beyond the mass requirement. The isotensoid performs worst of the remaining 4 concepts, offering a statically unstable spacecraft in combination with poor performance in the lift-to-drag ratio and deceleration performance. The trailing ballute does not perform better than the tension cone and rigid, while still being more complex and a very high development risk. Between the tension cone and stacked toroid, the choice was made to investigate the stacked toroid further, due to its higher TRL and higher fidelity in determining the aerodynamic shape.

4 System definition

This chapter discusses the system definition. First off the functions of the system are discussed in Section 4.1. The system is further broken down in subsystems in Section 4.2. Finally the technical risks of the system are discussed in Section 4.3.

4.1 Functional definition

The entry vehicle is required to perform the functions listed in the functional breakdown structure of Figure 4.1, which categorises the main vehicle functions. These functions can subsequently be attributed to the subsystems partaking in the mission.

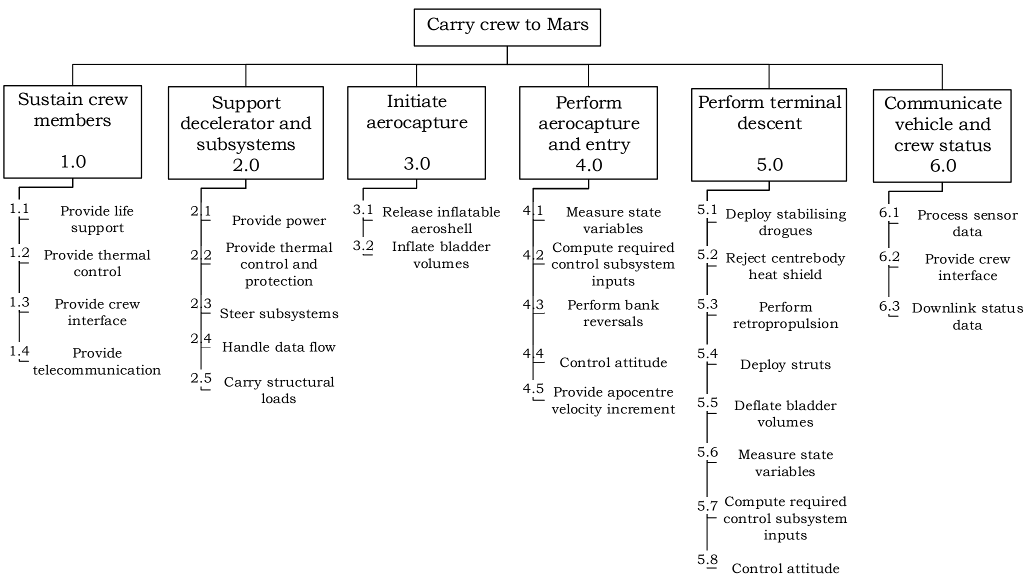

Figure 4.1: Entry vehicle functional breakdown structure

Sequencing the functions of the functional breakdown structure in time yields the functional flow diagram in Figure 4.2. Sequencing of sub-functions 3.1-3.2, 4.0-4.5 and 5.0-5.8 is taken up in the respective sections discussing their design. Sub-functions 1.1-1.4, 2.1-1.5 and 6.1-6.3 are performed continuously.

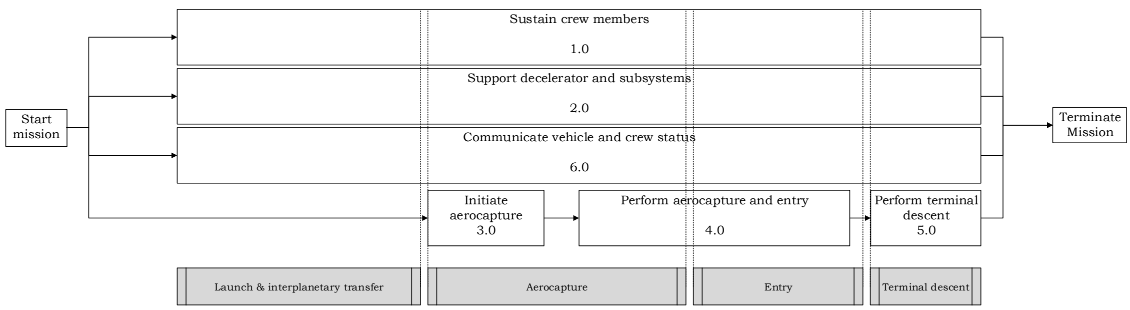

Figure 4.2: Entry vehicle functional flow diagram

4.2 Subsystem breakdown

A tally was made of all the subsystems included in the spacecraft. First a division can be made by distinguishing between the subsystems pertaining to the crew module and those included in the CIA. This division is shown in Figure 4.3. Also shown in Figure 4.3 are all the subsystems included in the crew module and decelerator.

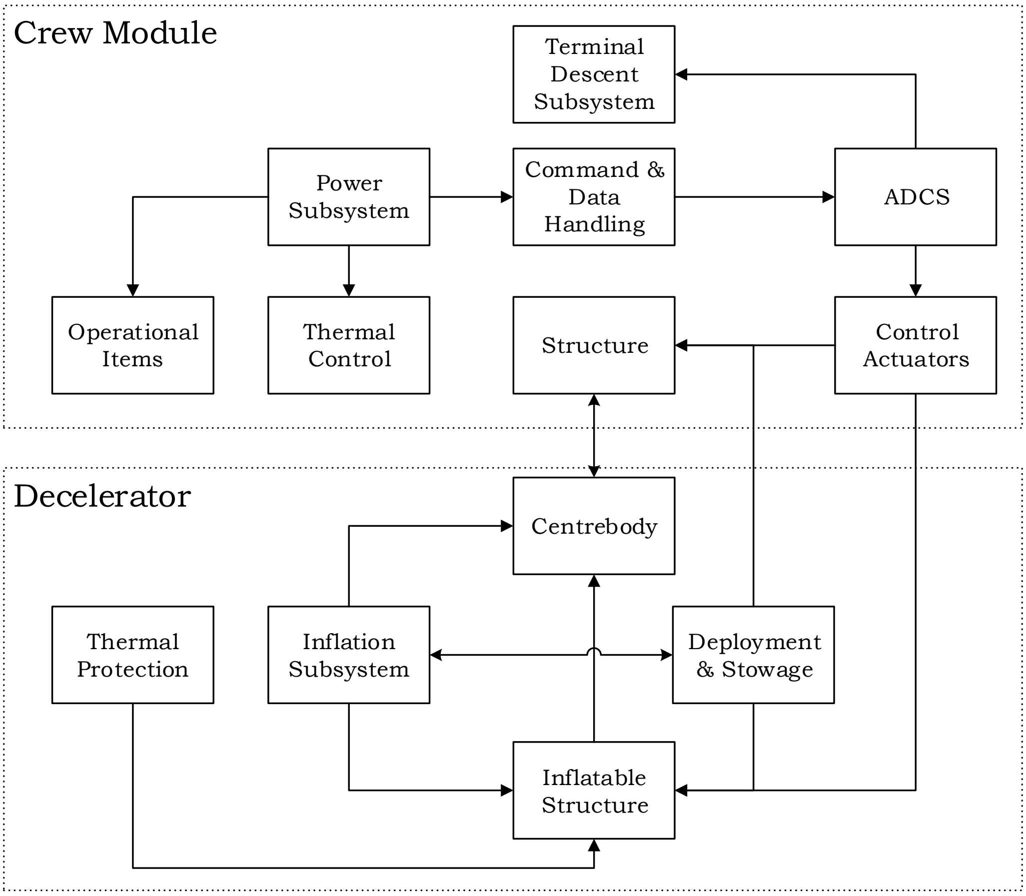

Figure 4.3: Hardware diagram depicting the primary connections between the subsystems

As can be seen from Figure 4.3 connections exist between several of the subsystems, both confined to the decelerator and crew module and between them. In the decelerator the inflation, deployment and stowage systems are closely related with the inflatable structure. The former two are required in order to utilise the stowed inflatable structure to fulfill its mission. The inflation system is located in the centre body. The inflatable structure is stowed against the crew module structure.

While decelerating the TPS has to protect the inflatable structure from the intense heat produced by aerodynamic forces.

The inflatable structure is attached to the crew module structure through the rigid centre body. Control actuators can be attached to both the inflatable and crew module structure. These actuators are managed by the Attitude Determination & Control Subsystem

(ADCS) which receives inputs from the Command & Data Handling (C&DH).
The power system delivers electrical power to the aforementioned C&DH, thermal control system and the operational items. At the end of the aerocapture and entry phase the ADCS provides the attitude control required for the terminal descent system.

4.3 Technical risks

A risk map, as can be seen in Table 4.1, is made in order to identify which elements and components might pose a risk to the mission. Those risks may cause a decrease in technical performance, scheduling overruns or unpredicted changes in mission costs. The risk elements are first listed in Table 4.2, after which they are placed inside a risk map. Each of these elements gets assigned a TRL based on the maturity of the technology that will be used in the corresponding element [23]. On the horizontal axis the consequence of failure is displayed. The TRL-classification is shown in Table 4.3. The elements of this risk map are discussed in the subsequent chapters.

Next to the risk map, precautions have been taken to prevent an increase in design mass over time. To do so contingency factors are introduced to predict mass increments during the design process. NASA has proposed guidelines for contingency factors 4.1. As result, in this preliminary design a mass contingency factor of 20% is taken into account.

Table 4.1: Risk map

TRL 1				
TRL 2				
TRL 3			8	
TRL 4				3
TRL 5			2	1, 6
TRL 6				
TRL 7				4, 5, 7
TRL 8				
TRL 9		9, 12	11	10
	Negligible	**Marginal**	**Critical**	**Catastrophical**

Table 4.2: Risk map elements

Number	Element
1	Thermal Protection System material
2	Thermal Protection System connections
3	Structural materials
4	Structural connections
5	Inflation system
6	Deployment mechanism
7	Decelerator-capsule joints
8	Aerodynamic shape
9	Pressure sensors
10	Bank-control thrusters
11	ADCS thrusters
12	ADCS reaction wheels

Table 4.3: NASA Technology Readiness Level [23]

Technology Readiness Level (TRL)	Description
TRL 9	Actual system "flight proven" through successful mission operations
TRL 8	Actual system completed and "flight qualified" through test and demonstration (ground or space)
TRL 7	System prototype demonstration in a space environment
TRL 6	System/subsystem model or prototype demonstration in a relevant environment (ground or space)
TRL 5	Component and/or breadboard validation in relevant environment
TRL 4	Component and/or breadboard validation in laboratory environment
TRL 3	Analytical & experimental critical function and/or characteristic proof-of-concept
TRL 2	Technology concept and/or application formulated
TRL 1	Basic principles observed & reported

5 Crew module design and sizing

Although the report is centred around the design of a CIA, it is essential that the crew module is designed and sized for the following purposes. Firstly, it is a prerequisite to size control mechanisms as the crew module is a dominant contributor to mass moments of inertia by its large mass. Secondly, it allows for the determination of the number of crew members to be taken on board and thereby to investigate advantages of an inflatable aerodynamic decelerator over the conventional rigid solution, such as Orion. Thirdly and most importantly, it is required to yield a full mission description.

To this end, crew module subsystems are designed and sized at a preliminary design level in Section 5.1. Each subsystem is given and accompanied by power, mass and volume budgets. The latter two allow for packaging of the crew module to effect a Centre of Gravity (CG) location that minimises required control system activity. Crew module subsystem integration is described in Section 5.2. The crew module configuration is carried through to the final design as input for the control system as well as to harmonise a design that integrates crew module and decelerator.

5.1 Subsystem design and sizing

The ADCS, C&DH, operational items (including life support), capsule structure, thermal control and power and the terminal descent system are key components of the crew module. A basic sizing and design follows hereafter.

5.1.1 Attitude determination & control

The general objective for the ADCS is to monitor the attitude of the spacecraft and perform corrections if needed. The operation period of the ADCS can be divided into two phases, the interplanetary phase and the Mars approach phase:

- During the interplanetary flight the ADCS keeps the attitude as required to point the solar arrays toward the sun, points the thrusters in the desired direction and to ensure nominal trajectory is followed.
- During the Mars approach phase the ADCS should adjust the attitude to the entry attitude and compensate for possible disturbances (i.e. inflation of the CIA) to adhere to the nominal trajectory.

Sensors Sensors are needed to determine the attitude. How accurate the sensors need to be depends on the required accuracy from different subsystems. For instance a high gain antenna requires a higher accuracy.

Star trackers Star trackers work by taking pictures of the stars and comparing them to an internal catalogue. They are the most accurate for pointing [24]. However they do not work if the spacecraft is rotating too fast, so an additional rough estimate is needed [8, p. 584].

The mass of star trackers is in the order of $0.1\,[kg]$. The required operating temperature range is $-30\,[°C]$ to $+50\,[°C]$. The average power consumption is less than $0.5\,[W]$.[12]

[12]URL: `http://www.sinclairinterplanetary.com/startrackers` Accessed: 11-06-2015

Gyroscope Gyroscopes can be used to provide the attitude determination for the initial stabilisation. There are different kinds of gyroscopes: Mechanical, optical and so-called Micro-Electro-Mechanical Systems (MEMS). The latter one is relatively new, and is widely used in mobile phones.

Accelerometers Accelerometers are a crucial element for control in the aero capture and final EDL of the entry vehicle. They allow for determination of control model parameters. More details with respect to this are given in Section 7.3.4.

Attitude control During the interplanetary flight the space craft will encounter disturbance torques. To prevent attitude changes, these disturbances must be counter acted. Although the thrusters used during the entry stage of the mission could be used for this, these are only capable of providing bursts of angular momentum. Instead, reaction wheels will be used. These momentum wheels continuously store the disturbance torques. Once they are spun up to their rated angular speeds, they must be unloaded using thrusters. Taking the Mars Reconnaissance Orbiter [25] as a reference case for the required momentum storage and unloading, and scaling these values to be more representative of crew module during interplanetary flight, an angular momentum storage capacity of $H = 1000\,[N \cdot m \cdot s^{-1}]$ and a momentum unloading ΔV of $5\,[m \cdot s^{-1}]$ is needed. Assuming the reaction wheels have a diameter of $0.5\,[m]$ and spin to a maximum of $500\,[rad \cdot s^{-1}]$ each wheel will have a mass of roughly $65\,[kg]$. For a 10 000 $[kg]$ crew module using MR-104G thrusters, a ΔV of $5\,[m \cdot s^{-1}]$ corresponds to a propellant mass of roughly $20\,[kg]$ per Tsiolkovsky's rocket equation.

5.1.2 Command, data handling and telemetry

C&DH and telecommunications form an integral part of the avionics system. These perform four functions: flight and vehicle control, data processing, human interfacing and communications [26]. This requires a direct link to the ADCS module, a link to the telecommunications network and a link to on-board display for crew members. These are illustrated in Figure 5.1.

Critical data flows are those to and from subsystems

Data processing is performed as follows. Data is first filtered, then analysed to see if reactions are required and in case reactions are required put through to the relevant effectors (subsystems) and critical system information communicated to the ground station via the Ka-band (see Section 2.2). Modulation is performed in the transponder by Binary Phase-Shift Keying (BPSK) on the carrier and sub-carrier (modulating the carrier) and Quadrature Phase-Shift Keying (QPSK) on the carrier, similar to the Mars Reconnaissance Orbiter mission [27].

For its integral part, it is key that the system is redundantly equipped to ensure adequate system reliability. To this end, cabling is redundant and safety-critical processing tasks are performed by self-checking pair processors, following their application in Orion [26]. These self-checking pair processors observe and compare the activity of their partner to identify faulty behaviour. Moreover, watchdog units are applied that identify faulty components (as applied in e.g. the SeaStar Satellite[13]).

[13]URL: `http://digitalcommons.usu.edu/cgi/viewcontent.cgi?article=2198&context=smallsat`. Accessed: 22-06-2015

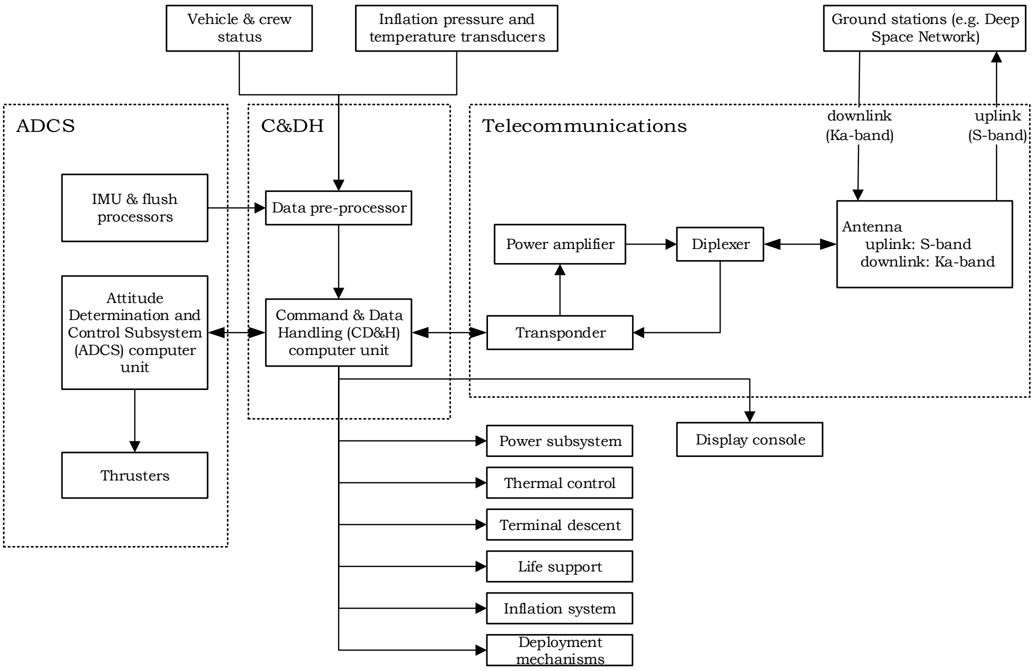

Figure 5.1: Communication flow

Antennas used can be extracted from a reference mission to Mars, for example the Mars Reconnaissance Orbiter [27]. This mission had relatively high scientific return communications and used a 3 $[m]$ diameter high gain antenna and two low gain antennas. The communication system for this mission was remarkable because it was able to send data back to Earth more than ten times faster than previously conducted missions. Such a high return would be highly beneficial for the manned mission at hand to maximise ground surveillance possibilities and accurate monitoring. It similarly used Ka-band communication for downlink. To this end, the communication system is deemed a good reference system for use in the mission at hand.

The mass of the C&DH subsystem is extrapolated from that in the Mars Odyssey mission by scaling with the ratio of masses. For an 11.1 $[kg]$ C&DH subsystem mass in the 376 $[kg]$ Mars Odyssey[14], this translates to nearly 300 $[kg]$ on the 10 000 $[kg]$ entry vehicle at hand. The validity of this estimate is confirmed to some extent by empirical C&DH mass estimation for interplanetary missions, showing relative proportionality with vehicle mass (indicated by a sample standard deviation that is relatively low with respect to the sample average) [8, p.953].

The telecommunications system, extrapolated from the Mars Reconnaissance Orbiter, has a mass of 108 $[kg]$, which is not scaled since the sizing thereof is not deemed mass-dependent. Taking into account a contingency for the larger crew module and more demanding mission at hand, the C&DH and telecommunications mass is estimated at 530 $[kg]$, thus taking a 30% contingency into account. In addition, cabling requires additional contingency, taken to be 10% and a mass of 53 $[kg]$.

[14]URL: `http://mars.nasa.gov/odyssey/mission/spacecraft/parts/command/`. Accessed: 11-06-2015

5.1.3 Operational items

In this section the operational items are sized. This can be summarised as the mass needed by the astronauts to live under reasonably comfortable conditions in the crew module during the mission. For this purpose the paper by Tito et al. has been used [28]. In this paper the operational items are called Environmental Control and Life Support System (ECLSS). First the method for estimation is described with its assumptions. Followed by the results of the estimation.

Estimation method The mass of the ECLSS is primarily driven by the crew size and mission length. The ECLSS is divided into subsystems: Air Management, Thermal and Humidity Management, Water Management, Waste Management, Human Accommodation, Food Preparation and Storage. Each of these subsystems can be subdivided into components. Examples of these are a water heater or packed food in the Food Preparation and Storage. It is evident that some components scale with the key drivers and others do not. For example, adding a crew member does not necessitate an extra water heater, but it does require extra packed food.

Taking this into account the mass has been divided into two components. A basic system mass which scales with crew size and the consumable mass that scales with crew size and mission length. Examples of components that belong to the basic system mass are oxygen scrubbers (not including oxygen), atmospheric control systems and food preparation systems. Examples of components that belong to consumable mass are oxygen, food, water and personal provisions. The used reference by Tito et al. incorporates the mass for the Thermal Control System (TCS) [28]. It is assumed that this TCS mass only provides the thermal control for the operational items. The TCS for other subsystems is discussed in Section 5.1.5.

Results By using the method described in the previous paragraph the results of Table 5.1 were obtained.

Table 5.1: Obtained masses and volumes of basic system & consumable items

Crew members	**Basic system mass [kg]**	**Basic system volume [m^3]**	**Consumables mass per day [kg]**	**Consumables volume per day [m^3]**
1	1800	4.88	3.2	0.018
2	2500	6.78	6.4	0.036
3	3200	8.68	9.6	0.054

It can be seen from Table 5.1 that both the basic system and consumables mass scale with the number of crew members. By using linear extrapolation the mass and volume associated with crew members higher than three can be determined. These are shown in Table 5.2 for a mission time of 100 days, which incorporates the transfer from Earth to Mars and the maximum deceleration time. Herein the TCS mass for the operational items comes down to 480 $[kg]$.

Table 5.2: Total mass and volume associated with operational items for varying crew numbers

Crew members	Operational items mass [kg]	Operational items volume [m^3]
1	2120	6.69
2	3140	10.40
3	4160	14.11
4	5180	17.82
5	6200	21.53
6	7220	25.24

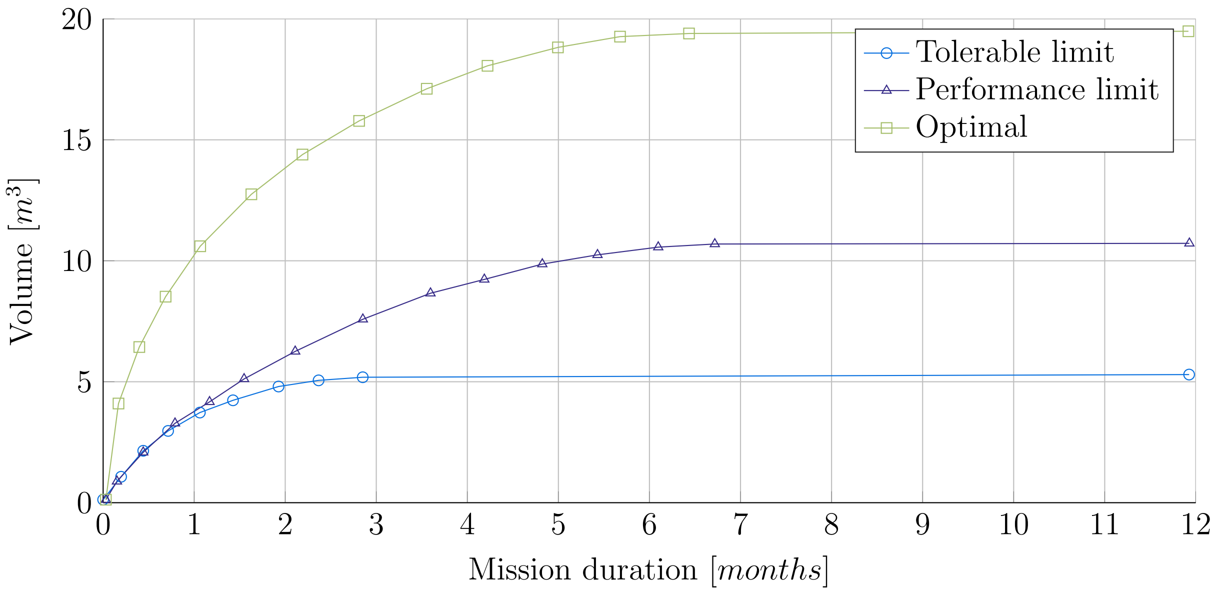

Figure 5.2: Habitable volume per crew member as a function of mission duration [29]

Furthermore Rudisill et al. mention the spacecraft volume required for crew operations per crew member [29]. This volume can take on three different values depending on the mission length. The resultant habitable volumes are shown in Figure 5.2.

In the remainder of this report the crew habitable volume will be sized to the 'performance limit' indicated in Figure 5.2.

5.1.4 Capsule structure

The structure of the crew module serves the important function of connection all the individual subsystems of the crew module and moreover connects with the CIA. The main scope of the design described in this report lies within this CIA. New advances from for example the currently being developed and Orion mission are therefore not considered. The Orion capsule can already be considered state of the art and is in a large amount representative for the crew module design.

A schematic layout as for example also used in the Orion spacecraft[15], features an aluminium grid structure. This structure encloses the pressurised volume inhabited by the

[15]URL: `http://www.spaceflight101.com/orion-spacecraft-overview.html`, Accessed 11 June 2015

astronauts. The grid structure allows for easy attachment of the individual subsystems. Subsystems which require pressurisation, typically those involving the astronauts can be placed within in this shell, whereas the systems that do not require pressurisation are placed on the outside of this shell. A more detailed analysis on where each of these individual subsystems are placed is discussed in Section 5.2.

A full estimate of the structural mass is only to be provided in later design phases. More detailed structural estimates are typically provided by detailed Computer Aided Design (CAD) models and Finite Element Method (FEM) models [8]. A rough estimate can be provided on the basis of previous reference missions. NASA's Orion mission is again of primary interest as it also features astronauts. Some differences with respect to the structural elements thereof can however be noted:

- Orion incorporates an integrated heat shield and structure
- Orion features a backshell. This is not required for the CIA because of its larger deployed diameter which shields the capsule from the oncoming flow

In the design at hand the heat shield structure is incorporated in the CIA. The crew module is merely connected to this CIA of which the latter is designed in more detail in the remaining chapters of this report. Due to the implementations of the CIA an additional backshell structure is also no longer required. The back shell normally functions a protection against thermal loading which moves sideways along the body. Using the large frontal of the inflatable this is prevented, denoting one of the advantages of using an inflatable structure [22]. The crew module structure should however also be sized considering , and may as such not be too tall and may feature a tapered end such that the crew module is not exposed to thermal loading passing the CIA.

For this reason the heat shield carrier structure of around 1500 $[kg]$ [30] is not taken into account into the mass estimate of the structure. A total structural mass for manned re-entry vehicles lies at around 30%. The manned Apollo mission featured a 31% structural mass fraction [16] including a heat shield structure. Extrapolating this value, with a 9000 $[kg]$ crew module mass yields a structural mass of 1300 $[kg]$, excluding the heat shield structure. This is in line with values suggested by Wertz et al. [8]. Taking into account a 30% mass contingency factor yields a final structural mass estimate of around 1700 $[kg]$. A similar mission featuring a descent towards Mars from 7 $[km \cdot s^{-1}]$ has a structural mass of 517 $[kg]$ on a dry mass of 2863 $[kg]$ including contingency factors[17]. Scaling this value yields a similar mass estimate of around 1800 $[kg]$.

The connection between the crew module and the CIA is taken into account in the capsule structural mass estimate of 1300 $[kg]$.

5.1.5 Capsule thermal control

Whereas the TPS is used to protect the crew module from excessive heating during the aerocapture and entry, the TCS is used to keep other subsystems in the crew module within their operating temperature limits. It is assumed the entry phase does not impose extra requirements on the TCS as it is completely covered by the TPS. Note that this only

[16]URL: `http://braeunig.us/space/specs/apollo.htm`, Accessed 11 June 2015

[17]URL: `http://www.nasa.gov/pdf/458812main_FTD_AerocaptureEntryDescentAndLanding.pdf` , Accessed 11 June 2015

holds when the angle of attack (α) is low enough such that the crew module stays out of the wake. Furthermore, in the paper by Tito et al. the mass estimation for the operational items already assigns a mass for the thermal control within the living compartments of the crew module [28]. Tito et al. calculate a mass of 480 $[kg]$ for a crew module suitable for the life support of two astronauts. Therefore this part only focuses on the thermal control of components that are not placed within the living compartments.

Examples of these components that need to operate at the edge or outside of the crew module are star trackers from the ADCS or the antennas from the telecommunications. To provide typical temperature limits Table 5.3 is provided [8, p.686]. In here there is a distinction between operational and surviving temperatures. From this table it is evident that components that operate outside the spacecraft can typically handle a wider temperature range than components that operate within the crew module.

Table 5.3: Typical temperature requirements for different components

Equipment	**Operational range [°C]**	**Survival range [°C]**
Avionics Baseplates	-20 – 60	-40 – 75
Batteries	10 – 30	0 – 40
Hydrazine Fuel	15 – 40	5 – 50
Solar Arrays	-150 – 110	-200 – 130
Antennas	-100 – 100	-120 – 120
Reaction Wheels	-10 – 40	-20 – 50

In order to keep the subsystems within their operative temperature range the TCS uses different tools and techniques. According to Karam the most commonly used are coatings, insulators and isolators, heaters, louvres and heat pipes [31]. For this stage of design of the crew module it is deemed sufficient to only provide a mass estimate for the TCS mass.

The TCS mass ranges from 3% to 10% with an average of 6% for the dry mass of an interplanetary spacecraft [8, p.953]. Note that these spacecraft are not designed to carry astronauts, therefore it is assumed that this 6% adds on top of the 480 $[kg]$ calculated in Section 5.1.3. This would add an extra 600 $[kg]$ dedicated to the TCS.

5.1.6 Capsule power

In order to successfully operate the mission during the Earth to Mars transfer including the EDL phase, several components require electrical power supply and management. Although multiple energy sources exist, photovoltaic energy is already a known and widely applied technology. Also, during the interplanetary transfer, sunlight will almost always be available. Therefore, photovoltaic energy will be used as the primary energy source.

Before performing an aerobrake however, solar panels must obviously be retracted. Hence, during the EDL phase the vehicle will run on batteries. When the vehicle goes into an orbit around Mars, the solar arrays can be re-deployed in order to recharge the batteries. This will reduce the energy demand as well as battery mass.

Several elements require a constant power supply. Among these elements are the life support system, thermal contact system, a galley, airlock, communications, personal quarters, command centre, health maintenance facility, data management system, audio & video facilities, a science lab, hygiene, vehicle control and the propulsion system. NASA has made an estimate for a 30 $[kW]$ power system for a crew of six with a corresponding mass of 500 $[kg]$, taking into account the power system efficiency [13]. Yet, the current mission is only designed for one or two members. By linearly scaling down all crew-dependent elements, the power required can affectively be reduced to 16.7 $[kW]$. Assuming that the power need scales linearly with the total mass of the power subsystem, this will result in a power subsystem mass of approximately 280 $[kg]$.

5.1.7 Terminal descent system

Terminal descent takes place in the following sequence, depicted schematically in Figure 5.3.

1. The rigid heat shield, joined in the middle by a bolt-and-nut assembly, is separated by redundant pyrotechnic cutters. The two halves are held fixed by locking actuators to prevent interference with exhaust flow and inflatable.
2. At this altitude, retro-propulsion is activated and the thruster provides the decelerating force in combination with the inflated CIA.
3. At an altitude of 50 $[m]$, struts are partially deployed from their stowed position such that the pads rest above the inflatable. At the same time, the vent in the inflation system is opened and inflatable bladders deflate. Upon full deflation, measured by pressure transducers in the inflation system, the struts deploy further such that the pads are level with but below the thruster nozzle exit and achieve a roughly 90 $[deg]$ inflatable half-cone angle.
4. The thruster is then deactivated and the crew capsule lands on the inflatable, on which the landing gear pads rest.

Retro-propulsion is used for the beneficial aerodynamic interaction with a CIA [10], effecting a required specific impulse that is twice as low as otherwise. This effects a smaller propellant mass required. The inflatable is not rejected, but rather deflated, because rejection would require a separation mechanism to prevent interference with the crew capsule. Deflation does induce, however, the risk that it is not performed reliably. In such a case, a risk mitigation plan could be deliberate puncturing of the inflatable bladder volumes in order to deflate it.

The final design of the terminal descent stage of the mission is chosen to consist of retro-propulsion deceleration, using 3 rocket engines that total 500 $[kg]$ dry mass, with a 680 $[kg]$ fuel usage throughout terminal descent and a corresponding propellant tank mass of 45 $[kg]$. The landing gear has an estimated mass of 200 $[kg]$ and will be deployed while still above the Martian surface. Following landing gear deployment the inflatable structure is deflated to make it lose its stiffness and allow the landing gear to touch the ground. The stabilisation drogue parachutes have a mass of 20 $[kg]$. Adding up the component masses gives the total terminal descent mass of 1445 $[kg]$.

The terminal descent system consists of the thruster system that decelerates the spacecraft from Mach 5 at 15 $[km]$ height to zero velocity at the Martian surface. The thruster should

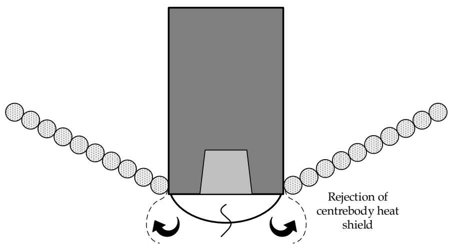

(a) Retro-propulsion activation

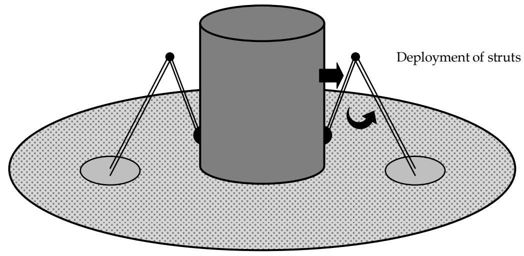

(b) Strut deployment

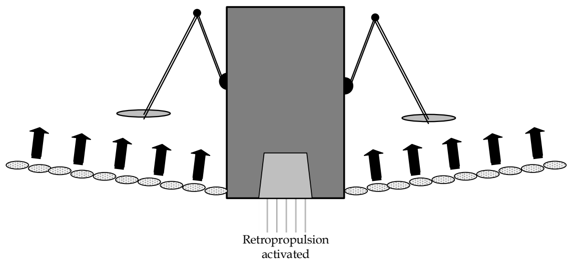

(c) Decelerator deflation

Figure 5.3: Terminal descent activity sequence

be placed in the centre body and pointed in the forward direction, such that the positive interaction between aerodynamics and the thruster plume is made use of. The total terminal descent mass, including thruster, fuel, landing gear and drogue parachute, is estimated to be approximately 1445 $[kg]$.

5.2 Crew module configuration

Space allocation of the subsystems described in the previous section, as well as crew members, is performed with the goals of:

- Accommodating subsystems necessary to support interplanetary flight and entry
- Providing crew members with a habitable volume and operational items to support a flight duration of approximately 100 days
- Keeping the axial position of the CG forward to lower pitch stability and alleviate pitch control performance in the final mission phase
- Allowing for packaging freedom in achieving a static lateral CG-offset for creating an asymmetric lifting shape

To this end, the crew module is packaged as depicted in Figures 5.4, 5.5 and 5.6.

The top part is required to contain drogues to stabilise the entry vehicle in its final descent phase. Four drogues are placed to incorporate redundancy and provide a symmetric configuration, to prevent excessive tilting during final descent. Moreover, the top part contains the foldable solar arrays required to generate power required during interplanetary transfer. These are placed in the top part to prevent interference with firstly the exhaust flow from thrusters and secondly the stowed inflatable before entry on the other hand. A high-gain antenna of adjustable attitude on a boom enables communication during all mission phases. Thrusters for the apoaerion boost are mounted on top, of 0.41 [m] length. Therefore the length of the top part is estimated on the basis hereof to be 0.50 [m] length.

Crew members are located in the next part, a habitable volume to their availability that is dictated by the performance limit for a three-month mission duration as 11 [m^3] per crew member [29]. The diameter of the habitable volume is 4.0 [m], thereby less than vehicle maximum diameter to accommodate four propellant tanks, one per quadrant. Propellant tanks allow intertank propellant transfer to maintain the lateral CG position. The tanks are sized on the basis of the total required propellant and provide propellant for both the reaction control thrusters, apoaerion boosters and retro-propulsion thruster assembly. The length of this part follows from the habitable volume and depends on the number of crew members. For two crew members, it is 1.75 [m] long. Including a 0.25 [m] contingency for an aft pressure bulkhead yields an estimated length of 2.00 [m].

Operational items are located within reach of crew members. These are placed at this location because of their relatively high mass and therefore contribution to the axial CG position. The total volume occupied follows from Table 5.2. On one hand these operational items include relatively dense products, foremostly the life support systems, and less dense products in the form of food and other supplies. The length of this part follows from the required volume for operational items, for two crew members equal to 0.75 [m]. Including a forward additional bulkhead yields an estimated length of 1.00 [m].

Four struts for touchdown, packed symmetrically. The struts are arranged about the batteries required to provide power during entry, when solar panels are stowed, and the main thrusters for retro-propulsion. The length follows from estimates for the strut required volume and the retro-propulsion thrusters of 2.30 [m] length. It is an estimated 2.0 [m], as part of the thruster is contained within the last part.

The last part contains the thruster nozzle, closed off by a heat-resistant end-cap during entry, a nitrogen tank and inflation system, and the attachment rings for the inflatable decelerator. The end-cap is to be eject-able. The length of this part is mainly dictated by the shape of the inflatable and where it attaches to the centre body. For a 12.0 [m] deployed diameter, it is approximately 1.0 [m] in length.

This yields a total vehicle length of an estimated 6.5 [m]. This fits within SLS fairing constraints and moreover ensures that the crew module is not impinged by the flow.

Component masses are as listed in Table 5.4. Due to the relative large mass of items closer to the CIA the axial CG position is estimated closer than 3 [m] from the CIA attachment point. A more elaborate estimate is without value, for the actual packaging of the crew module requires a more thorough design beyond the mission scope. However, to investigate the feasibility of achieving the required CG-offset, it follows from Figure 7.19 that the required CG-offset is below 0.5 [m]. Such an offset can be affected primarily by shifting the relatively heavy contributions of operational items. Placing the CG thereof 1.5 [m] from the axial centreline and assuming a symmetric configuration otherwise yields an approximate 0.5 [m] lateral CG-offset. Considering the 4.5 [m] diameter allocated to operational items, this is feasible.

Table 5.4: Crew module mass budget

Component	**Component mass [kg]**
Power	280
ADCS	225
Thermal	600
Structural mass	1300
Operational items	3140
Crew	160
Terminal descent	1445
C&DH	585
Other	815
Total	**8550**
Margin (5%)	450
Capsule mass	**9000**

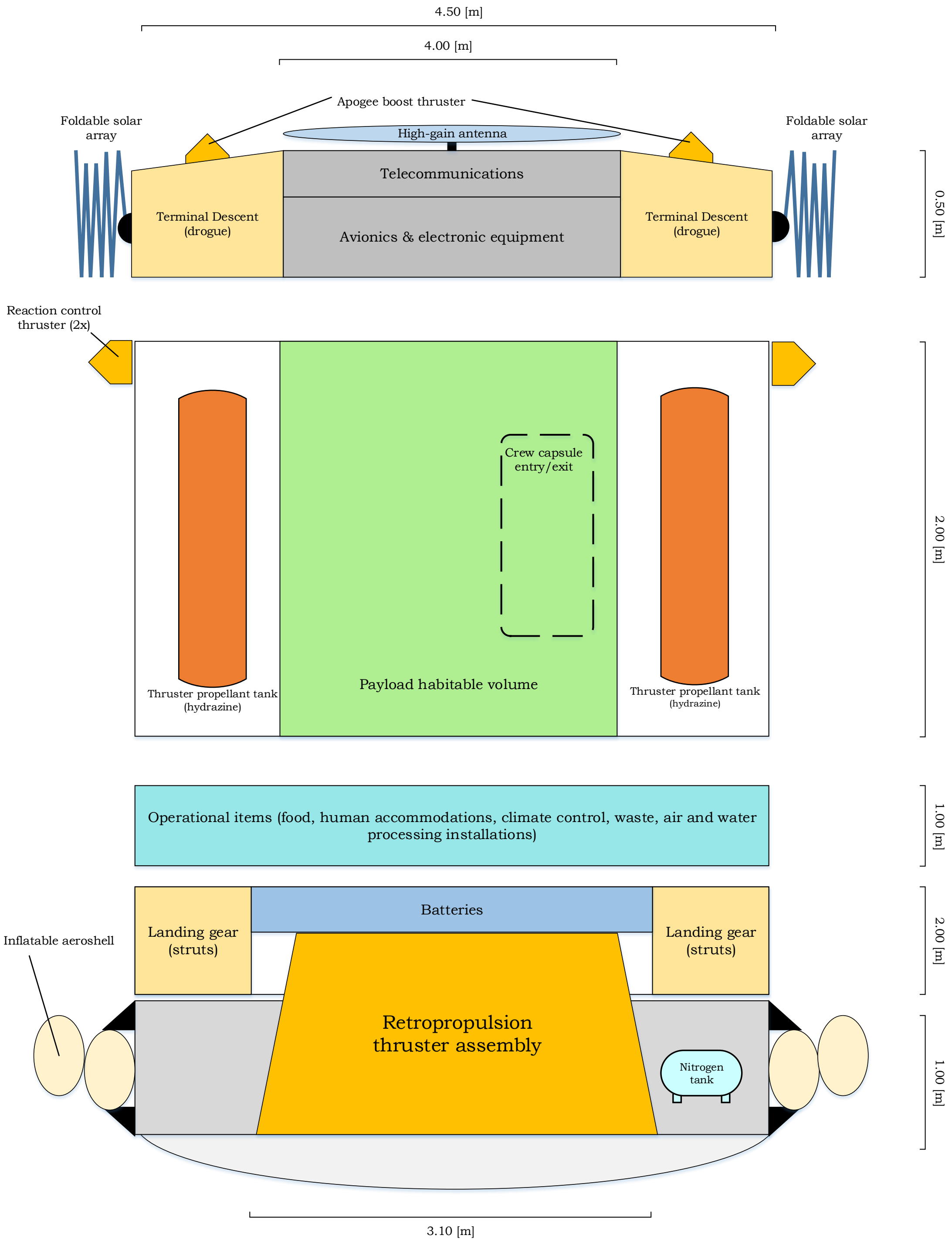

Figure 5.4: First axial view of crew module lay-out. Space allocation only, drawing not to scale.

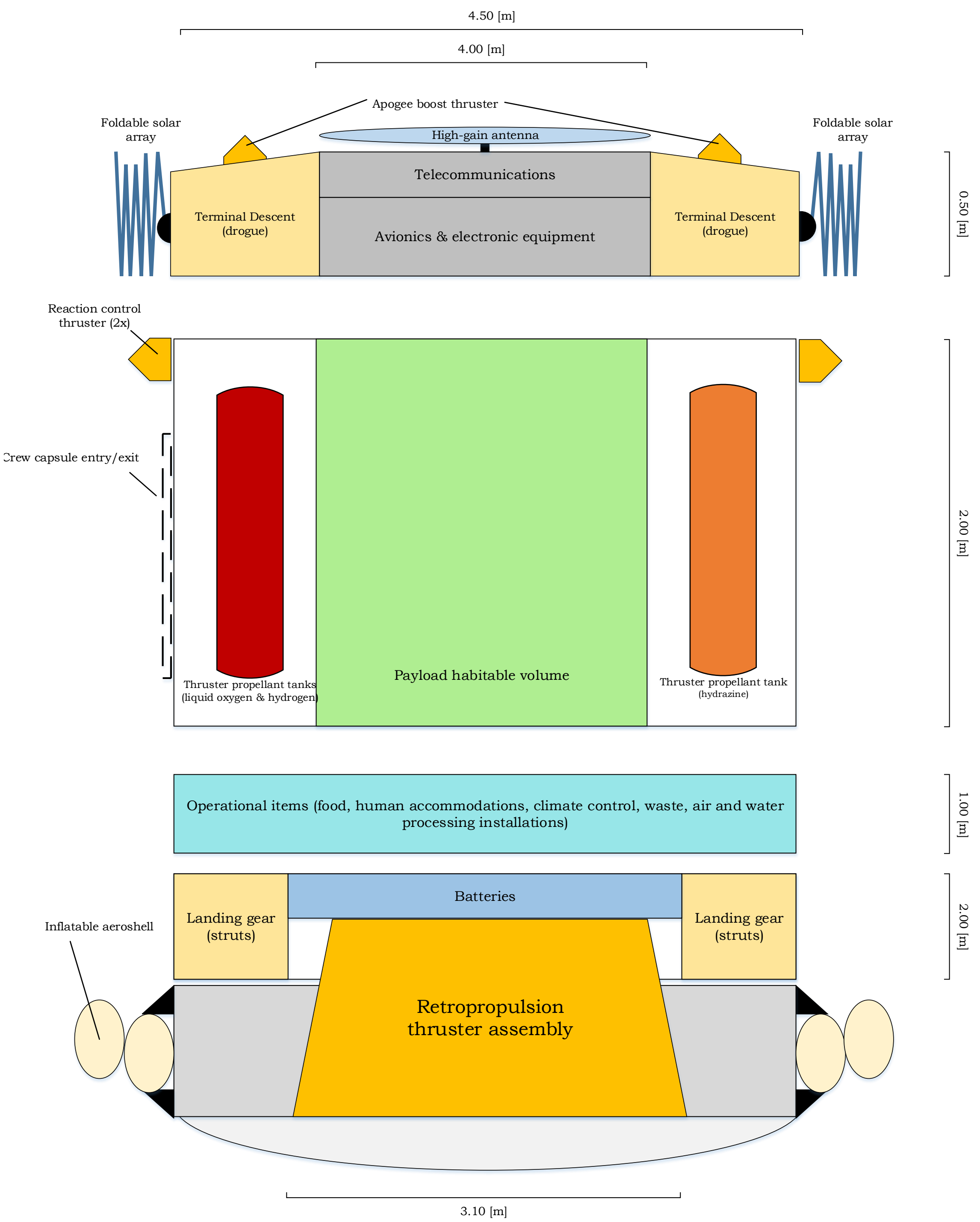

Figure 5.5: Second axial view of crew module lay-out. Space allocation only, drawing not to scale.

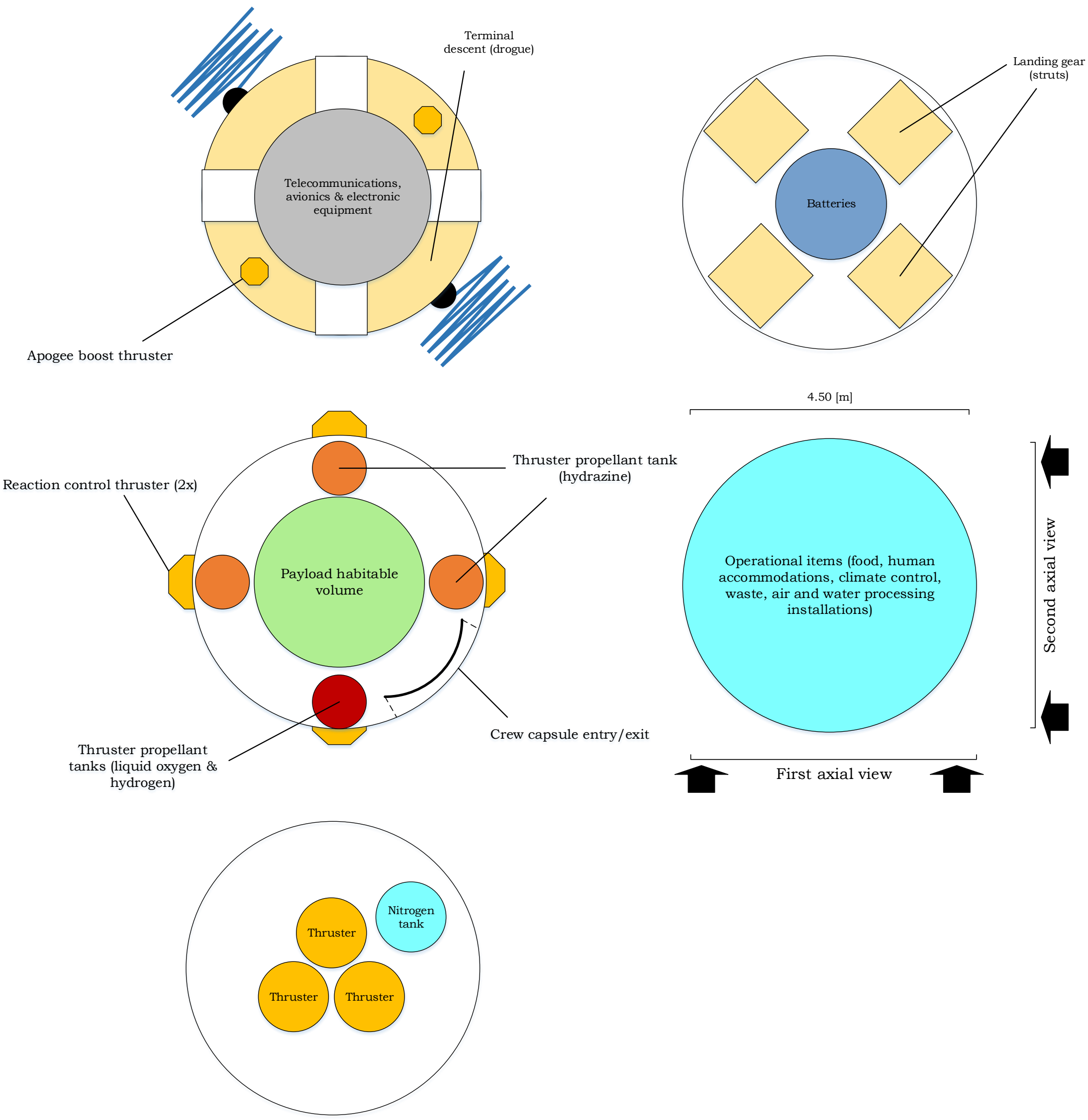

Figure 5.6: Top-down view of crew module lay-out. Space allocation only, drawing not to scale.

6 Design parameters and tool analysis

It is essential for the iterative design process that the design sensitivity is investigated. This sensitivity is quantified by tools for trajectory, thermal structural and aerodynamic analysis. These tools are complemented by a control system tool for the purpose of control system design and sizing. The description of these tools is given in Section 6.1 and their output in Section 6.2.

6.1 Design tools

Subsequent sections describe the trajectory, aerodynamic, control, thermal and structural analysis tools. A brief overview of the underlying principles, assumptions and in- and output is given.

6.1.1 Trajectory analysis

Input and output As input the tool requires the entry velocity, flight path angle at the boundary of the atmosphere, an aerodynamic model (C_L and C_D as a function of α), an α-profile (changes in the angle of attack during the aerocapture and entry), and a μ profile (changes in the bank angle during the aerocapture and entry).

As output the trajectory tool can generate important parameters at each moment in time. The most important parameters are: location ($\mathbf{R}$), acceleration ($\mathbf{a}$), dynamic pressure (q_∞), velocity ($\mathbf{V}$), Mach number (M), atmospheric temperature (T_∞) and atmospheric density (ρ_∞).

Assumptions Some of the assumptions have a big impact, these are the primary assumptions. There are, however, also some assumptions that have a negligible effect on the results. These are the secondary assumptions.

Primary assumptions

- All atmospheric properties only vary with the height above MOLA and not with longitude, latitude or time. These variations are shown in Appendix C.
- All trajectories are assumed to only occur in the equatorial plane. This means that the latitude is always $0\,[deg]$. Changing the latitude will have a big impact on the relative speed of the Martian atmosphere.
- The gravitational pull is assumed to only vary with the height above MOLA. The gravitational field of Mars is however not uniform over longitude and latitude, this will induce errors in the trajectory as gravity is one of the major forces in the analysis.
- The bank reversals needed for bank control are assumed to be instantaneous.

Secondary assumptions

- The spacecraft is assumed to only feel a gravitational pull from Mars. It is thus assumed that there is no gravitational pull from the sun, any other planet or the Martian moons.
- The atmosphere stops at an altitude of $400\,[km]$. At this point the atmosphere is negligibly thin, expanding the atmospheric model would not contribute to the results.
- The effect of other disturbances i.e. solar radiation is neglected.

Analysis method The trajectory can be divided into two different parts, one part is the pass through the atmosphere and the other is outside of the atmosphere. In the first part, there are three forces working on the spacecraft: Lift, drag and gravity. In the second part there is only the gravitational force.

The part outside the atmosphere is simplified by using the Kepler equations of orbital motion to determine the position of the spacecraft over time.

The atmospheric properties are determined using the NASA software Mars-Global Reference Atmospheric Model 2010 v1.0 (Mars-GRAM). The software generates data based on equations for atmosphere properties and incorporates the high amount of dust on Mars, which has a big effect on the absorbed radiation heat from the sun. From this model the average atmospheric properties are used to determine the aerodynamic forces. All data used from Mars-GRAM is shown in Appendix C.

Using the aerodynamic forces combined with the gravitational pull from Mars the accelerations are calculated. These accelerations are integrated twice to obtain the velocity and the location.

Limitations The tool is mainly limited by the 1D implementation of the atmospheric properties and gravity model. This means that no variations of the atmosphere over longitude, latitude or time are considered. It is recommended to implement the full atmospheric model in later stages of the design. The use of a numerical simulation only introduces a small error. The full verification and validation are done in Appendix A.1.

6.1.2 Aerodynamic analysis

The design of the entry vehicle requires an analysis of the aerodynamic properties of the vehicle. Although high fidelity solutions which describe the entire flow field around the vehicle exist, these are prohibitively expensive in both runtime and computational resources for the design study at hand. A low fidelity tool has been developed to allow for rapid design iterations.

Input and Output For a given external shape, the aerodynamic analysis tool provides aerodynamic lift, drag and moment coefficients for ranges of angles of attack and angles of sideslip. This is used in the trajectory analysis and the stability & control analysis of the entry vehicle. It also calculates the heat flux in the stagnation point for a given flight condition and vehicle shape. The heat flux is required for the analysis of the TPS.

Analysis method The aerodynamic analysis is based on modified Newtonian flow theory. This theory relates the pressure coefficient on a given surface C_p with the incidence angle χ this surface has with respect to the freestream. The equation for pressure coefficient is given in Equation 1, while the maximum pressure coefficient can be calculated using Equation 2 [32].

$$C_p = C_{p,max} sin^2(\chi) \tag{1}$$

$$C_{p,max} = \frac{2}{\kappa M_\infty^2}\left(\frac{p_{O_2}}{p_\infty} - 1\right) \tag{2}$$

These pressure coefficients can then be integrated to find the force and moment coefficients acting on the vehicle. The local change in static pressure due to the aerodynamic effects can be found by multiplying C_p by the dynamic pressure $q = \frac{1}{2}\rho_\infty V_\infty^2$. This method provides reasonable accuracy in determining the pressure coefficient distribution over blunt bodies for a low computational cost. It is therefore well suited for initial design studies such as the one performed in this report [32].

The heat flux in the stagnation point is calculated using the method developed by Tauber et al. [33]. Equation 3 gives the heat flux in the stagnation point. This equation uses the ratio between the wall temperature and the temperature in the stagnation point in the flow, which can be calculated using Equation 4 [32].

$$\dot{q}_s = 1.83 \times 10^{-8} \rho_\infty^{0.5} V_\infty^3 r^{-0.5}\left(1 - \frac{T_w}{T_0}\right) \tag{3}$$

$$T_0 = T_\infty \frac{\kappa - 1}{2} M_\infty \tag{4}$$

Limitations The modified Newtonian flow method is more accurate for high incidence angles with respect to the flow [32]. As described in Chapter 3, the body to be analysed is a blunt body, which limits the impact of this loss of accuracy since the majority of the body is at a high incidence angle to the flow. The method will not produce accurate results below a Mach number of 5, since at lower Mach numbers the forces on the entry vehicle will no longer be dominated by pressure drag. This will invalidate the modified Newtonian theory [32]. Since the part of the mission that is analysed in-depth in this report ends at a Mach number of 5, the analysis will not be influenced.

Optimisation An optimisation algorithm is implemented that allows for a single or multiple objective shape optimisation. To this end, the aerodynamic shape is parametrised to allow optimisation using genetic algorithms as implemented in MATLAB. This parametrisation is done by choosing the coefficients of a polynomial such that it represents the external shape of the CIA. This polynomial is then revolved around an axis to obtain the 3D shape of the CIA. Furthermore, the height and skewness are optimisation parameters as well. The genetic algorithm searches for a minimum of a certain function, which can be chosen to be an aerodynamic performance parameter such as the drag or moment. It tries different combinations of coefficients of the polynomial, assesses their performance according to the objective and combines the best performing specimens into even better specimens. Furthermore constraints can be given, such as a requirement on lift-to-drag ratio or static stability. Optimisation can then be used to efficiently search the multi-dimensional design space for the global optimum, given constraints and one or multiple objectives such as a maximum drag or minimum heat flux.

Concluding remarks The aerodynamic analysis is capable of calculating the pressure distribution on the surface, the lift, drag and moment coefficients of an arbitrary body as well as their derivatives with respect to angle of attack and sideslip. It is also capable of calculating the heat flux in the stagnation point. Verification and validation have been performed to ensure the consistency and accuracy of the method. Details on this can be found in Appendix A.2.

6.1.3 Control system analysis

The control systems should be able to keep the spacecraft on the trajectory as defined by the trajectory tool in Section 6.1.1.

Stability The aerodynamic tool determines the static stability around all axes in the aerodynamic frame. If the spacecraft is stable around a certain axis all perturbations around said axis are automatically counteracted. However, if an attitude change around that axis is required a larger moment has to be counteracted to control the spacecraft. If the spacecraft is unstable around a certain axis perturbations around that axis have to be counteracted by active control. However, if an attitude change around that axis is required a smaller moment has to be counteracted to control the spacecraft. It is thus preferable to perform control about the axes that are neutrally stable, or even unstable, and axes about which no control is needed are preferred to be stable. Following from the aerodynamic analysis the stability around all three axis can be considered. For pitch and sideslip the entry vehicle was found to be stable whereas for roll the vehicle is neutrally stable.

Available control systems The control systems that are considered are active CG-offset control, thrusters and aerodynamic surfaces respectively.

Active Centre of Gravity-offset control In order to be able to trim the spacecraft at a certain angle of attack (α) a constant control moment has to be delivered by the combined control systems. To achieve this an active CG-offset control system is considered. By changing the location of the capsule CG with respect to the aeroshell the magnitude of the resultant moments changes [34].

The aerodynamic forces acting on the spacecraft work on the centre of pressure of the aeroshell. The CG of the spacecraft has a certain offset in the X, Y and Z-directions with respect to this centre of pressure. Thus moments are induced around the CG. Knowing these moments a line in 3D space can be found on which all moments are zero. This line varies for different combinations of forces which follow from different combinations of angle of attack, sideslip and bank angle.

Thrusters By dividing the required reaction control moment around a certain axis (M_{aero}) by the length of the thruster moment arm (d) the required thruster control force ($\mathbf{F}_{req}$) can be determined, as is done in Equation 5. From the specific impulse of a thruster (I_{sp}) and its propellant mass flow ($\dot{m}$) follows the amount of thrust and control moment each thruster can generate, as is done in Equation 6 [35].

$$\mathbf{F}_{thrust} = I_{sp} g_e \dot{m} \tag{5}$$

$$\mathbf{F}_{thrust} = \frac{M_{control}}{d} \tag{6}$$

Where g_e is the gravitational acceleration on Earth. Solving the preceding for $\mathbf{F}_{req} = \mathbf{F}_{thrust}$ and by summing the mass flow over time the total propellant mass can be obtained. This relation is shown in Equation 7.

$$m_{prop} = \int_0^t \frac{M_{control}}{I_{sp} g_e d} dt \tag{7}$$

Since a constant mass flow is needed to be able to deliver a continuous control moment thrusters are not considered to be used to trim the spacecraft at a certain angle of attack. A continuous control moment is needed to overcome the stability around the α axis. Doing so would result in an excessively high propellant mass.

To arrive at a thruster design the specific impulse and maximum mass flow of available thrusters can be taken from literature. From this also follows the dry mass per thruster, which can be added to the propellant mass to arrive at the total thruster control system mass.

Thrusters allow for very versatile operations but with varying efficiency. The effectiveness of attitude changes depends on the stability of the vehicle. If the entry vehicle is stable around a certain axis large amounts of propellant are required to maintain a certain attitude. Again, any trimming around such an axis is not feasible.

The neutral stability of the entry vehicle can be used relatively efficiently for bank control. This is the conventional solution for guidance & control during entry. The use of thrusters implies a high control system reliability as they are not only frequently employed but also allow for redundant placement with a minimal mass increase. As such a high control system reliability can be achieved in line with the mission requirements. Moreover the use of thrusters allows for a relatively fast control system. Peak rotational rates are in the order of $20\,[deg \cdot s^{-1}]$ and $5\,[deg \cdot s^{-2}]$ [36].

The use of bank control for Martian landings has previously been found [36] to achieve accuracies of up to $10\,[m]$ at final landing featuring a Hypersonic Inflatable Aerodynamic Decelerator (HIAD) with a combined mass of over $10\ 000\,[kg]$.

Outside the Martian atmosphere thrusters feature the additional advantage that unlike an active CG-offset control system or body flaps control is system possible since the presence of an atmosphere is not a perquisite.

The main disadvantage of thrusters over body flaps or an active CG-offset control system is an increasing control system mass as the thruster usage increases. If the thrusters are employed frequently the propellant mass increase can become significant, negating the aforementioned advantages.

Aerodynamic surfaces Using the modified Newtonian flow theory discussed in Section 6.1.2 the force and moment contributions of a surface with a certain orientation to the freestream flow can be computed. For an aerodynamic surface (essentially a flap) the freestream inclination angle can be varied by using rotational actuators. Alternatively the flap area exposed to the freestream flow can be varied by using linear actuation. Both of these options directly influence the pressure distribution over the CIA surface. This induces a moment around the required axis, thereby allowing for active control.

The required control moments can be determined in a manner similar to as was done for thrusters. By comparing the required and delivered control moments the required force per flap can be computed. From this force a required $C_D A$ for the flaps follows. This depends on the flap area and on the flap inclination angle. Using this $C_D A$ then forms the basis for computing the resulting control moment corresponding to the aforementioned inclination angle.

An advantage of flaps is the possibility of having a low control system mass. This is possible because of the option to mechanically lock each flap in a certain orientation. This would not require constant power, as the control forces would be produced by the aerodynamic forces exerted on the flaps.

This advantage poses a major disadvantage at the same time: No control force actuation is possible outside of the Martian atmosphere. Each time the spacecraft is not flying through the atmosphere and needs control actuation usage of the flaps is not possible. Thus thrusters would need to be used during these times, requiring additional mass.

A second disadvantage to using flaps comes from the option to lock the flap orientations. By doing this the mass can be kept low, but this also means a limited number of discrete flap settings would be available. This would make it hard to properly control the spacecraft by using these flaps, especially under the influence of disturbances.

A third complication of using flaps is the coupling between the force exerted by the flaps and the local structural deflection angle. The control force delivered by the flap causes the inflatable structure to deflect rearward, which causes the flap force to decrease. This in turn commences a decrease in structural deflection angle which will again increase the force exerted by the flaps. One can see from this that using flaps on the inflatable structure would induce oscillations in the spacecraft. The effects of these vibrations on the stability and controllability of the CIA are unknown at this point in the design process.

Lastly, using body flaps on a non-winged entry vehicle has not yet been proven in flight. This poses a performance risk during concept development. This is in sharp contrast with the option of using thrusters, which features high reliability. Thrusters have been used extensively and are the go-to option for ADCS' and as main propulsion system.

6.1.4 Thermal analysis

This section discusses the method used to perform the thermal analysis of the TPS. First the required inputs and outputs are explained, then the analysis method is briefly described. The limitations of the model and concluding remarks will conclude this section.

Inputs and outputs To perform the thermal analysis a given lay-up that consists of different materials with variable thicknesses is needed. From the aerodynamic analysis and the wall temperature (T_w) a heat flux ($\dot{q}_s$) is found. The chosen trajectory determines the atmospheric temperature (T_{atm}). Using the given lay-up, the heat flux and atmospheric trajectory as input in the upcoming analysis method, the temperature distribution over time throughout the lay-up is found. This distribution also consists of the wall temperature (T_w), which is used to determine the heat flux. Thus, herein a small iteration takes place. After the temperature distribution is obtained it is used to check whether a given lay-up will properly function in the chosen trajectory.

Assumptions Here the assumptions are stated that are used to simplify the problem.

- The aerodynamic analysis has shown that the highest heat flux is found in the stagnation point at the wall. Therefore this is the main point of interest, for which the whole TPS is sized.
- The sizing can be done in one point with a 1D lay-up since the 1D analysis is very comparable to the 3D analysis at the centre of the heat shield according to Del Corso et al. [1].
- It is assumed the materials used have properties that remain constant as the temperature changes.
- The heat equation used to model the problem can be discretised. The Crank-Nicolson scheme is used as discretisation scheme, which has as advantage that it is unconditionally stable. A disadvantage is that it is more computationally expensive than simpler schemes.
- Contact resistance between the layers can be modelled as a thin layer of air with varying thermal conductivity.
- The incoming heat flux consists only of aerodynamic heating. Influences such as the solar flux, Mars' albedo and Mars' infra-red radiation are considered negligible with respect to the aerodynamic heating.

Analysis method The thermal problem is modelled as shown in Figure 6.1. Smith et al. have modelled this problem in approximately the same way and are therefore used as reference for the model to be developed [4]. The tool starts with a given lay-up consisting of thermal protection, insulation and structural layers. The heat transfer is modelled by an incoming heat flux due to the convective aerodynamic heating at the surface and an outgoing radiation at the front and back surfaces. Between the front and back surface the different layers are separated by a layer with varying conductivity that models the contact resistance. Within each layer heat is transferred by conduction.

Since a 1D thermal model is used to analyse the problem Equation 8, also known as the 1D heat equation, can be used to relate temperature, space and time using the thermal diffusivity (α_d). The thermal diffusivity is a function of the thermal conductivity (k), density (ρ) and specific heat capacity (c_p) as shown in Equation 9 [37]. A Crank-Nicolson scheme is used to implement the heat equation. This will model the heat conduction within each layer. The convective heating is obtained from the aerodynamic analysis and the radiation is calculated using Equation 10 [37]. It is assumed that the temperature

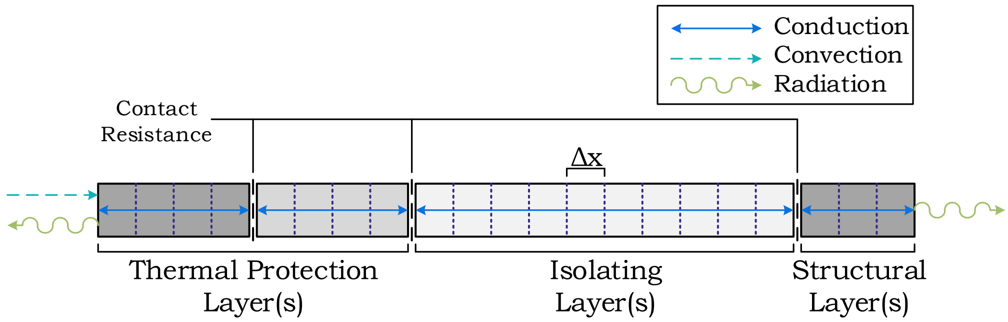

Figure 6.1: 1D thermal model

(T_∞) of the gas into which the heat shield radiation is directed, is equal to the atmospheric temperature of Mars.

$$\frac{\partial T}{\partial t} = \alpha_d \frac{\partial^2 T}{\partial x^2} \quad (8) \qquad \alpha_d = \frac{k}{\rho c_p} \quad (9) \qquad \dot{q}_r = \varepsilon \sigma \left(T_w^4 - T_\infty^4\right) \quad (10)$$

Limitations Simplifying the problem introduces some limitations to the design tool. One of the drawbacks of a 1D analysis is that the complete TPS is sized according to the conditions at the stagnation point. Furthermore it does not account for cross-planar heat flow. These drawbacks will decrease the estimated heat through the lay-up and therefore the current analysis method provides a conservative estimate for the TPS.

The influence of the assumption that material properties do not vary with temperature on the required thicknesses of different lay-ups is small. Note that this will not lead to a more conservative design as the thermal resistance decreases as temperature increases.

The paper by Del Corso et al. states that it is difficult to analytically determine the contact resistance [1]. Del Corso et al. used their own data for this, though arbitrary multiplication factors had to be applied to match their model with the validation data. Also analytically calculating the contact resistance introduces more unknowns that have to be determined. Therefore varying conductivities have been empirically assigned to the thin layers of air between the layers. A disadvantage is that multiple layers had to be tested to find correct conductivities such that the developed tool matches experimental data. The experimental data found in the papers by Del Corso et al. is used for the validation of the thermal model [1, 2]. The thermal model was successfully verified and validated as shown extensively in Appendix A.3.

6.1.5 Structural analysis

Structural assessment of the inflatable configuration has been performed by an estimation of internal forces. This is an essential step in the design of the CIA, since it:

- Allows to identify whether loads allow for concept structural design within state-of-the-art material capabilities
- Yields the loads at the structural interface between the CIA and the rigid centre body

- Gives an impression of the effect of changing design parameters on concept structural performance
- Gives insight in the structural behaviour and interaction of the inflatable

Forces are estimated for an inflatable structure that is aerodynamically loaded, as follows from vehicle trajectory analysis in its deployed condition. An interface with the aerodynamic analysis yields the optimised aeroshell shape as a baseline for the structural model used.

Moreover, it is essential that mass contributions of centre body, inflatable structure and connections are estimated in order to verify that decelerator mass is below the 1000 [kg] limit imposed as discussed in Section 2.4. Moreover, the parametric mass model for the inflatable structure allows for the identification of design measures to minimise the structural mass of the decelerator.

Force estimation method To meet the purposes of structural assessment of the inflatable configuration, force estimation is performed by a 2D truss analysis on a simplified geometry. This geometry relies on the aerodynamic aeroshell shape as its outer shape. This shape is defined by a number of toroids N, held together by radial straps, running along the surface of the inflatable.

Adjoining toroids are connected at three locations: By radial straps along the forward and aft side of the CIA (the former impinged on by the flow) and at their direct contact surface. In reality, as in the stacked toroid configuration used for NASA's IRVE [38], the contact surface of adjoining toroids is a straight wall, while top and bottom surfaces are of circular shape. This shape is the result of the internally applied pressure: equal but oppositely directed pressures cause a straight interface between toroids, causing the toroids to adapt to the unbalanced pressure in top and bottom surfaces through energy minimisation by taking on a circular shape.

Simplification was performed to realise a structurally determinate problem. This was done by modelling toroids as diamonds. The orientation of the diamonds is defined by the half-cone angle θ, allowed to vary over its radius and circumference per toroid, and their shape by a fixed width w and varying height h, to allow for a tapered structure. Nodes are designated as the corners of each diamond and connecting members have been numbered. The numbering convention and dimensions are illustrated in Figure 6.2.

Force estimation is performed in a 2D plane representing a cross-sectional slice of the CIA. Each toroid is loaded externally by an aerodynamic force applied perpendicular to its width w at its forward node. The aerodynamic force is the resultant of the aerodynamic pressure q, assumed to be constant for each toroid, multiplied by the toroid width w to represent its working area.

By requiring a force equilibrium in two orthogonal directions within the plane, the internal forces in each of the members 1 to 6 (as defined in Figure 6.2b) are determined for the N toroids. This system of equations is solved from the free end (outboard) to the pinned end (inboard) where the inflatable is connected to the centre body. The resultant reaction forces are determined for the two attachment points between the centre body and inflatable structure, forward and aft.

As the input forces are in Newtons per meter, being the product of a pressure over a length, forces should technically be designated as forces per unit length or running loads.

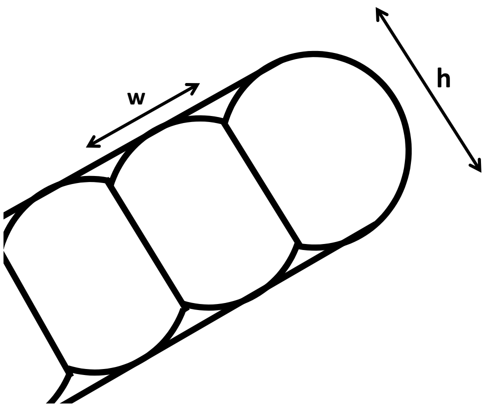

(a) Actual toroid layout

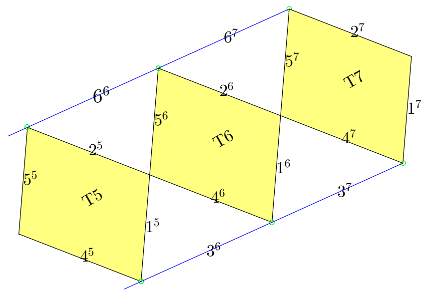

(b) Simplified truss model

Figure 6.2: Comparison between the actual and simplified inflatable model

Hereafter, all references to forces in this section are in fact references to running loads. To calculate forces from running loads, these are multiplied with the local circumference since running loads act over the circumference.

The decreasing circumference over which the forces act going from outboard to inboard in each 2D slice, inherent to the sphere cone design, results in an increase in running loads. This increase is proportional to the decrease in diameter via the circumference. Thereby the member running loads are scaled by the ratio of the radial distances with respect to the centre body longitudinal axis. Force transfer namely requires tip and root forces to be equal, where forces are the product of running load and circumference.

3D effects are partially taken into account by assuming that all lateral loads are carried circumferentially rather than in the considered 2D plane. Therefore lateral loads are set to zero at each of the outer (forward and aft) truss nodes. In reality this will, to a large extent, be true as the circular and stacked structure will be the primary contributor to bending stiffness. These lateral loads are primarily those induced by bending moments, such that neglecting them in the 2D plane implies that the bending moment is taken up by the 3D structure.

Validation is performed on the basis of FEM results presented by Lindell et al. [38]. The modified 2D method yields acceptable results for force estimations on IRVE-II with a maximum error of 15.4%, rather than the severe errors induced by not taking into account the 3D bending stiffness. The full verification and validation results can be found in Appendix A.4.

The minimum internal pressure required to prevent wrinkling is approximated by Equation 11 [39, 40], based on the premise that the work done by the aerodynamic force F_{aero} is counteracted by the internal inflation pressure. In this approximation θ denotes the mean half-cone angle.

$$p_{infl_{,min}} = F_{aero} \frac{4}{3\pi} \frac{tan(\theta) sin(\theta)}{D_o h} \tag{11}$$

This pressure induces a tensile running load f_{infl} in the members of magnitude [41]:

$$f_{infl} = \frac{p_{infl_{,min}} w}{2} \tag{12}$$

Dimension w is used rather than h as it is the smaller of the two dimensions. Hence this results in an overestimation of the inflation pressure. As the pressure calculated by Equation 11 is an approximate minimum inflation pressure for a general stacked toroid case, it is used as an initial guess. The inflation pressure is iteratively increased from this value to produce tension in all flexible material.

The inputs and outputs of the structural model are tabulated in Table 6.1.

Table 6.1: Inflatable structural analysis tool in- and output

Input	**Output**
Toroid inclination	Internal forces
Number of toroids	Reaction forces
Toroid dimensions	Inflation pressure
Aerodynamic loading	
Centre body and deployed diameter	

The approach is based on the following assumptions:

- Small deformations. In reality the deformations can be significant, changing the orientation and magnitude of the forces in the structure.
- 3D effects are partially taken into account by setting the lateral loads to zero. See the previous discussion.
- Constant dynamic pressure. A constant dynamic pressure is not in line with the actual loading. Based on the discussion in Appendix A.4 the errors introduced by this are deemed acceptable.
- The aerodynamic loading is applied discretely at the outer nodes. The effects of a continuous distribution are neglected since they do not fit within the truss model. This assumption neglects a bending load within the forward radial strap.
- Structural mass is neglected. Neglecting the structural mass causes a small error within the computed loads, varying with the ratio of structural mass and dynamic pressure.

The consequence of these assumptions and their impact, primarily the first two, make the model suitable for a preliminary load analysis of the inflatable structure and the loads at its attachment points, but unsuitable for detailed analysis and structural design & sizing.

Inflatable mass estimation method Mass estimation for the inflatable structure is performed on the basis of a parametric mass model [40]. The mass model is based on a number of stress equations and cone deformation to compute the outputs listed in Table 6.2. Moreover, the model calculates inflation gas pressure based on the premise that work done by inflation gas and aerodynamic pressure should be equal and members are in tension, in line with relations established by Brown [39]. The model is based on the assumption that the inflatable is an axisymmetric sphere cone of constant half-cone angle, thereby treating a simplified model of the shape determined by the aerodynamic optimisation.

Primary assumptions in this model are a symmetric sphere cone and a constant half-cone angle. Verification and validation efforts have been summarised in Appendix A.4 and have yielded the conclusion that the mass model is suitable for preliminary design.

Table 6.2: Inflatable mass analysis tool in- and output

Input	Output
Toroid inclination	Flexible material mass
Centre body and deployed diameter	Inflation gas mass
Number of toroids	Inflation system mass
Inflation gas properties	
Aerodynamic loading	
Material properties	

6.2 Design parameter sensitivity

The following sections present an overview of design characteristics as obtained by the analysis and design tools presented in this chapter. Sensitivity analysis is limited to those parameters of key importance for the aerocapture and entry phase.

6.2.1 Trajectory sensitivity

Effect of radius For five different radii the maximum dynamic pressure and minimum height above Mars that were encountered on the first pass through the atmosphere were recorded. This is shown in Figure 6.3. For each radius a trajectory for which the spacecraft just reaches the escape velocity (dark blue line, slow trajectory) and a trajectory which decelerates as fast as possible while staying under $3g_e$ deceleration (light blue line, fast trajectory) are calculated. These two trajectories represent the two boundaries of what could possibly become the final trajectory. To achieve the different trajectories the control (constant angle of attack and changing bank angle) has been adapted. In Figure 6.3 it can be seen that there is an approximately quadratic relationship between dynamic pressure and diameter for both limit trajectories. It can also be seen that the fast trajectory has a higher dynamic pressure over the entire range of diameters. This is because the fast trajectory decelerates faster and goes deeper through the atmosphere. The minimal height achieved in the first pass is always 15 $[km]$ for the fast trajectory because in this trajectory the aerocapture and entry phase is terminated at 15 $[km]$ height within the first pass. For the slow trajectory it can be seen that a deeper pass through the atmosphere is needed with a lower diameter aeroshell. The same relation is true for the fast trajectory even though this cannot be seen in this figure. The maximum Mach number encountered is a constant value of Mach 41.7 for changing diameter and also for both limit trajectories.

Apart from this results it should be noted that there is a lower limit to the diameter of the CIA imposed by the side heat flux into the capsule. For a large diameter the capsule is in the wake of the CIA and the side heat flux can thus be neglected. For a smaller diameter aeroshell eventually a backshell will be needed to protect the capsule. This will induce an unacceptable amount of mass.

Effect of lift-to-drag ratio During the aerocapture a high lift allows the spacecraft to pass higher through the atmosphere while still having control over the vehicle, thus having the ability to stay in the atmosphere longer. The drag should also be high during the aerocapture in order to have the ability to lose enough energy.

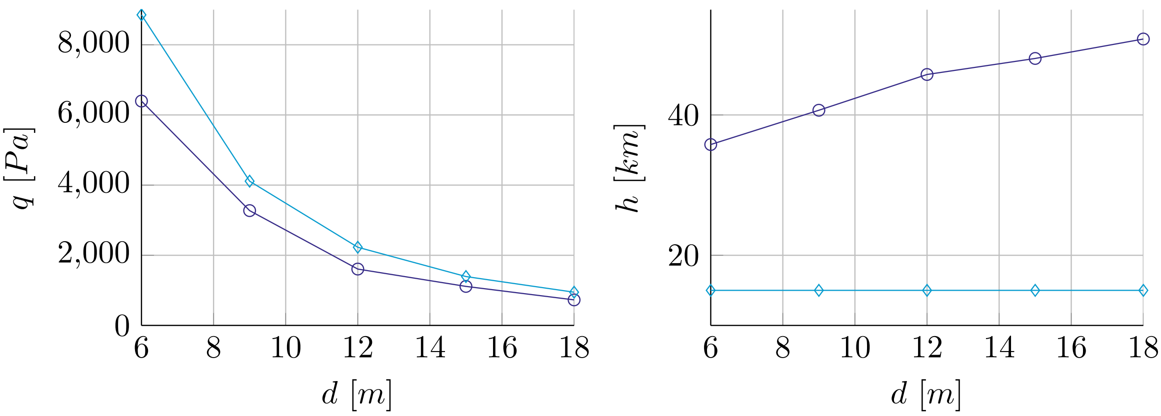

Figure 6.3: Maximum dynamic pressure and Mach number and minimum height for different radii

During the entry & descent phase a high lift gives better control over the final landing position. The deceleration during this phase is however quickly too high, so a lower drag is required.

As the aerocapture and entry & descent phases both have to deal with the same aerodynamic properties a compromise has to be made on the drag, however the lift should be high for both phases.

Entry corridor The entry corridor is the fictional box where the entry vehicle should pass through to go into orbit. Too low and the acceleration limit or the heat limit is breached, too high and the entry vehicle will skip on the atmosphere and never return. This corridor is dependent on different design parameters, the most important are the aerodynamic coefficients, entry velocity and control system.

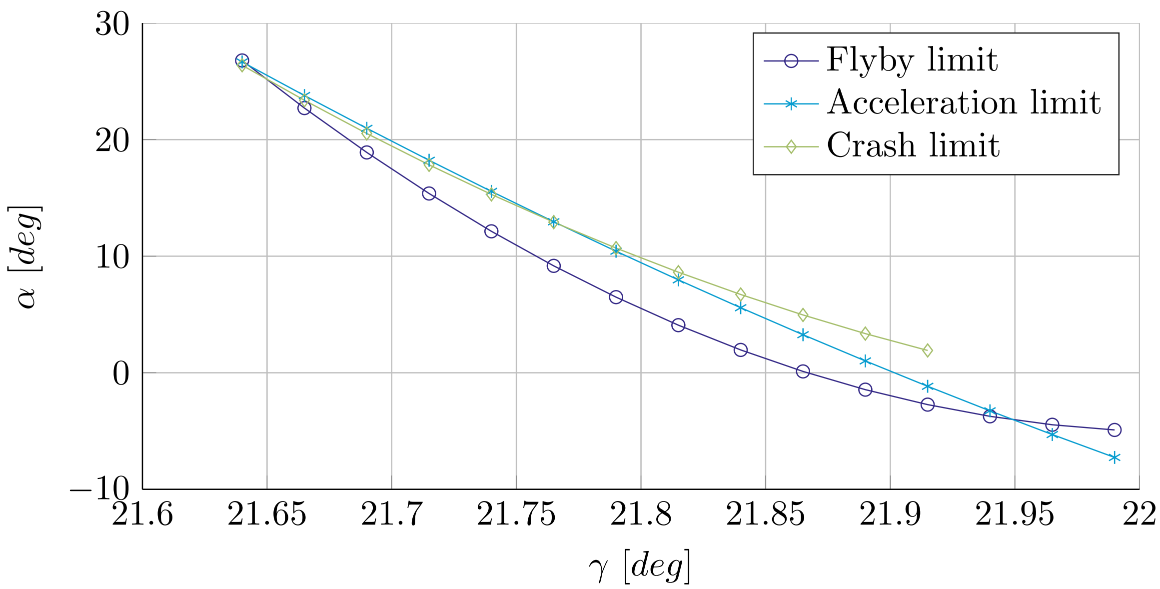

Figure 6.4: The entry corridor for different angles of attack and flight path angles. This figure is computed with the final aerodynamic shape, the aerocapture μ-profile, and an entry velocity (V) of 7000 $[m \cdot s^{-1}]$

From a point in the middle of the entry corridor, as shown in Figure 6.4, the initial flight path angle (γ), the angle of attack (α) and the bank angle (μ) have been changed to the utmost points where an orbit was still achieved. The effects of these changes separately are presented below.

Effect of initial flight path angle As can be seen in Figure 6.5 the range of initial flight path angle for which an orbit is achieved is very limited. This means γ has a big effect on the trajectory. For this small change in flight path angle the maximum dynamic pressure (q) increases by approximately 400 $[Pa]$. It can also be seen the minimum height (h) decreases by more than two kilometres. The maximum Mach number (M) does not change for changing initial flight path angle.

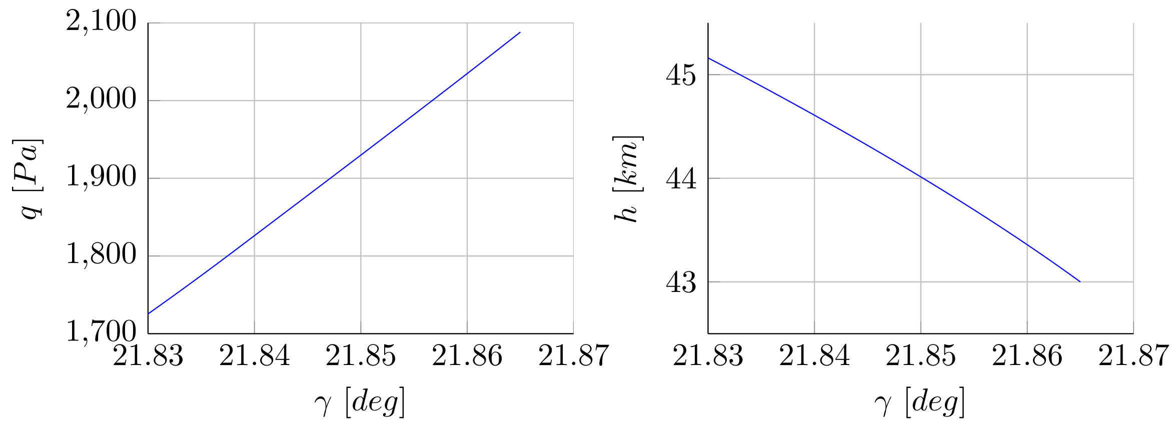

Figure 6.5: Effect on dynamic pressure, height and Mach number of different flight path angles at $\alpha = 15$ $[deg]$ and $\mu = 30$ $[deg]$

Effect of angle of attack In Figure 6.6 the range of angle of attack for which an orbit is achieved is shown. It can be observed that this window is five degrees wide. This means that the effect of α on the trajectory is significantly smaller than the effect of the flight path angle. However for this bigger change in angle still a big change both dynamic pressure and height is encountered. The maximum dynamic pressure increases by approximately 300 $[Pa]$. It can also be seen the minimum height decreases by almost two kilometres. The maximum Mach number does not change for changing angle of attack.

Effect of bank angle As can be seen in Figure 6.7 the range for which an orbit is achieved changing only bank angle is almost 60 $[deg]$. This means μ has to be changed a lot, compared to γ and α, to have an effect on the orbit. This change in bank angle does not have a big effect on the maximum dynamic pressure and the height. This indicates that the change in trajectory caused by a change in bank angle is much more subtle. The maximum Mach number does not change for changing bank angle.

6.2.2 Aerodynamic sensitivity

Important parameters The following parameters were determined to have a significant influence on te performance of the vehicle:

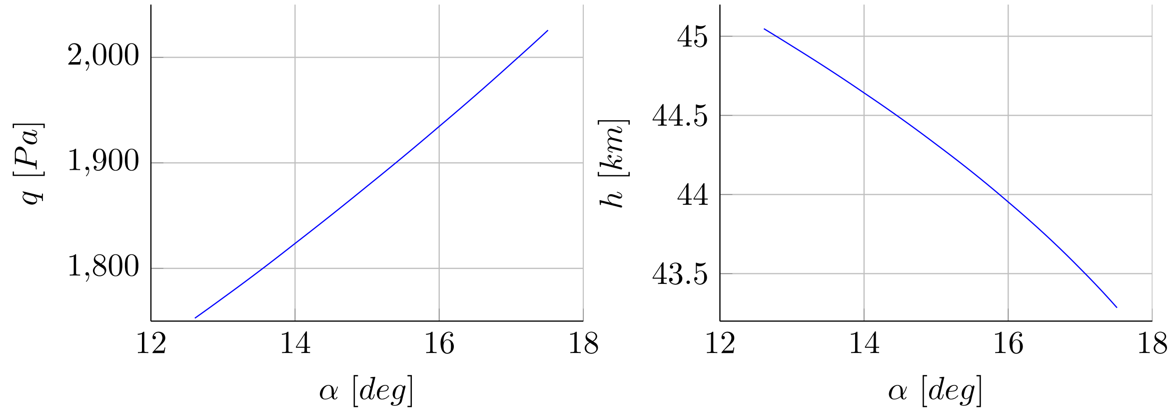

Figure 6.6: Effect on dynamic pressure, height and Mach number of different angles of attack at $\gamma = 21.845$ $[deg]$ and $\mu = 30$ $[deg]$

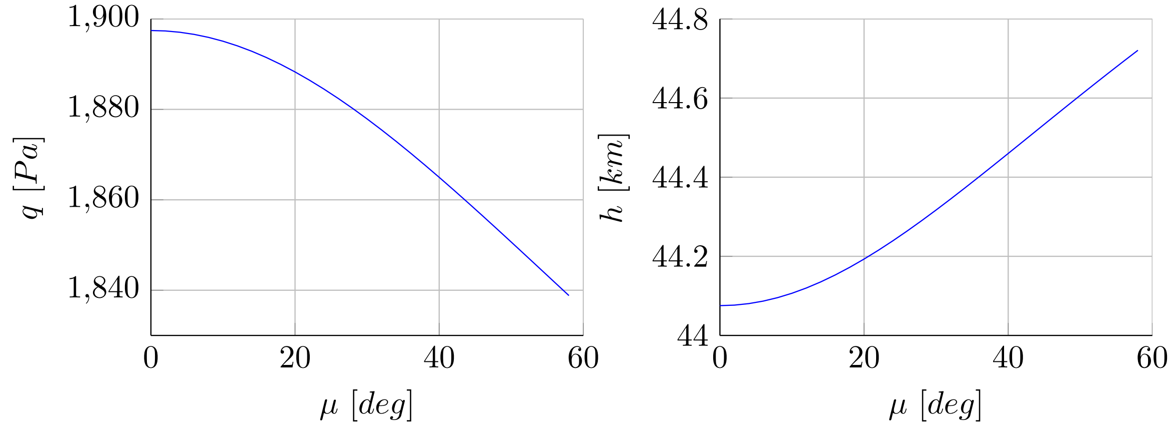

Figure 6.7: Effect on dynamic pressure, height and Mach number of different bank angles at $\alpha = 15$ $[deg]$ and $\gamma = 21.845$ $[deg]$

- Lift. As detailed in Section 6.2.1, the vehicle requires a lift vector to provide flight path control. A larger lift vector provides an increase in flight path control.
- Drag. The vehicle decelerates purely on atmospheric drag. An increase in drag will decrease the required time for aerocapture and entry and provides greater flexibility in terms of the path through the atmosphere.
- Lift-to-drag ratio. The lift-to-drag ratio is an indication of the freedom in the selection of the trajectory. A higher lift-to-drag ratio will provide greater flexibility.
- C_{M_α}. The derivative with respect to angle of attack of the moment coefficient is a measure of the stability of the vehicle.
- CG-offset. The CG-offset at a given angle of attack required to cancel the moment generated by the vehicle at that angle of attack. It is a measure of the control effort required to trim the vehicle.
- Heat flux. For a given flight condition, the heat flux in the stagnation point depends only on the vehicle geometry.

Shape sensitivity Obtaining favourable characteristics of the aerodynamic shapes requires understanding of the influence of shape parameters on the performance of the design. To this end, firstly an analytical approach is taken. After that, conclusions can be made about different aerodynamic shapes. The optimisation tool is used afterwards to generate shapes that are optimised for certain design parameters, such that the conclusions based on the analytical knowledge can be verified.

In Figure 6.8, the lift and drag performance as well as the lift-to-drag ratio of a flat plate in a free stream is given. Since Newtonian flow theory is based on the assumption that pressure only depends on the local body incidence angle, this plot can be used to deduce performance of a given shape. As can be seen in the plot, a vehicle with a high drag has most of its surface perpendicular of the flow.

Lift A high lift is achieved by having large parts of the shape under an incidence angle of $35\,[deg]$. An axisymmetric shape does not create lift at zero angle of attack, since every radial part of the shape cancels all non-drag forces out. Skewness of the shape, such as portrayed in Figure 6.9a, can be used to create lift at zero angle of attack: a larger part of the surface is inclined upwards than downwards, meaning the skewed shape generates a downward lift. Using skewness instead of an axisymmetric body at a high angle of attack may help to prevent the shock wave from hitting the payload module.

Drag Maximum drag is created by having large parts of the shape perpendicular to the flow. This follows directly from Figure 6.8, in which it can be observed that maximum drag is generated at an incidence angle of $0\,[deg]$

Lift-to-drag ratio A high lift-to-drag ratio is achieved by having the highest angle of attack for every part of the spacecraft. This entails having a flat plate at the maximum angle of attack for maximum lift-to-drag ratio. If a non-flat body is chosen, large parts of the area should be nearly under a high inclination, which can be realised by having a very long body at a small angle of attack.

Static stability The aerodynamic shape required for static stability can be argued based on the local inclination angle. The pressure force always acts normal to the surface. A large moment arm can be created by inclining the outer edges of the CIA. At a positive angle of attack, the lower edge of the CIA is turned more perpendicular to the flow such that its pressure force is increased. An example of a shape that features this is given in Figure 6.9a. Depending on the location of the CG, at an angle of attack the lower part pressure is increased while the pressure on the upper part is decreased, generating a moment. This means that for an increase in angle of attack, the restoring moment is also increased.

Centre of Gravity shift In order to trim the CIA at a certain angle of attack, a CG-offset is used: the CG does not lie directly on the most forward point of the spacecraft. In order to minimise the impact, the required CG-offset is calculated using Equation 13. A large offset may be unrealistic and more difficult to implement.

$$Z_{CG} = \frac{C_M l}{C_L} \tag{13}$$

In general the relation between required CG-offset for a certain lift-to-drag ratio is a good indicator for the performance of a design, since this relates the performance to the cost of the performance.

Finally, the heat flux is given in Equation 3 and is directly dependent on the density and velocity as well as the local radius of curvature. A less curved body in the stagnation point thus leads to a lower heat flux.

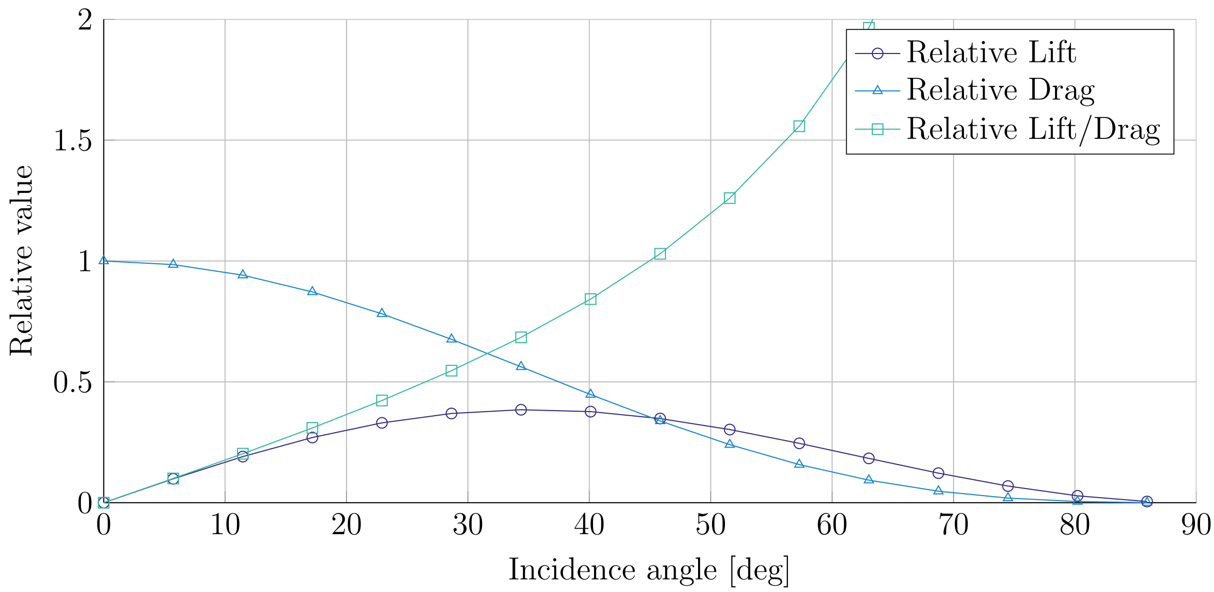

Figure 6.8: Lift, drag and lift-to-drag ratio for a flat plate versus incidence angle

To illustrate the characteristics of different aerodynamic shapes, an optimisation has been performed towards certain aerodynamic coefficients, as explained in Section 6.1.2. These shapes serve to enlarge understanding of how certain shape aspects correspond to certain aerodynamic properties. For the following parameters has been optimised:

- Drag coefficient C_D: The maximum drag should be attained by a flat plate at a zero angle of attack. This is also the result of the optimisation towards a maximal drag.
- Lift coefficient C_L: As per the analysis in this Section, the maximum lift coefficient is achieved by a flat plate at an angle of attack of 35 $[deg]$. This is confirmed by the optimisation algorithm, which produces the same flat plate as for maximum drag, but at an angle of attack.
- Lift over Drag $L \cdot D^{-1}$: The maximum lift-to-drag ratio is found for a flat plate at an angle of attack as high as possible. This result was achieved at an angle of attack of 40 $[deg]$, which is limited to keep the design in the range where the shockwaves do not hit the payload module.
- Static stability C_{M_α}: For this parameter, it is necessary to have large parts of the aerodynamic shape inclined with respect to the flow. The optimisation confirms this and creates a shape as portrayed in Figure 6.9b. This optimisation was constrained by a maximum length.
- CG shift $C_M \cdot {C_X}^{-1}$: The minimum CG shift for a given angle of attack is achieved by a flat plate since it generates very little moment. However, if static stability is required, the contours of the CIA can be inclined inwards.

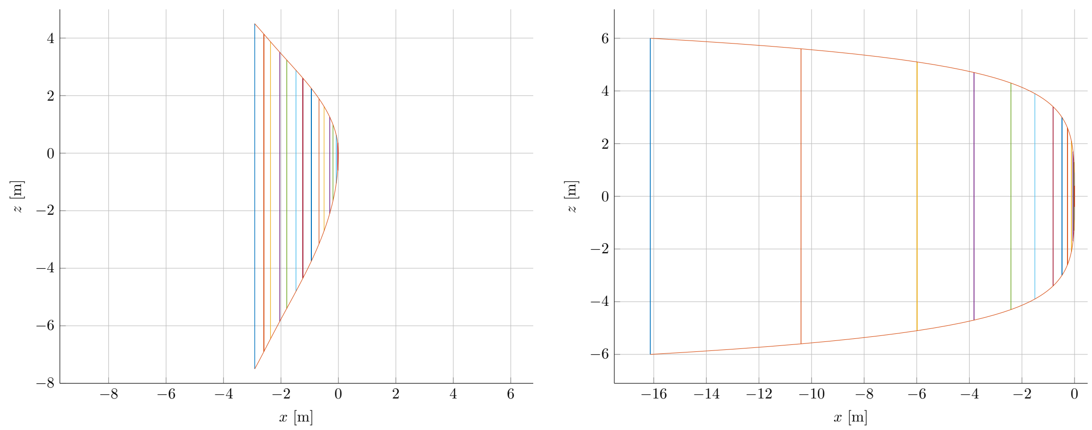

(a) Side-view of a skewed aerodynamic shape. The lower part generates a moment around the frontal part of the CIA when under an angle of attack

(b) Optimised shape resulting in high static stability

Figure 6.9: Skewed and statically stable aerodynamic shapes

Various shapes Several large groups of varying shapes can be identified. The relative performance of each group can be qualitatively assessed by looking at the variations of the shape with respect to the optimal shapes for the various parameters. The effect of asymmetric cross-sections will be ignored in this assessment, and will be investigated separately. In Figure 6.10 representative cross-sections of the groups can be seen. Group A represents simple concave surfaces. Group B has a concave centre section with a flat ring around it. Group C has an approximately flat central section, with steep edges around the outer radius. Group D represents the half cone shapes, with relatively straight sides and a blunt nose.

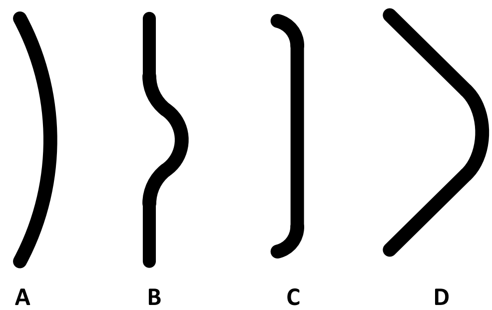

Figure 6.10: Various schematic aerodynamic configurations

As was discussed in this section, a flat plate will generate the most lift and the most drag, albeit at different angles of incidence. Since Group C closely mimics a flat plate in the majority of its cross-section, it will have the best lift and drag performance. Group B also has a significant flat section and will therefore also have good performance in terms of lift and drag. Groups A and D will both have significant portions of their cross-sections at sub-optimal incidence angles for maximum lift or drag, and will therefore have lower lift and drag performance.

The C_{M_α} of a given shape is a measure of stability. Shapes which require large moments to change the angle of attack have a higher stability. As can be seen in Figure 6.8, surfaces at incidence angles of 40 to 60 $[deg]$ provide large changes in force for small changes in angle of incidence. Sections at these incidence angles will therefore stabilise the vehicle, since a change in angle of attack will cause one side of cross-section to generate a greater moment than the other. This is visualised in Figure 6.11. Cross-sections B and C have parts of their cross-section at such angles. Since the sections in C are on the outside of the cross-section, it will be significantly more stable than type B due to the moment arm these parts have. A and D will have significant portions of their cross-sections contribute to the vehicle moment. Although these section are likely to be at sub optimal angles of incidence for high stability, the large area contributing to the stability of the vehicle will ensure that both types of cross-section are stable.

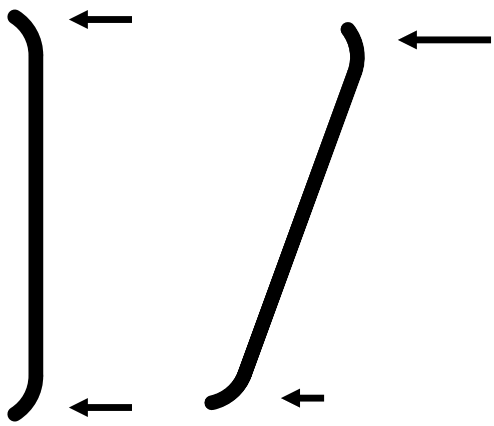

Figure 6.11: Stabilising effect of reduced incidence angle sections

Asymmetry An asymmetric body will ensure that even at zero degrees angle of attack, the vehicle generates lift. As explained in Section 6.2.1, this allows for greater control of the vehicle during aerocapture and entry and is therefore desirable. The angle of attack that can be attained is limited by the crew module extending into the flow around the body. Achieving a higher lift at a lower angle of attack is therefore desirable. If the shape is heavily offset to one edge of the body, the crew module will extend into the flow at very low angles of attack. Figure 6.12 shows the effect of asymmetry on the lift-to-drag ratio by transforming a given symmetric shape into an asymmetric shape. The asymmetric shapes are created by a linearly shifting the cross-sections of the body in the zy-plane along the y-axis, with no shift at $x = 0\,[m]$ and maximum shift at $x = x_{max}$.

6.2.3 Thermal sensitivity

To investigate the influence of lay-up materials, heat flux variations, vehicle diameter and the trajectory approach on the TPS a sensitivity analysis is performed. First materials are selected to form multiple lay-ups. The different lay-ups are then optimised for different loading conditions. First the influence of heat flux variations on areal density is investigated. Subsequently, variations in mass due to changing diameters are tested. Lastly, the lay-ups are tested for different trajectories, either with a direct trajectory or with a

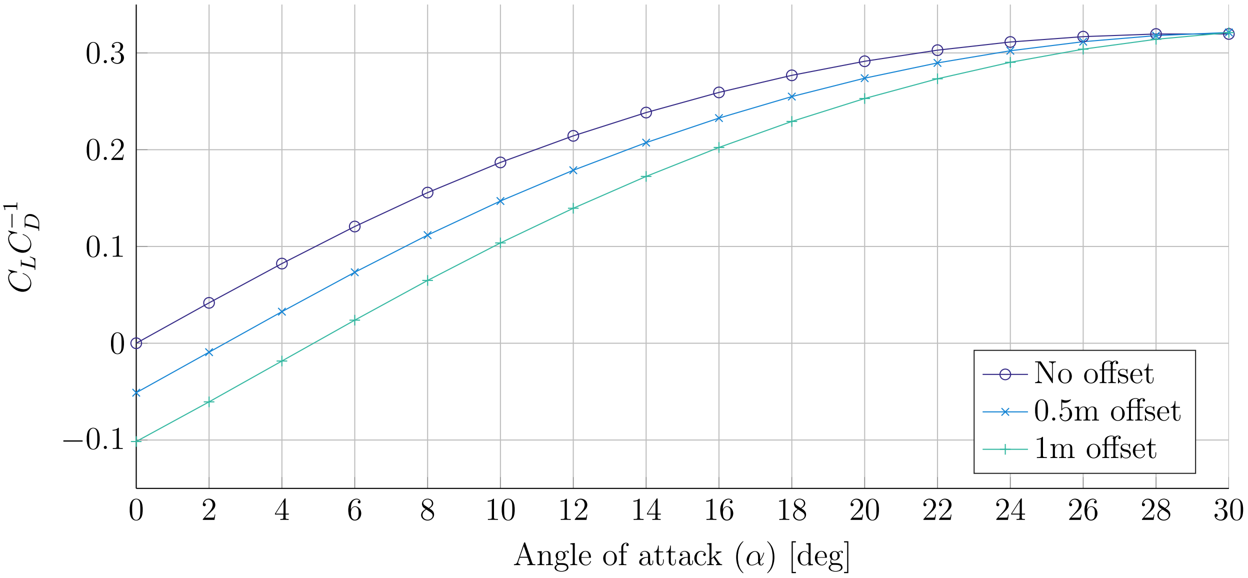

Figure 6.12: Effect of asymmetric shape on lift-to-drag ratio

parking orbit between aerocapture and landing. This investigation is done by using the tool described in Section 6.1.4 and successfully validated in Appendix A.3.

TPS materials Table 6.3 shows the materials that are used in the inflatable heat shield. A more extensive list of possible TPS materials and their properties can be found in Appendix B. These materials have been proposed during the design of multiple inflatable decelerator concepts, such as IRVE and Terrestrial HIAD Orbital Re-entry (THOR) [22]. For each material the thermal conductivity, the density, the specific heat, the maximum operative temperature and if applicable, the emissivity are given. The latter is only applicable to the upper thermal protection layers, because these layers, or heat barriers, will radiate heat into the surroundings.

A selection is made for the most promising thermal protection and insulation layers. These are Nextel BF-20 and Nicalon™ for the heat barrier layers. Nextel is a material already used by NASA in IRVE. Nicalon™ is a heavier alternative made up of continuous fibres of silicon carbide (SiC) that can withstand higher temperatures than Nextel up to 2073 $[K]$. Also the emissivity of Nicalon™ is much higher that Nextel, which allows for more radiation. For the insulation layers these are Pyrogel® 3350 and Pyrogel® 6650. With those materials three lay-ups are created such that a comparison can be made between the heat barriers and insulators. A schematic view of the layers is shown in Figure 6.13. Lay-ups 1 and 2 can be used to compare the performance of Pyrogel® 3350 and 6650. Lay-ups 2 and 3 serve as comparison for the Nextel BF-20 and Nicalon™. These lay-ups will be tested for different heat fluxes as well as different diameters.

Effect of heat flux In order to analyse areal density performance of lay-ups and changes due to varying atmospheric conditions a heat flux sensitivity is performed. To achieve this, ratios of the heat flux of a possible trajectory are used. The trajectory is found using a diameter of 12 $[m]$. The results are shown in Figure 6.14. The horizontal axis shows the heat flux ratio and the areal density is shown on the vertical axis.

Table 6.3: Flexible Thermal Protection System material properties [1–6]

Material	$\mathbf{k}\ \left[\frac{\mathbf{W}}{\mathbf{m \cdot K}}\right]$	$\rho\ \left[\frac{\mathbf{kg}}{\mathbf{m^3}}\right]$	$\mathbf{c_p}\ \left[\frac{\mathbf{J}}{\mathbf{kg \cdot K}}\right]$	$\mathbf{T_{max}}$ [K]	ε [−]	**Function**
Hi-Nicalon™	2.4	2900	1200	2073	0.93	rad. & barrier
Nextel BF20	0.146	1362	1130	1643	0.443	rad. & barrier
Pyrogel® 6650	0.030	110	1046	923	-	insulator
Pyrogel® 3350	0.0248	170	1046	1373	-	insulator
Kapton	0.12	1468	1022	673	-	gas barrier
Kevlar	0.04	1440	1420	443	-	structural
PBO Zylon®	20	1540	900	673	-	structural

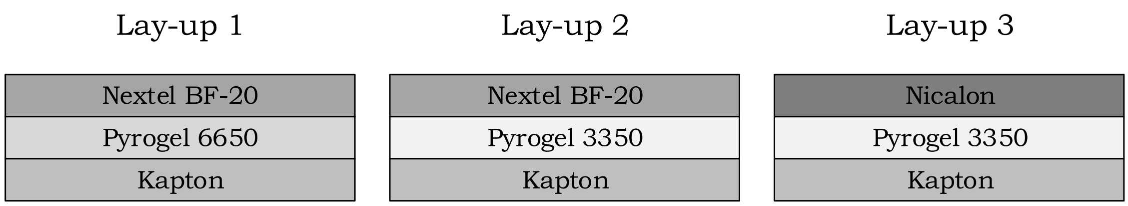

Figure 6.13: Tested lay-ups for the sensitivity analysis

As expected, the mass of the TPS increases with increased loading. Secondly and most important, the relative performance of the lay-ups can be observed. Lay-up 1 is clearly the lightest solution, followed by lay-up 3 and 2. Although lay-up 1 performs better in terms of its mass, the amount of loading it can bear is limited. If small changes in atmospheric properties occur during the EDL phase, for instance due to Martian storms, the TPS may succumb under the increasing loads. Therefore it is wise to choose Nicalon™ for further design. Lastly, if lay-up 1 and 3 are analysed relative to each other, it is clear that Pyrogel® 6650 performs much better than the 3350 variant. Therefore, for further design it is more favourable to use Pyrogel® 6650 as an insulator. The drawback of Pyrogel® 6650 is that it has a lower maximum use temperature. This is solved by using a good heat barrier such as Nicalon™.

Effect of diameter The three lay-ups are put to the test for different diameters. Aerodynamic analysis has provided heat fluxes for trajectories with corresponding diameters of 6, 9, 12, 15 and 18 $[m]$. As a side note, because the aerodynamic shape is different from the one in the previous paragraph, Figures 6.14 and 6.15 cannot be directly compared. An increase in heat flux caused an increase in the maximum temperature, surpassing the Nextel operative temperature limit which made it impossible for lay-ups 1 and 3 to fly trajectories at diameters of 12 $[m]$. Optimising the thickness of the lay-ups for these heat flux result in Figure 6.15. The solid lines indicate the nominal trajectory, with a parking orbit after aerocapture. For both graphs, the horizontal axis shows the relevant diameters. The plot on the left shows the areal density on the vertical axis and the right plot shows the total mass of the frontal TPS on this axis.

For increasing diameters, larger radii of curvature can be obtained, resulting in a direct decrease of incoming heat flux. Also, due to the increasing diameters which causes an

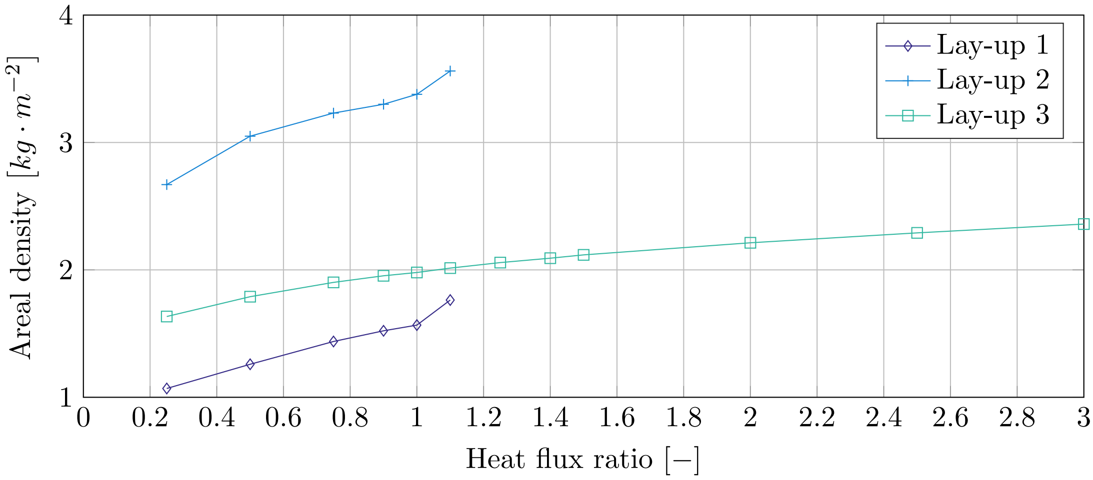

Figure 6.14: Heat flux sensitivity for the three selected lay-ups

increase in C_D and a reduction in ballistic coefficient, the vehicle can decelerate by the same amount at lower dynamic pressures. Therefore, the vehicle can stay higher in the atmosphere and fly in thinner air with the same velocity, decreasing heat development and incoming heat flux.

This effect can clearly be seen in the left figure, where the areal density decreases for increasing diameters. Obviously more material must be used to create larger TPS, which mostly results in a total mass increase for larger diameters. This can be seen in the right figure. The only exception is lay-up 2, the lay-up that is able to cope with the larger incoming heat flux at lower diameters. An optimum of its thermal performance is found at $9\,[m]$ where the frontal TPS mass reduces to approximately $150\,[kg]$. In addition, the relative mass performance of the different lay-ups is comparable to the performance in the previous paragraph.

Effect of time Whenever the vehicle is changing its descend rate, the total dissipated energy is still the same. However, the energy rate profile will have a different distribution over time, changing the temperature throughout the TPS. Steeper descends require a thicker heat barrier, limiting the heat flow to the rest of the shell, such that operational temperature of the insulator is not exceeded. A more gradual descend increases the time spend in the atmosphere and therefore increases the heat stored in the heat shield. This puts limits on the insulators minimum thickness, to block the heat flow to the structural layers and the rest of the vehicle. Therefore, the effect of descent time is analysed. The results are also shown in Figure 6.15. An alteration in time is visible by considering two types of viable trajectories, a direct trajectory and one with an orbit after aerocapture. From the figure it can be seen that the direct trajectory is the limiting one.

6.2.4 Structural sensitivity

Inflatable structural mass Based on the mass estimation model outlined in Section 6.1.5, the effect of changing design parameters on inflatable structural mass is investigated hereafter. To this end, the following design parameters have been investigated: centrebody

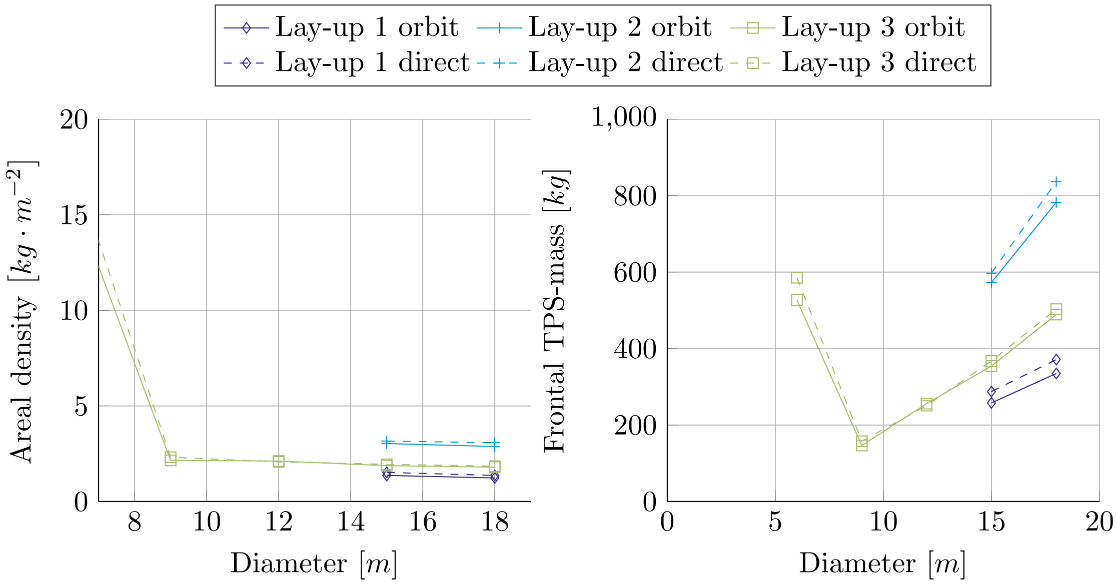

Figure 6.15: Areal sensitivity for the three selected lay-ups, both for a direct trajectory and a usual trajectory with a parking orbit after aerocapture. Left plot shows areal density, whereas the right plot shows the total mass.

and inflated diameter, half-cone angle, the number of toroids and aerodynamic loading. The drag coefficient has not been investigated separately, for it appears exclusively multiplied by dynamic pressure and a percentual increase in drag coefficient therefore has the same effect as an equal percentual change in dynamic pressure. The product of these two terms gives the aerodynamic force working over the decelerator frontal surface area.

Firstly, from Figure 6.16a it follows that mass decreases with an increasing centrebody diameter given a deployed diameter. This is due to the fact that an increasing centrebody diameter increases the areal contribution of the centrebody: the inflatable requires less structural mass by decreased aerodynamic loading thereof, as aerodynamic pressure works over an area. In turn, this suggests that the centrebody becomes heavier, which is not the case as the centrebody is typically sized for launch rather than (re-)entry loads [38]. It can therefore be concluded that maximising centrebody diameter is beneficial for structural mass.

Secondly, from Figure 6.16c it follows that increasing dynamic pressure effects an increase in structural mass of the inflatable. This is the result of an increased aerodynamic loading and therefore structural taxation of the inflatable. To withstand this loading, extra structural mass is required. Moreover, for a given peak dynamic pressure an increase in deployed diameter effects an increase in structural mass. Primary cause hereof is the fact that pressure works over a surface area and an increase in area thereby increases the loading. This is further amplified by an increase in bending moments by the larger distance from tip to root.

From Figure 6.16b it may be observed that the half-cone angle significantly affects inflatable structural mass: in general smaller half-cone angles are preferable. Increasing half-cone angle beyond an optimum region at approximately 45 $[deg]$ strongly increases structural mass; decreasing it below this region similarly increases structural mass, but less strongly. Moreover, as aerodynamic loading is increased the optimum region shifts and smaller half-cone angles are preferable. This is due to the fact that decreasing the

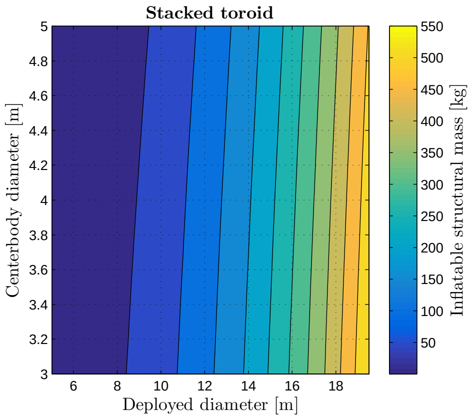

(a) Mass versus centrebody and deployed diameter

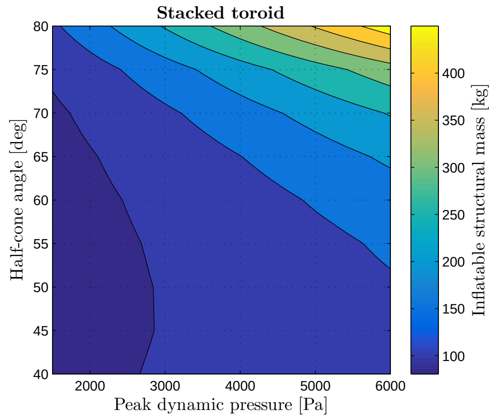

(b) Mass versus half-cone angle and peak dynamic pressure

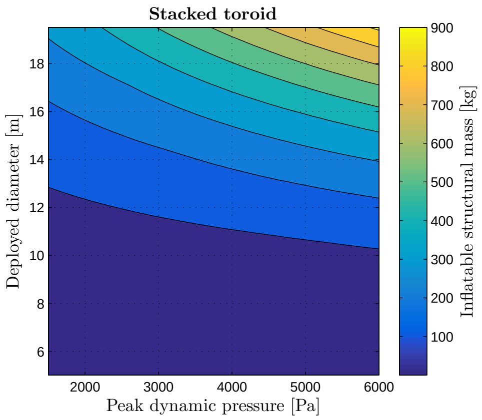

(c) Mass versus deployed diameter and peak dynamic pressure

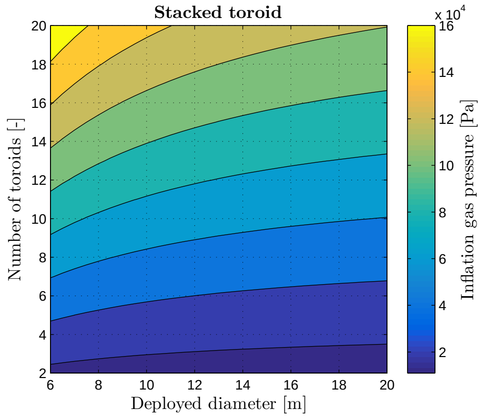

(d) Inflation pressure versus number of toroids and deployed diameter

Figure 6.16: Inflatable structural mass and inflation pressure as a function of design parameters

half-cone angle increases bending stiffness by an increased moment of inertia in the bending plane. This increased bending stiffness is further amplified by the 3D characteristic of the sphere cone and carries over to more effective use of material in bending, requiring less mass to resist the bending moment by aerodynamic loading. For a given deployed diameter, however, decreasing the half-cone angle increases the effective inflatable length. This addition of material is to be traded off against the increased bending material. At low dynamic pressures, increased bending stiffness is less warranted than at higher pressures, at which bending loads increase and bending stiffness is increasingly more warranted.

In Figure 6.16d inflation gas pressure is observed to increase for an increasing number of toroids and to decrease with an increasing deployed diameter. Both an increase in the number of toroids and a decrease in deployed diameter decrease toroid radii, effecting an increase in the working area of the inflation pressure. Due to the proportionality of the running load induced by inflation pressure via Equation 11 with toroid radius, a larger inflation pressure is required to induce the same running load with a smaller radius. This running load is based on the consideration that the work done by inflation gas and external forces in axial direction are equal [39], independent of the number of toroids. It is similarly independent of the deployed diameter, since both inflation and aerodynamic pressure have the same working area in axial direction. The number of toroids was observed to have no significant effect on structural mass beyond ten toroids, after which mass reductions were found to be within two percent. An increase in the number of toroids from two to ten yields significant mass advantages of up to ten percent.

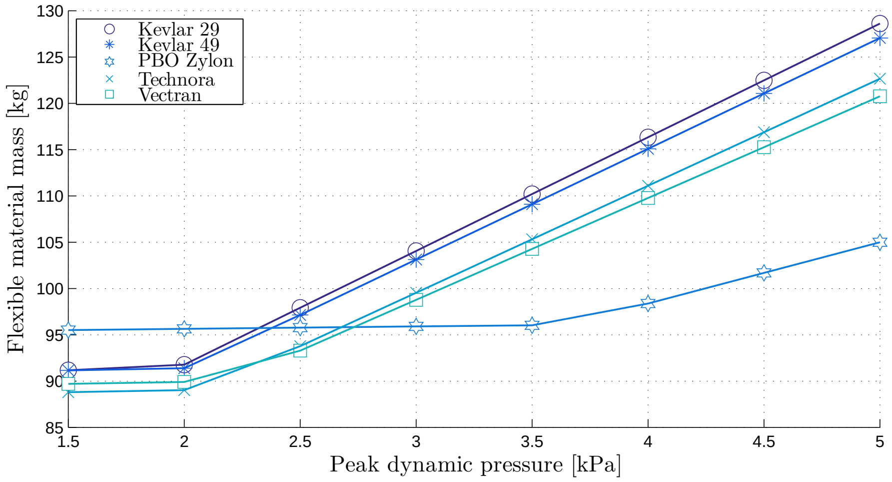

Figure 6.17: Flexible material structural mass estimation for different materials

Material selection has a significant effect on flexible material mass, as illustrated by Figure 6.17. It can be observed that, for peak dynamic pressures below $2\,[kPa]$, minimum gauge thickness is leading for all selected fibres. Below this pressure, density is the leading parameter and a less dense material will perform better. Due to the significantly lower density of Spectra 2000, $970\,[kg \cdot m^{-3}]$, versus that of for example PBO Zylon®, $1540\,[kg \cdot m^{-3}]$, Spectra 2000 offers mass advantages at low dynamic pressures. Therefore it can be concluded that for low dynamic pressures materials should be selected based on minimum gauge thickness, but thickness rapidly increases as loading is increased and the minimum gauge thickness is exceeded. For PBO Zylon®, this occurs at a relatively high peak dynamic pressure of $3.5\,[kPa]$.

For higher dynamic pressures, materials with a higher specific strength perform better in terms of structural mass. Flexible material is fully loaded in tension by the inflation pressure is required not to fail under tension, dictated by ultimate strength. To this end, a certain thickness with a corresponding mass is required. Mass performance is then directly linked to specific strength and this is confirmed by Figure 6.17. Aramid fibres Kevlar and Technora have the lowest specific strengths, approximately $2\,[MN \cdot m \cdot kg^{-1}]$. A notably higher specific strength of 3.44 and $3.77\,[MN \cdot m \cdot kg^{-1}]$ is attained by Spectra 2000 and PBO Zylon® respectively. This confirms the choice for PBO Zylon® for its mass advantages over Kevlar in IRVE-3 [42]. Spectra 2000 is capable of achieving a lower mass than PBO Zylon® despite its lower specific strength, due to its low density.

All materials have been selected based on their operating temperature since these are required to operate in an environment with significant thermal loading. As an example, Spectra 2000 fibres are not deemed suitable for their allowable temperature of $150\,[°C]$, which would incur significant extra TPS mass. Dyneema would similarly be unsuitable by its temperature limit of $145\,[°C]$[18]. A summary of material properties is given in the Mid-Term Report [19, p.64].

[18]URL: `http://eurofibers.com/fibers/dyneema/`. Accessed: 17-06-2015

Forces Using the force estimation tool for the inflatable structure the sensitivity for the scaling of loads can be determined. Figure 6.18 displays the estimated structural loads throughout the inflatable for a total of 9 toroids and a set outer diameter of 12 and 18 $[m]$. The loads as displayed in Figure 6.18 feature solely the loads induced by aerodynamic pressure. The internal pressure loads follow separately. This sensitivity analysis is performed to evaluate the scalability of the CIA design. Previous HIAD designs, most predominantly the IRVE missions, feature smaller mission payloads and corresponding smaller diameters. Up to this point the highest diameter stacked toroid design flown is featured in the second and third IRVE missions, namely an outer diameter of 2.93 $[m]$.

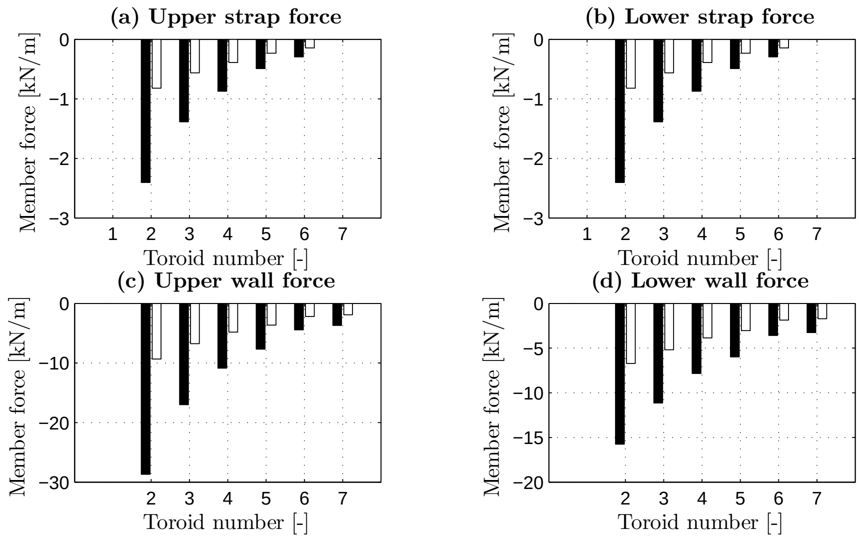

Figure 6.18: Internal force estimation for dynamic pressure 3750 $[Pa]$, no inflation pressure applied. Black bars are for a diameter of 18 $[m]$; white bars for 12 $[m]$

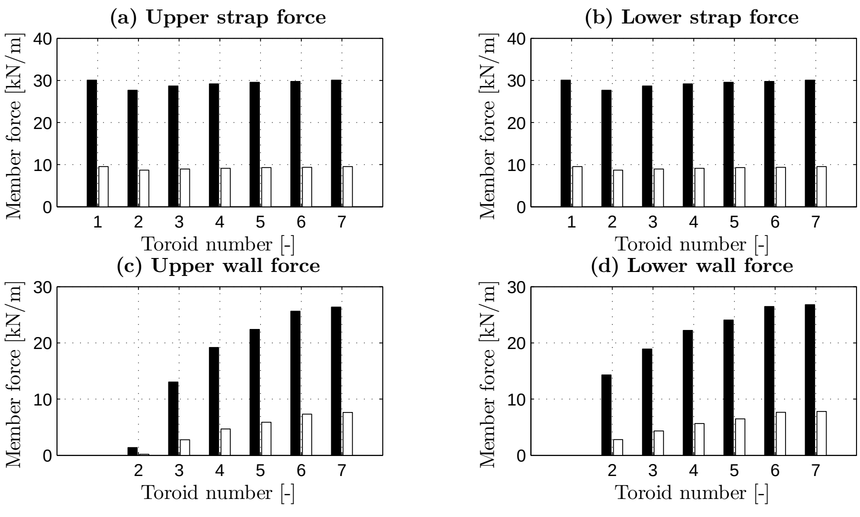

Figure 6.19: Internal force estimation for dynamic pressure 3750 $[Pa]$, with inflation pressure applied. Black bars are for a diameter of 18 $[m]$; white bars for 12 $[m]$

From the results of Figure 6.18 several conclusions can be made. Most importantly it shows that scaling of the inflatable is possible. Although a load increase can be observed for increasing diameter, this follows only from the additional axial loads. The induced bending moment is not represented in Figure 6.18 as this is carried circumferentially.

This followed from the verification and validation procedures explained in more detail in Appendix A.4. Moreover, loads are found to be within material capabilities.

Secondly the loads do not increase linearly over the diameter. This is the result of the scaling of the loads, to account for the decreasing circumference over which forces act. The reducing diameter causes an additional increase of the loads per unit length.

Thirdly the dynamic pressure loads of Figure 6.18 are found to be of a similar order as the internal pressure loads induced per Equation 12 at the root of the inflatable. Moving towards the tip of the inflatable these differences increase as the internal pressure loads are maintained whereas the loads induce by the dynamic pressure reduce towards the tip. This is further expanded upon in Figure 6.19 in which pressure loads are included.

The final conclusion with regards to scalability of the inflatable can be made on the basis of Figure 6.19. If the internal and external pressure loads are combined a minimum required thickness can be computed on the basis of requiring the structure not to yield. This parameter is relevant as foldability of the inflatable has to be considered as well. Foldability is an important parameter as the inflatable has to be stowed away during launch and the transfer towards Mars. From this yielding criterion and a typical material such as Kevlar 49 a minimum required thickness of below 0.01 $[mm]$ is found. Since this value is rather small the thickness of the inflatable is not a consideration from a folding perspective even for large diameters.

7 Final design

This chapter will discuss the final design together with the path taken to determine the final design parameters. First Section 7.1 will give an overview of the procedure followed to arrive at the final design. Secondly Section 7.2 shows the final determined trajectory taken by the CIA, after which Section 7.3 will present the design of the subsystems of the CIA. Lastly Section 7.4 summarises the design in terms of its performance. In addition to this summary a Reliability, Availability, Maintainability and Safety (RAMS) analysis is made, followed by an overview of the compliance to the requirements defined earlier.

7.1 Iteration process

In order to structure the design process, several design aspects were separated to facilitate iterating over the design. The goal is to find a design that complies with the requirements as given in Section 2.4. This is done by choosing a design concept containing a combination of an aerodynamic shape, trajectory, TPS, inflation structure and control system and analysing its performance. If the requirements are not yet met, the analysis of the concept is used to assess possible points of improvement if the requirements are not yet met. This is repeated until all requirements are complied with. The design process is started with an initial design which is assessed for its performance and used as a baseline for all following iterations. In the following paragraph, the steps composing an iteration are detailed.

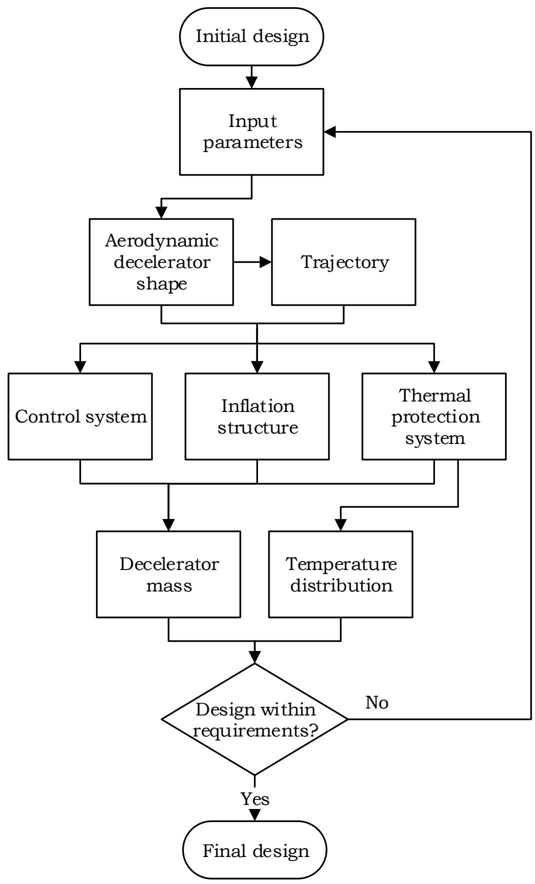

Figure 7.1: The iterative design process flowchart

The aerodynamic shape is chosen such that certain aerodynamic properties are achieved. This is largely done by optimisation since this allows a high fidelity in design optimisation objectives and constraints. These aerodynamic properties are chosen based on the previous design analysis. When a suitable aerodynamic shape is chosen, the resulting aerodynamic characteristics are used in determining a trajectory that complies with the initial and final velocity and height requirements. This is done by choosing a bank angle profile, defining the bank angle as a function of time to arrive at the required location and velocity. The aerodynamic shape and trajectory data containing velocity, density, Mach number and dynamic pressure is used for the inflation structure sizing, TPS lay-up and control system mass estimation:

- The shape and maximum dynamic pressure in the trajectory is used in determining the inflation structure, for which a parametric mass model is used to estimate the decelerator mass. Also, a representative truss structure is used to determine whether the loads do not exceed the material maximum loads.

- The heat flux into the system is calculated with the trajectory data. Numerically integrating the 1D heat equation with as input the heat flux data yields a temperature distribution for a given lay-up. The lay-up thickness and composition is then iterated until no layer temperature exceeds its maximum temperature while having the smallest thickness possible such that the TPS has the lowest possible mass.
- The control system mass is finally estimated using the required bank angle through the trajectory, moments of inertia and required velocity increments. These data are then used to estimate the control thruster fuel mass.

When the technical analysis of the concept is done, the design iteration is completed by analysing the results and assessing points where improvement can be made. When not all requirements are met, changes have to be made to the design. Several problems have been identified during the design phase:

- In case the temperature in the different TPS layers is calculated to be too high, irrespective of the thicknesses of the layers, the trajectory needs to be changed to facilitate a lower maximum dynamic pressure. This can be done by making the lowest point of atmospheric entry higher such that the density is lower. If achieving the required deceleration at this higher point is not possible with the current aerodynamic design, the drag coefficient is to be increased to allow the same deceleration at lower dynamic pressures.
- If the thermal protection system mass or inflation structure mass makes the total design exceed the mass requirement, also the maximum dynamic pressure is to be decreased such that physical loads on the structure and thermal loads on the TPS are decreased.
- If bank angle control does not perform well enough to allow a trajectory that satisfies the requirements, the lift over drag ratio can be increased to allow more freedom in trajectory choice.

The iteration strategy is visualised as a flow-chart in Figure 7.1. In this figure the solid lines represent design information flowing towards the areas that still need analysis. In the 'Design within requirements?' decision box, the check is made whether the mass is within budget and the temperature does not exceed the maximum temperature of the material. If this is the case, the design meets the requirements and is thus the acceptable choice.

7.2 Trajectory design

In this section the design of the trajectory followed by the spacecraft during the aerocapture and entry phase is presented. Also the motivation behind it, its sensitivity to changing atmospheric properties and the possibility to correct for these changes are explained. The main input with which the trajectory is calculated is the shape of the decelerator. This shape and the reasoning behind it is presented in Section 7.3.1. An overview of the aerocapture and entry phase trajectory is given in Figure 7.2.

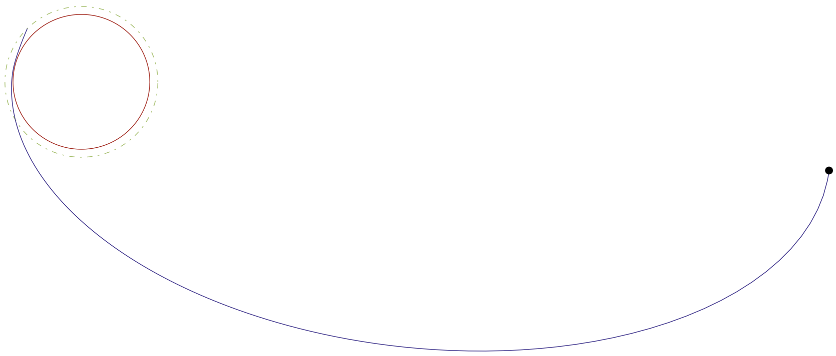

(a) The aerocapture trajectory visualised

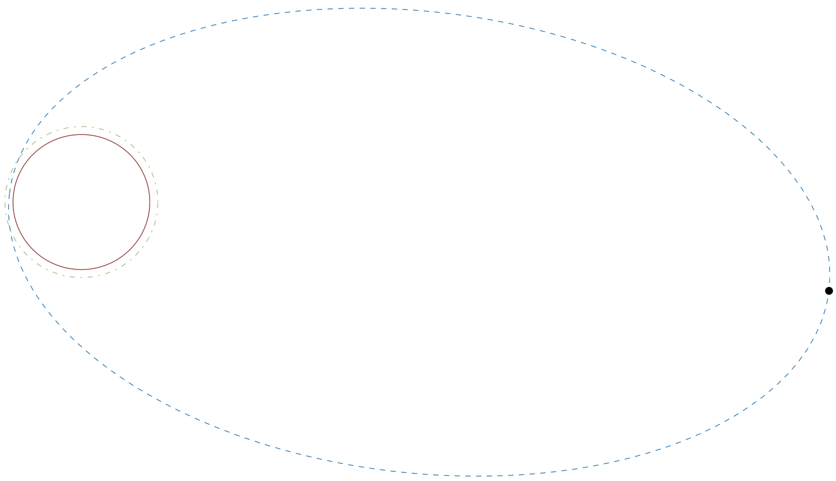

(b) The parking orbit after the pericentre raise

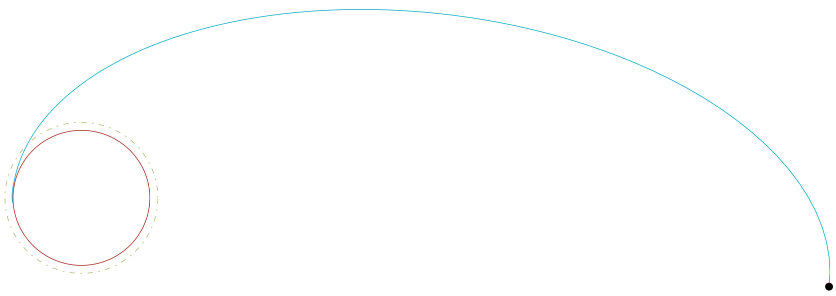

(c) The re-entry trajectory after lowering the orbit

Figure 7.2: Visualisation of the spacecraft trajectory. The apocentre is shown with a black dot

7.2.1 Aerocapture

The first phase of the trajectory is aerocapture, in which the objective is to lose enough energy to get in a Mars-synchronous orbit. The velocity that has to be obtained at the end of aerocapture in order to get in such an orbit is 4.53 $[km \cdot s^{-1}]$. In Figure 7.3 it can be seen from the velocity profiles that they all end at this velocity.

Furthermore the trajectory was chosen as high through the atmosphere as possible to lower the required TPS and structural masses. A pass higher through the atmosphere decreases both the heat flux and peak dynamic pressure which are used to design the TPS and inflatable structure respectively.

These two objectives are conflicting since a higher altitude corresponds to a lower density, which makes it harder to achieve the required velocity change. In order to still reach the desired velocity, two options are available: with a longer aerocapture, the lower deceleration at higher altitudes is applied for enough time to reach the final velocity, and with a higher drag coefficient or frontal area the aerodynamic deceleration is increased for equal dynamic pressures.

A longer aerocapture can be achieved by improved control over the vehicle, which is accomplished by a higher lift coefficient. A longer aerocapture however, increases the total heat load, which may lead to a higher TPS mass.

In order to facilitate both objectives for aerocapture it is thus important that the aerodynamic shape has a high lift-to-drag ratio as well as a high drag coefficient. For the entry and descent phase conflicting objectives for the shape are found since a lower drag coefficient is required such that more time is available in this phase to manoeuvre. In Section 7.2.4 a conclusion is drawn on the properties needed from the design of the aerodynamic shape.

In Figure 7.3 the parameters that were recorded during the simulation are shown for the nominal trajectory and two trajectories created for a 10% increase and decrease in atmospheric density. This change in density is based on the maximum estimated error in the ESA Mars climate database v5.2 [43].

The bank control profile for the trajectories can be changed, by varying bank angle and timing, to attain the same exit velocity for each atmospheric density. This exit velocity is needed to get into a Mars-synchronous orbit. The fact that a bank control profile is available for each density proves that a density change of ±10% can be accounted for. However, some other parameters of the trajectory do change. The peak acceleration and dynamic pressure increase for a higher density. The TPS and inflatable structure should be sized on the worst case. Also the time passed and the position of exit (defined by τ in Figure 7.4) are different for each trajectory. These changes have a significant effect on the entry and descent phase. This effect will be explained in Section 7.2.3.

7.2.2 Parking orbit

After aerocapture the spacecraft goes into an elliptic orbit. In the apocentre a boost is given to raise the pericentre to 200 $[km]$ above MOLA. In this parking orbit the vehicle can wait for dust storms to vanish and can observe the entry conditions it will be subjected to. Because the parking orbit is Mars-synchronous the pericentre is over the same point on the Mars surface so entry conditions can be monitored for the actual entry point.

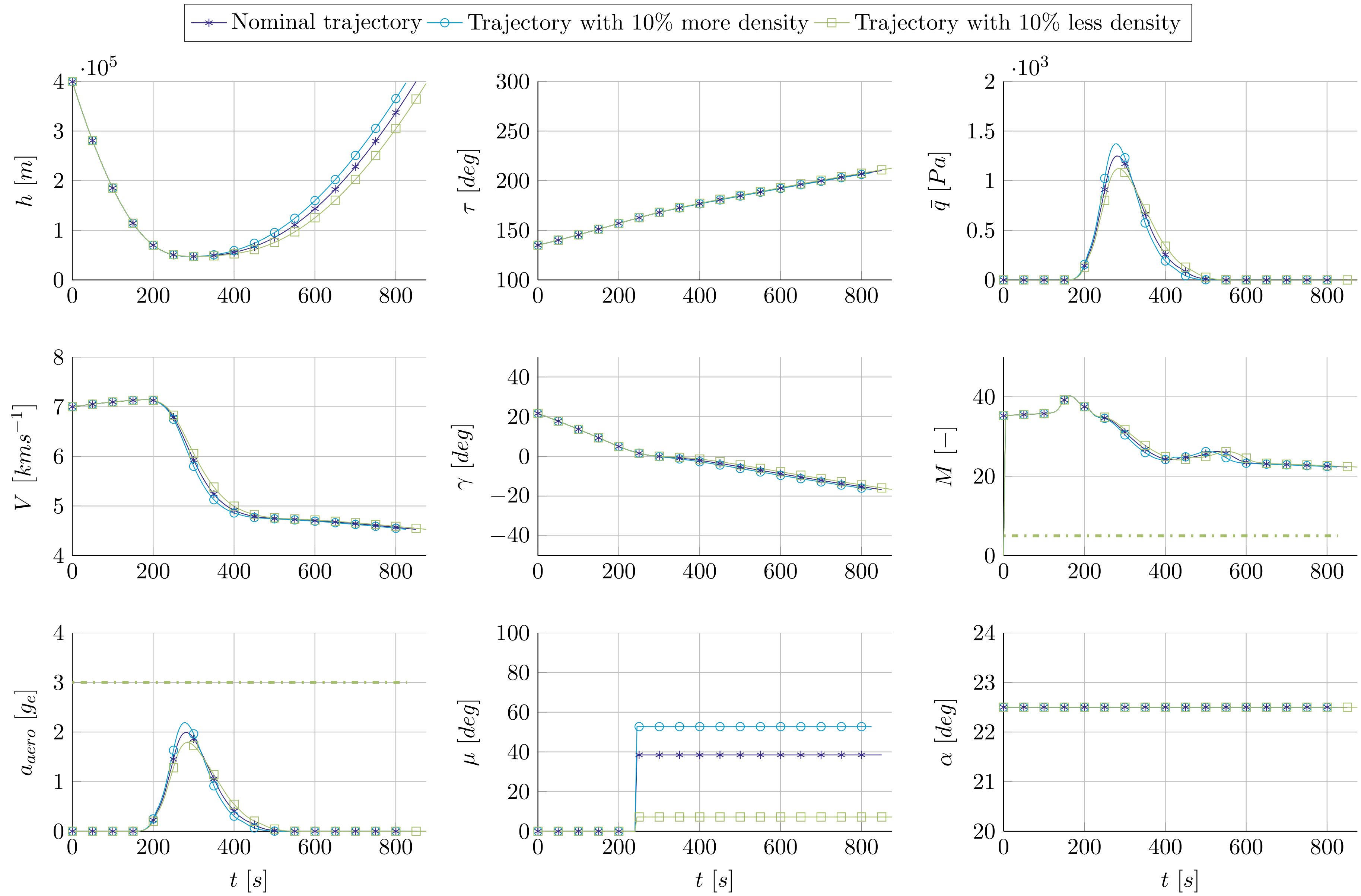

Figure 7.3: Results of the aerocapture trajectory for three different density profiles. The trajectories with modified density are corrected (changed μ profile) to maintain the same exit velocity. The horizontal dashed lines are design limits (for the M and **a** plots)

The first entry opportunity is after approximately one day from the start of the aerocapture and entry phase. From that moment every sol (Martian day) an opportunity for entry arises. This gives in total nine opportunities for entry in little over nine days. This is the maximum that can be achieved within the ten days that are available for the aerocapture and entry phase. In principle the spacecraft could stay in the parking orbit much longer if it would be necessary. However the current mission is fully designed for an aerocapture and entry phase of at most 10 days. i.e. crew operational items are insufficient to sustain a longer mission.

For every entry opportunity the decision to start entry has to be made half a sol before the entry. In the apocentre a boost opposite to the flight direction should be given to lower the pericentre. When the vehicle reaches the atmosphere in this lower orbit the entry and descent phase begins.

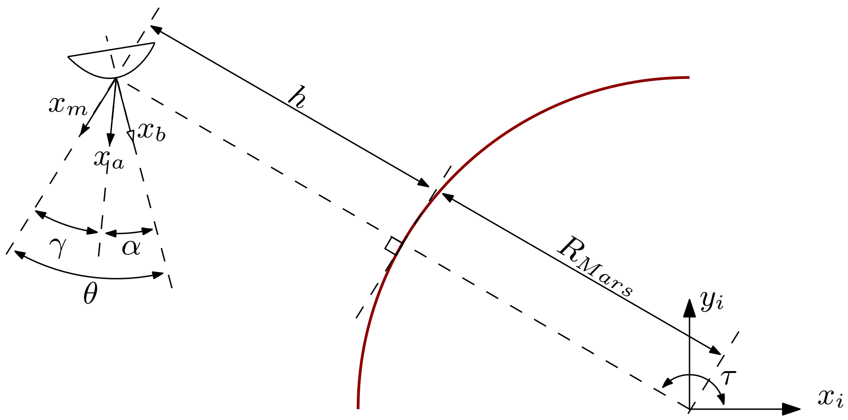

Figure 7.4: The angles used in the simulation of the trajectory

7.2.3 Entry and descent

The boost given in the apocentre before entry is determined such that the initial flight path angle (γ as in Figure 7.4) of the entry is 17.2 $[deg]$. Corresponding to this flight path angle an entry location (defined by τ in Figure 7.4) is dictated by the exit location of the aerocapture. With this location, flight path angle and the control as shown in Figure 7.6, the entry trajectory and final position are attained as shown in Figure 7.5.

The objective of the entry and descent phase is to get to a height of 15 $[km]$ with a velocity of $M = 5\,[-]$ while keeping the deceleration under $3g_e$.

In order to keep the deceleration low, especially at the end of the descent, a low drag coefficient is required. This objective clearly conflicts with the properties needed for the aerocapture. As can be seen in Figure 7.6 the deceleration at the end of the aerocapture and entry phase is right at the $3g_e$ limit for the nominal trajectory. Meaning the drag coefficient could not have gotten any higher.

In the last part of the descent also a high dynamic pressure is attained, which is the parameter that is the main input for inflatable structure design. The highest dynamic pressure is reached by the trajectory with a 10% lower density.

In Figure 7.5 next to the nominal trajectory also two trajectories with a 10% higher or lower density are plotted. The trajectory in the higher density atmosphere would land at a location before the nominal landing location if no change to the control is done. The trajectory that is shown for 10% higher density is one with control that allows the vehicle to fly further (increased μ). This control causes the vehicle to overshoot the nominal landing location. Any point between these two margins is a possible landing location. It is thus proven that the nominal landing location can be achieved with 10% higher density.

The trajectory for a 10% lower density would normally overshoot the nominal landing location. The control is thus changed in order to push it towards the surface faster (lower μ). This control causes the vehicle to land before the nominal landing location. Again any point between these two margins is a possible landing location. This proves that the nominal landing location can be attained with 10% lower density.

In Figure 7.5 it can also be seen that the entry locations for each trajectory is different. This flows down from the aerocapture where the exit location for these trajectories where different as well.

The time passed during both the aerocapture and the entry and descent phases are also different for each trajectory. During this time the landing location has rotated with Mars in the same direction as the flight direction of the vehicle. Three points for the nominal landing location can be distinguished in Figure 7.5. Each point for the time one of the trajectories would arrive.

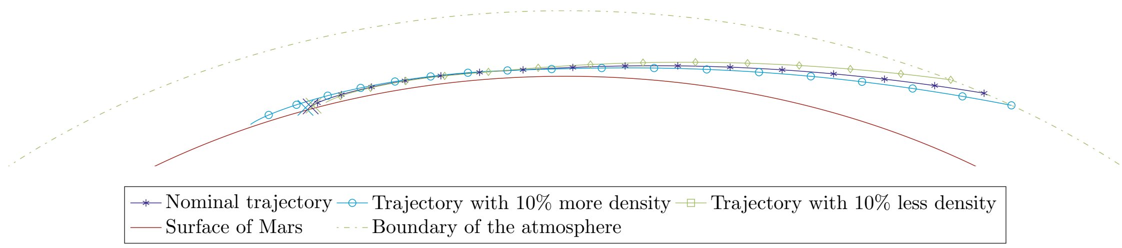

Figure 7.5: The re-entry trajectory for three different density profiles. The trajectories with modified density are corrected (changed μ profile) to show the ability to reach the desired landing location.

In Figure 7.6 it can be seen that the Mach number at a height of 15 $[km]$ is approximately 5 for all trajectories. The entry trajectory with a lower density is the shortest, however it also decelerates fastest overshooting the $3g_e$ requirement by 23%. This higher deceleration is needed to reach the required velocity of $M = 5\,[-]$.

The entry trajectory with a higher density is the longest. The deceleration is also faster than for the nominal trajectory and it also overshoots the $3g_e$ requirement by 11%. This higher deceleration is caused by the denser atmosphere at a height of 15 $[km]$.

7.2.4 Required properties for aerodynamic shape design

The required aerodynamic properties for the different parts of the aerocapture and entry phase are conflicting. For the aerocapture phase a high drag coefficient as well as a high lift coefficient is needed. For the entry phase still a high lift coefficient is needed, however also a low drag coefficient is required.

Compromising between these requirements an angle of attack has been chosen at which the $L \cdot D^{-1}$ is maximal in order to maximise the lift for certain drag. The aerodynamic

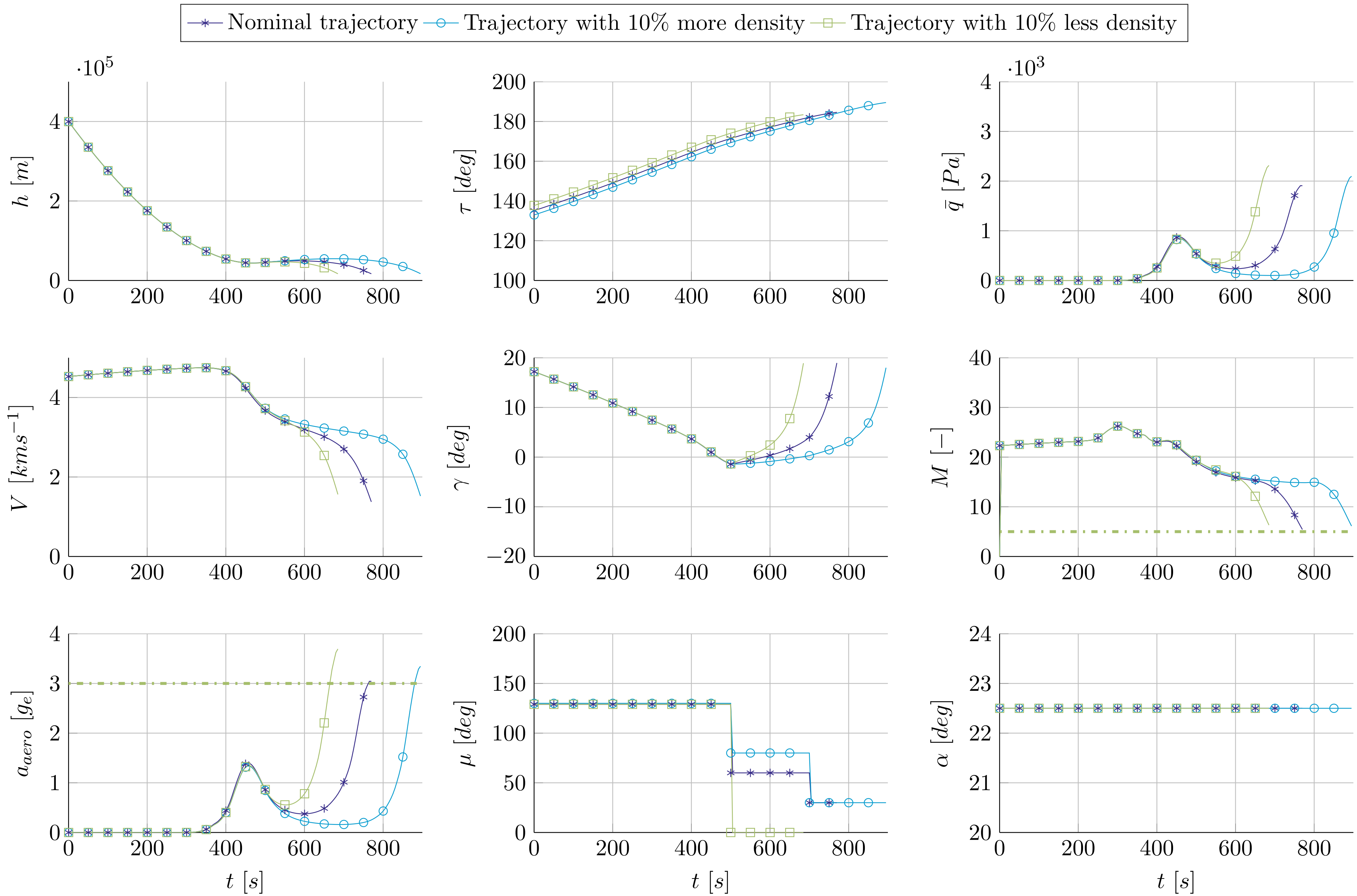

Figure 7.6: Results of the re-entry trajectory for three different density profiles. The trajectories with modified density are corrected (changed μ profile) to show the ability to reach the desired landing location. The horizontal dashed lines are design limits (for the M and **a** plots)

shape should be designed in such a way that the drag at maximum $L \cdot D^{-1}$ is a perfect compromise between the objectives for the aerocapture and entry & descent phases.

7.3 Subsystem design

This section will present the final design of the CIA subsystems. First Sections 7.3.1, 7.3.2 and 7.3.3 will discuss the inflatable structure, deployment mechanism and inflation system respectively. Secondly Section 7.3.4 will mention the final control system design. Lastly Section 7.3.5 will give an overview of the crew module design.

7.3.1 Inflatable structure

The inflatable structure consists of three main design elements: The aerodynamic shape, structural arrangement and TPS design. These elements will be covered in the subsequent sections in the aforementioned order.

Aerodynamic shape The CIA will have a shape similar to configuration D in Figure 6.10 in Section 6.2.2, with a radius of 6 $[m]$ and a half cone angle of approximately $\theta_{cone} = 70\,[deg]$. The curved nose will have an outer radius of $2.5\,[m]$. The cross-sectional offset at the rear of the body is approximately $0.91\,[m]$. At an angle of attack of $\alpha = 22.5\,[deg]$, it has a lift-to-drag ratio of $L \cdot D^{-1} = 0.35\,[-]$ and a drag coefficient of $C_D = 1.3\,[-]$. At this angle of attack, a CG-offset of $C_M \cdot l \cdot {C_X}^{-1} = 0.5\,[m]$ is required to trim the vehicle around the pitch axis. It has a moment derivative of $C_{M_\alpha} = -0.21\,[rad^{-1}]$.

Figures 7.7a through 7.7d show the final outer mould line of the CIA. The final shape is composed of circular cross-sections stacked on top of each other, with an offset in the z-direction. The CIA is $1.8\,[m]$ high and has a maximum offset of $0.9\,[m]$.

Figures 7.8a through 7.8d display the aerodynamic characteristics of the vehicle through an angle of attack range of $0\,[deg] < \alpha < 30\,[deg]$. As can be seen from these plots, the behaviour of the lift-to-drag ratio and the moment coefficient in pitch is near linear. This linearity ensures predictable vehicle behaviour over the entire angle of attack range.

Structural analysis and design The inflatable consists of ten toroids, stacked aside and on top of one another. The asymmetric shape obtained by aerodynamic optimisation is attained by arranging the toroids at an angle with respect to one another. The result is an assembly of circular inflatables, placed at differing radial distances with respect to the centre body. While the structural performance of the inflatable is altered, an asymmetric configuration is achieved by stitching the toroids and varying the radial length of the straps over the sphere cone circumference. Structural performance is altered in the sense that the asymmetry of the configuration implies additional concerns for aero-elastic phenomena, such as limit cycle oscillations, for example. These phenomena, however, are highly unpredictable and warrant additional wind tunnel and flight testing in any case.

The number of toroids is based on Figure 6.16d, which shows that mass decreases beyond ten toroids are insignificant. Moreover, ten toroids are sufficient to adequately represent the optimised aerodynamic shape.

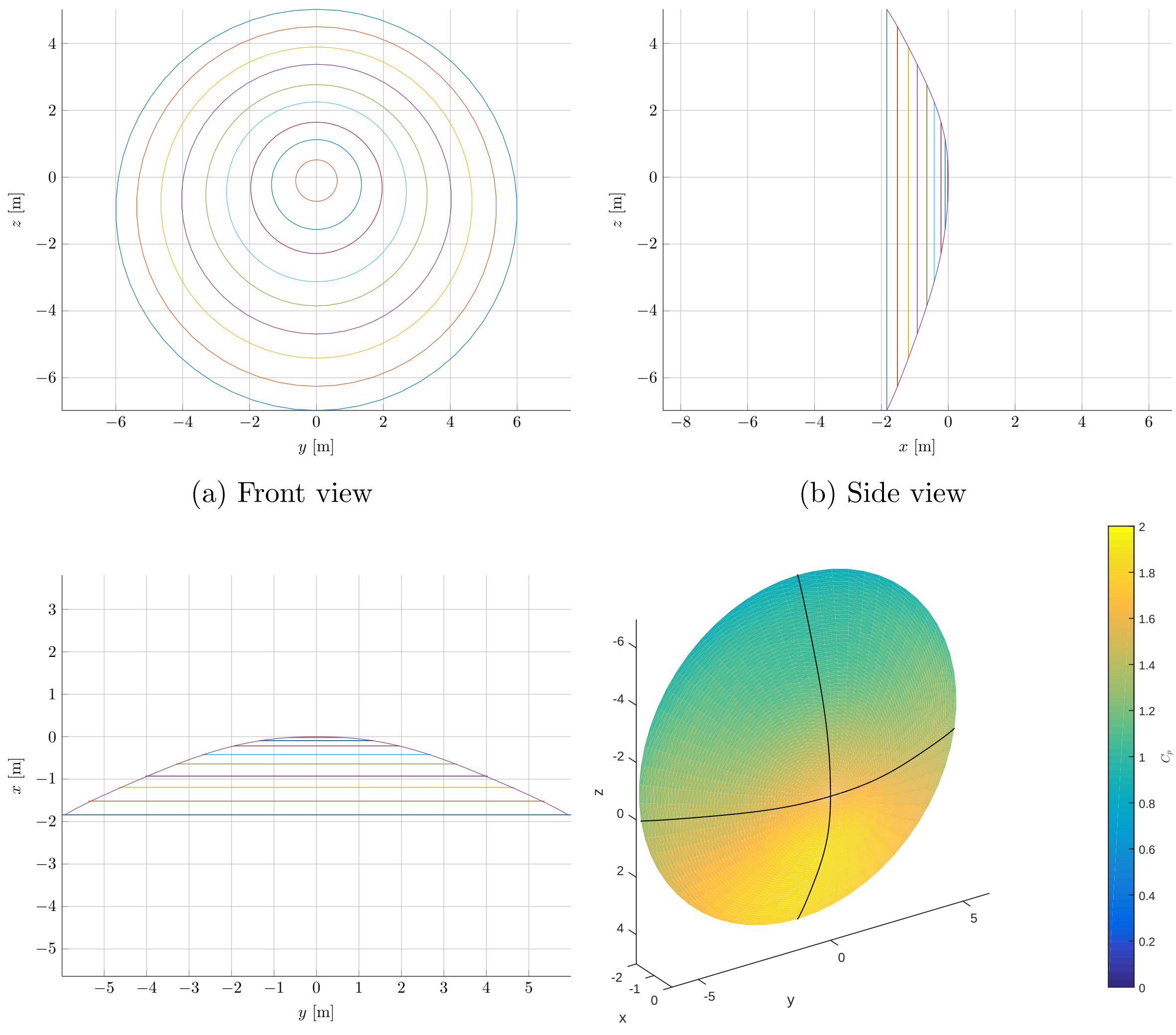

(a) Front view

(b) Side view

(c) Top view

(d) 3D view

Figure 7.7: Front, side, top and 3D view of the inflatable shape

Structural loads are carried by PBO Zylon® fibres, interlaced warp and weft to provide load-carrying capability in all required directions: circumferential and hoop. As such,fibres are woven perpendicular to each other. To this end, a plain weave pattern is adequate.

For the load analysis, the ultimate load is calculated by multiplying the limit load, a peak dynamic pressure of 2300 $[Pa]$ (with a 10% density deviation from the nominal density), with a factor of safety of 1.5. This factor of safety respects NASA standards for composite structures and accounts for uncertainties in the maximum external loading applied [44]. From Figure 6.17 and the parametric mass model it follows that for this ultimate load Vectran and aramid fibres Kevlar and Technora have exceeded their minimum gauge thickness, set at 0.125 $[mm]$ for aramid fibres.

Such a minimum thickness is achievable for a plain weave, based on its proposed application in IRVE-4 in a 0.127 $[mm]$ lay-up [45] and commercial availability of these weave patterns for Kevlar[19]. Based on available grades of Vectran[20], its minimum thickness

[19]URL: `http://www.cstsales.com/aramid_fabric.html`. Accessed: 16-06-2015
[20]URL: `http://www.swicofil.com/vectran.html#Grades`. Accessed: 17-06-2015

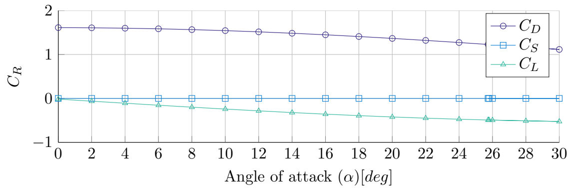

(a) Force coefficients in the aerodynamic frame versus angle of attack

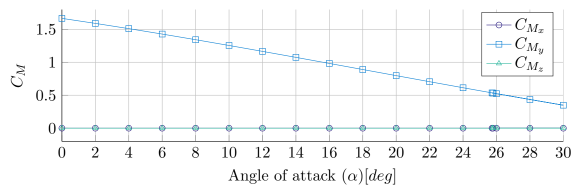

(b) Moment coefficients in the body frame versus angle of attack

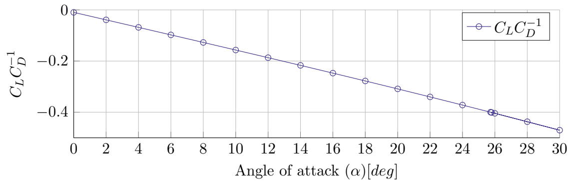

(c) Lift-to-drag ratio versus angle of attack

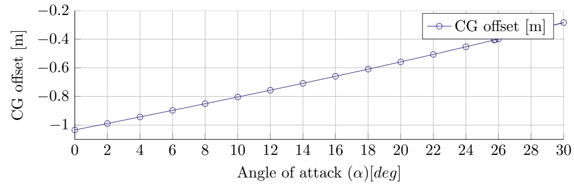

(d) Required CG-offset versus angle of attack

Figure 7.8: Various aerodynamic characteristics of the Controllable Inflatable Aeroshell over the angle of attack range $0\,[deg] < \alpha < 30\,[deg]$

is set at $0.023\,[mm]$. PBO Zylon®, on the other hand, remains at its minimum gauge thickness for this loading. This minimum thickness is assumed to be the same as that of Kevlar, an assumption supported by the same yarn count and sample thickness in a study on ballistic impact on Kevlar 49 and PBO Zylon® [46].

PBO Zylon® offers a mass advantage of approximately $5\,[kg]$ with respect to Technora and Vectran and $10\,[kg]$ with respect to Kevlar. This mass advantage is the first reason for opting for PBO Zylon®. In addition, PBO Zylon® is capable of withstanding higher temperatures, $400\,[°C]$ for short exposure versus $250\,[°C]$ for Kevlar 49, one of the key drivers for its implementation in the upcoming THOR mission [47]. While in principle this would allow for a lighter TPS, this advantage is included as an additional contingency. At this stage, PBO Zylon® fibres have not been applied in previous HIAD missions, in contrast to Kevlar 49 fibres. Since the mass limit is not exceeded, the mass advantage is not required and reliability is preferred due to the criticality of the inflatable.

The structural feasibility of the configuration is ascertained by the truss-based analysis model. The truss-based analysis model uses the representation in Figure 7.9. Cross-sections that displayed the most extreme loading are the short side, defined at the inflatable minimum diameter, and the long side, defined at the inflatable maximum diameter. Due to the skewness, load asymmetry is introduced which is thereby evaluated by some extent through evaluation of multiple cross-sections.

For an inflation pressure of $169\,[kPa]$, required to bring all members into tension, structural loads are as obtained in Figures 7.10 and 7.11. It can be observed that the maximum running load in the walls is $50\,[kN \cdot m^{-1}]$. Translating this to a stress by dividing through the $0.125\,[mm]$ thickness yields a maximum stress of $400\,[MPa]$, well below the (room-temperature) tensile strength of $5.8\,[GPa]$ for PBO Zylon®. In the straps, the maximum running load is $100\,[kN \cdot m^{-1}]$, translating to an $800\,[MPa]$ stress. As such, the minimum gauge thickness is well above the required thickness determined by preliminary load and stress analysis. Firstly this takes into account material strength loss at higher temperatures, as PBO Zylon® retains 80% of its strength when exposed to $200\,[°C]$. Secondly, it takes into account a wide margin for material uncertainties, production deficiencies and

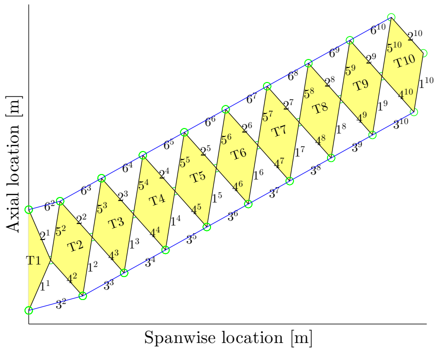

(a) Cross-sectional view at maximum diameter

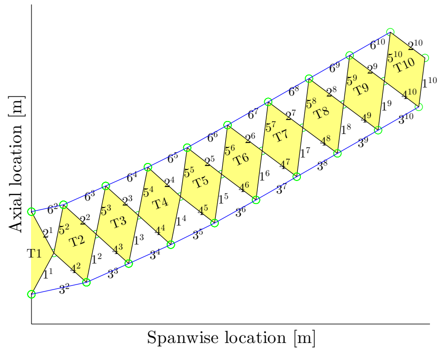

(b) Cross-sectional view at minimum diameter

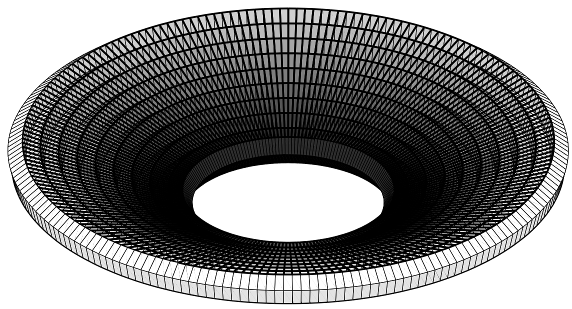

(c) Isometric view

Figure 7.9: Structural representation of inflatable structure

unpredicted structural phenomena. The flexible material mass, given a uniform thickness of 0.125 $[mm]$ for radial straps and toroid material, is 110 $[kg]$.

Stitching of the fabrics making up the toroids is used for the joints of the inflatable, on one hand to join the toroids to each other and on the other hand to join the toroids to the radial straps. This is a method excellently suited, applied, tested and proven in the IRVE missions [38, 48, 49]. Joints are thereby proven high-strength and suitable for space application and a stacked-toroid configuration.

To prevent the inflation gas from leaking, the structural PBO Zylon® layers are coated with a gas barrier in the form of a 50 $[\mu m]$ Upilex layer. This uniform thickness coating adds an estimated 25 $[kg]$. The thickness of this coating is feasible, in line with findings by Samareh and Miller [40, 50] and available Upilex grades of 12.5, 25, 50, 75 and 125 $[\mu m]$[21,22].

[21] URL: `https://www.ube.com/content.php?pageid=81`. Accessed: 16-06-2015

[22] URL: `http://dasp.mem.odu.edu:8080/~deorbit_sp12/ref/UPILEXS%20Data%20sheet.pdf`. Accessed: 16-06-2015

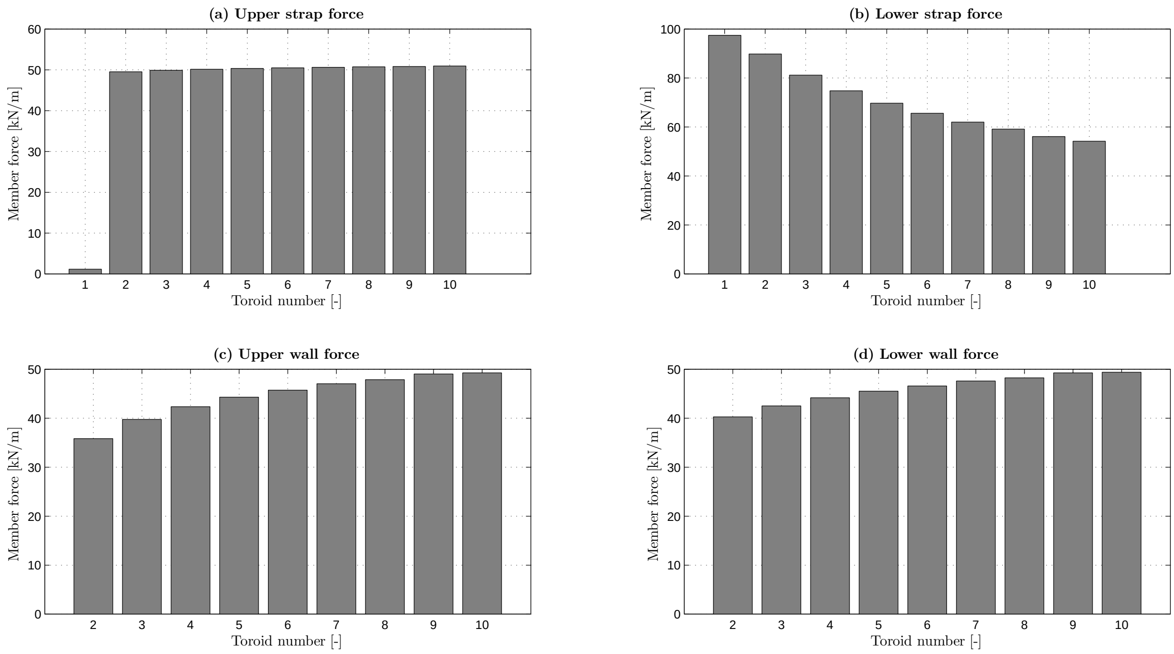

Figure 7.10: Cross-sectional running loads inflatable at maximum diameter

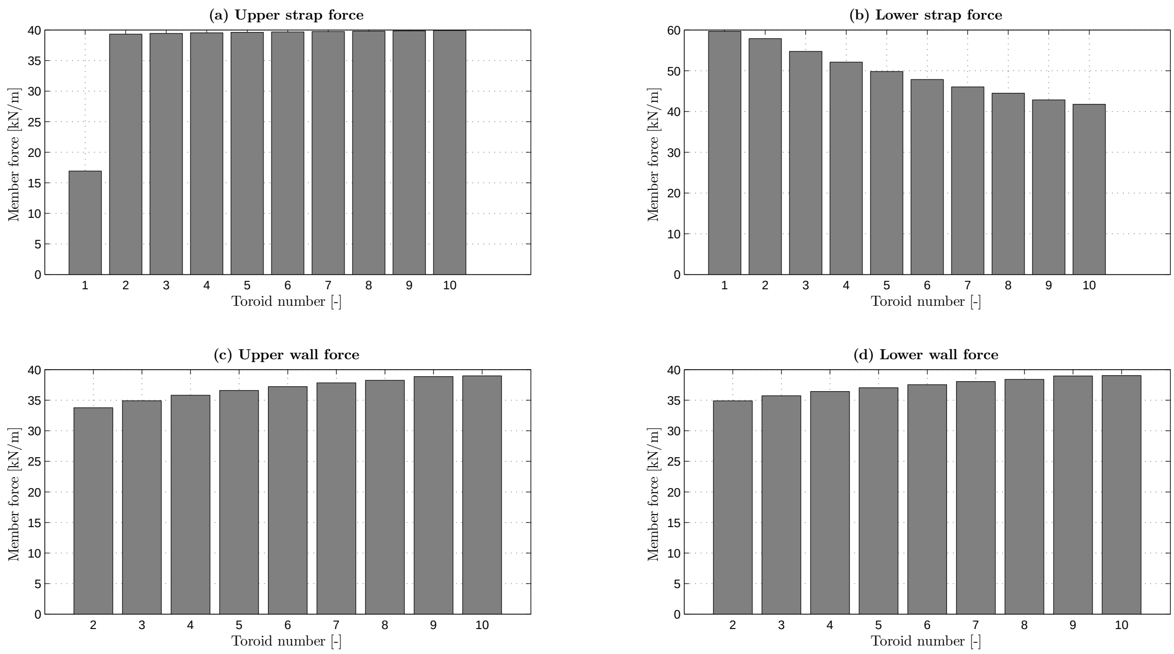

Figure 7.11: Cross-sectional running loads inflatable at minimum diameter

Thermal Protection System design For a given trajectory and lay-up it is possible to check the temperature distribution for failure. From the sensitivity analysis in Section 6.2.3 it is deducted that a Nextel BF-20 layer with Pyrogel® 6650 as insulator is preferable for mass reduction purposes. However, due to the relatively low emissivity of Nextel the wall temperature exceeds the limit as high aerodynamic heating can not be radiated away efficiently. For this reason a slightly heavier alternative, Nicalon™, is needed. Nicalon™ is a type of silicon continuous fibre that can withstand temperatures up to 2073 $[K]$. Furthermore it has a much higher emissivity, which greatly reduces the wall temperature. It performs comparable or even better on its ability fold compared with Nextel BF-20 [2]. The sensitivity analysis has shown that for a diameter of 12 $[m]$ it was not possible to find a viable thickness for the Nextel lay-ups. Several iterations have been performed to reduce the heat flux such that Nextel BF-20 became viable, however these attempts resulted only in an approximate mass of 500 $[kg]$. Therefore Nicalon™ is chosen as TPS-layer and Pyrogel® 6650 as insulation layer for the lay-up in the final design. In addition to the Upilex coating on the inside of the PBO Zylon® layer, two thin impermeable layers of kapton are placed between the Pyrogel® and Zylon® to prevent hot gasses reaching the Zylon® layer [22, 45].

The incoming heat flux, or aerodynamic heating of the chosen trajectory is shown in Figure 7.12. The heat maximum heat flux is approximately 21 $[W \cdot cm^{-2}]$. The maximum heat flux for the entry phase is 7.3 $[W \cdot cm^{-2}]$. It is expected that this entry phase is not leading for the design and therefore it is not shown. In the figure three fluxes are shown for the aerocapture phase, which represent the change in heat flux when the atmospheric density is over- or underestimated by 10%. This 10% comes from the uncertainties in the density as explained in Section 7.2. Surprisingly, when the density is underestimated by 10%, the heat load becomes slightly higher as the duration of the trajectory is longer and this results in a higher required thickness. This case is used as reference heat flux for which the lay-up is optimised.

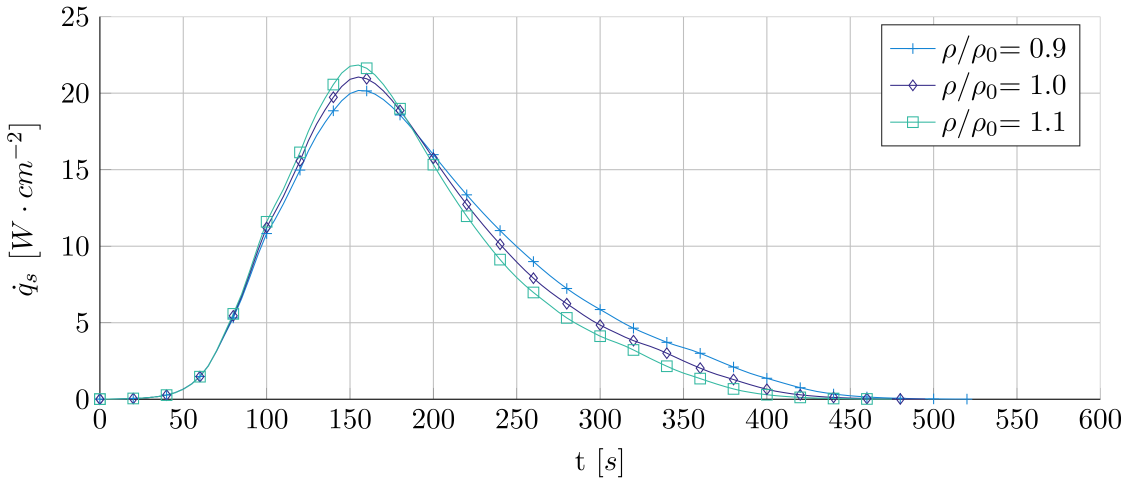

Figure 7.12: Heat flux of the aerocapture for different density levels

Figures 7.13a and 7.13b show how the heat propagates though the material during the aerocapture and entry phase of the chosen trajectory. It is clear that the aerocapture is indeed leading for the design as the heat load during this phase and resulting temperatures are higher. The figure can also be used to understand the required thicknesses. The Nicalon™ and Pyrogel® layers remain far below their maximum temperatures, 2073 $[K]$

and 923 $[K]$ respectively. Therefore the Nicalon™ layer is as thin as possible, which is 0.508 $[mm]$. For the kapton and PBO Zylon® layers the maximum temperature is set at 473 $[K]$ to remain their structural integrity. This is why the insulation layer is needed such that the temperature drops to this maximum through the Pyrogel® 6650. The required thickness for this is 2.439 $[mm]$. Each kapton layer is also very thin which comes down to 0.025 $[mm]$.

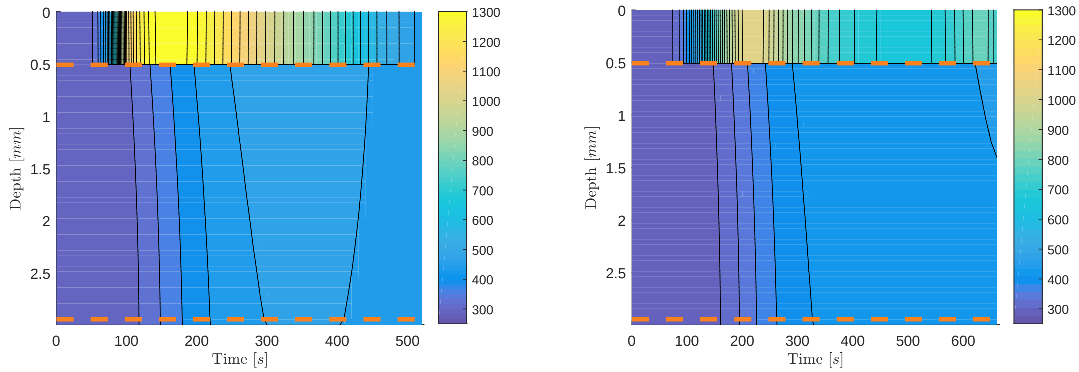

(a) Aerocapture (b) Entry

Figure 7.13: Heat propagation during both decelerations

The areal density of this lay-up is 1.816 $[kg \cdot m^{-2}]$. The frontal surface area or wetted area is 120.9 $[m^2]$, as is obtained from the aerodynamic analysis. Multiplying the surface area with the area density results in a frontal TPS mass of 219.6 $[kg]$. Note that the frontal TPS covers the rigid centre body of the vehicle. For the protection on the other side of the inflatable very thin layers of kapton and Nextel AF-14 are assumed to be sufficient. The resulting area density is 0.342 $[kg \cdot m^{-2}]$. The area onto which it is applied is assumed to be the frontal surface area minus the centre body area, which equals to 105.0 $[m^2]$. The resulting mass is 35.96 $[kg]$. The total TPS mass for the lay-up shown in Figure 7.14 yields 255.6 $[kg]$.

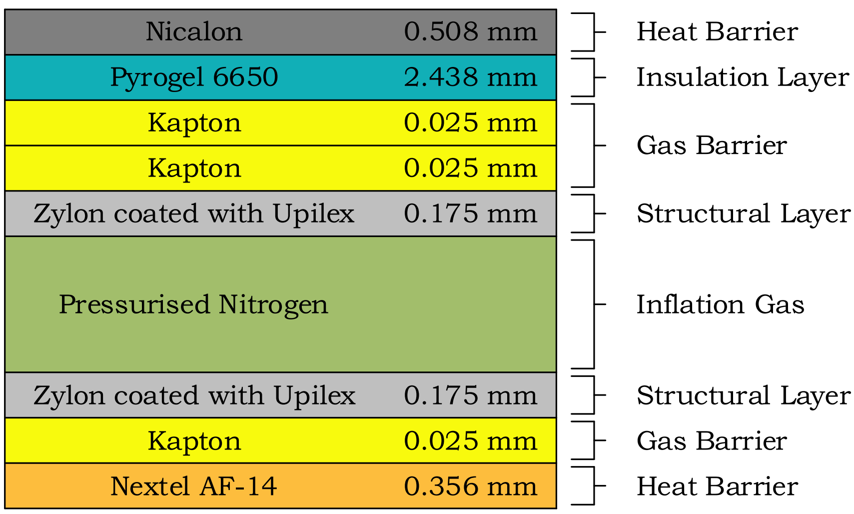

Figure 7.14: Final design for the Thermal Protection System

7.3.2 Deployment mechanism

This section presents the design of the deployment mechanism required to bring the inflatable from its stowed to its deployed configuration. It is key that this action is performed with maximum reliability, since deceleration of the entry vehicle and thereby mission success hinges on the aerodynamic surface area provided by the inflatable decelerator. This design comprises selection of a Hold-Down and Release Mechanism (HDRM), its detachment and deployment.

Deployment of inflatables can be performed either by unrolling, unfolding or deploying a strut [51, p.222-227]. Figure 7.15 serves as qualitative comparison between the principles of these systems. The unrolling and unfolding deployment mechanisms are deemed impractical for the following reason. Unrolling and unfolding in lateral direction from the centre body are less package efficient than deploying it as a strut. Unrolling requires a hub about which is rolled and results in multiple toroids stacked together laterally. Unfolding compresses the toroids and thereby also features multiple toroids in lateral direction. Deploying, on the other hand, stretches the sphere cone shape in axial direction and thereby features less material in lateral direction. Unrolling and unfolding thus take up more space in radial direction through denser packing in this direction, while deploying stretches the packaging over the axial direction.

A key driver for the use of inflatable aeroshells is the launch vehicle constraint on diameter in stowed configuration. By requiring a smaller diameter for aeroshell packaging, a bigger volume is left free for the centre body design. This results in maximum efficiency in the use of available diameter and thereby a more mass-efficient design, since an increase in centre body diameter is deemed less mass-expensive than an increase in inflatable diameter for a given deployed diameter. This is a result supported by the sensitivity analysis presented in Section 6.2.4.

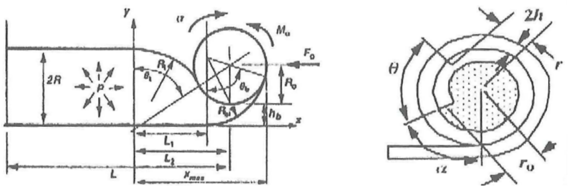

(a) Unrolling strut [51, p.222]

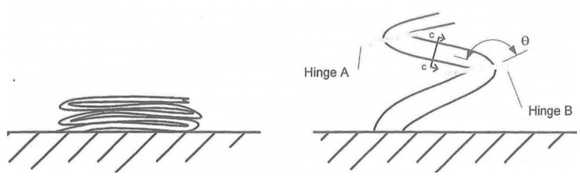

(b) Unfolding strut [51, p.226]

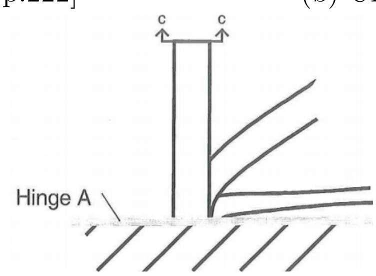

(c) Deploying strut [51, p.227]

Figure 7.15: Overview of various deployment possibilities [51]

Moreover, less interference between flexible material is present when deploying the inflatable sphere cone as a hinge, as opposed to the folding and rolling of the toroids in the other two methods. This decreased amount of interference reduces the unpredictability and thereby increases reliability of the deployment procedure.

Deploying requires attachment points at which the outer toroid is held in place in stowed configuration. The axial length over which the inflatable is held in stowed condition is equal to the inflated radius minus the centre body radius corrected for the half-cone angle, equal to 2.6 $[m]$. Attachment points will therefore be located at the side of the crew module, such that the inflatable is wrapped about the vehicle in stowed condition.

The inflatable may moreover be covered by a shroud to provide additional protection from the space environment, primarily space debris, UV and radiation. A possible solution would be a coated Kevlar or Vectran canopy, as used for example in IRVE-II [52]. For IRVE the shroud weighed 1.9 $[kg]$, for an approximate spanned area of 2 $[m^2]$. Scaling this yields a shroud mass of 60 $[kg]$ for the design at hand, where the shroud is required to span approximately 85 $[m^2]$. This shroud mass is significant on a decelerator mass of 1000 $[kg]$ and such mass estimates are confirmed by a first-order estimate of a coated Vectran canopy, with a density of 1500 $[kg \cdot m^{-3}]$ [50], which would yield a mass of 64 $[kg]$ for half a millimetre thickness. Such a shroud is therefore infeasible in terms of mass.

The canopy is not only infeasible, but in addition not required. The outer layers of the inflatable are composed of Nicalon™, a silicon carbide. silicon carbide materials are currently being developed for high-load applications. Moreover, their main drawback is a reduction of performance under oxidised conditions [53]. As these conditions are not experienced within the mission no drawback can be mentioned for using Nicalon™ as outer layer.

The asymmetry of the inflatable does not form a problem, due to the foldability of the flexible material. The top of the inflatable is wrapped over itself such that the attachment ring is concentric with the crew module.

To prevent the inflatable from de-attaching from the centre body and crew module during launch and transfer, a strap band is employed that wraps around the top of the inflatable and keeps it in place. The band features a cushioning part to prevent chafing and a bolt-and-nut clamping system that facilitates detachment. It is key that the strap band is reliable, both in terms of holding the inflatable to the centre body and releasing it. An example product that fulfils these demands and has seen space application is produced by Voss Aerospace[23]. Pre-tensioning of the strap band and bolt-and-nut fastening mechanism are essential pre-flight activities to ascertain proper functioning.

To separate the bolt-and-nut fastening mechanism of the attachment belt and thereby initiate deployment events HDRM's are used. As deployment is a singular event in time, one-time use is warranted. Reusable mechanisms typically have a larger number of moving parts and thereby a lower reliability than non-reusable mechanisms[24]. Reliability is key, since deployment of the CIA is of singular importance to aerodynamically decelerate the vehicle. To this end, pyrotechnic cutters are the pre-eminent solution by their high and proven reliability in space operations, low mass and low shock imparted to the vehicle. Example cutters are Chemring Hi-Shear cutters, applied in multiple space missions, such as the Mars observer mission[25]. These possess a mass in the order of one hundred grams. For their criticality in mission success, redundancy of HDRMs is key and multiple cutters are required to be present.

[23]URL: `http://vossind.com/assets/band-clamps---aerospace.pdf`. Accessed: 08-06-2015

[24]URL:`http://www.esa.int/Our_Activities/Space_Engineering_Technology/Mechanisms/Hold-Down_and_Separation_Systems`. Accessed: 04-06-2015

[25]URL:`http://www.hstc.com/Products/OrdnanceProducts/CuttersBoltRodandCab/`. Accessed: 08-06-2015

This choice of separator mechanisms is moreover supported by an analysis for a tension cone, similar to a stacked toroid concept in deployment, by Miller et al. [50]. Severing corset lacing by pyrotechnic cutters is therein deemed the most favourable option.

It is essential that the diameter of centre body and crew module is slightly smaller than the maximum 5 $[m]$ diameter to account for inflatable stowage. To this end, the centre body diameter of 4.5 $[m]$ rather than 5 $[m]$ is imposed. In addition, this smaller diameter accounts for launcher fairing considerations.

A first-order mass estimate is 10 $[kg]$, a conservative estimate considering two Hi-Shear cutters of 0.1 $[kg]$, a latch of similar mass[26], and a 9.50 $[kg]$ Vectran strap of 8 $[mm]$ thickness and 5 $[cm]$ width. These values are deemed sufficient to hold together the inflatable to a first-order estimate.

Deployment is schematically summarised in Figure 7.16. Detachment is followed upon by inflation, which gives the inflated system the shape defined in Section 7.3.1. Inner bladder volumes are inflated first, to provide more stiffness towards the root where loads are highest and provide a stiff basis for the outer bladder volumes to inflate.

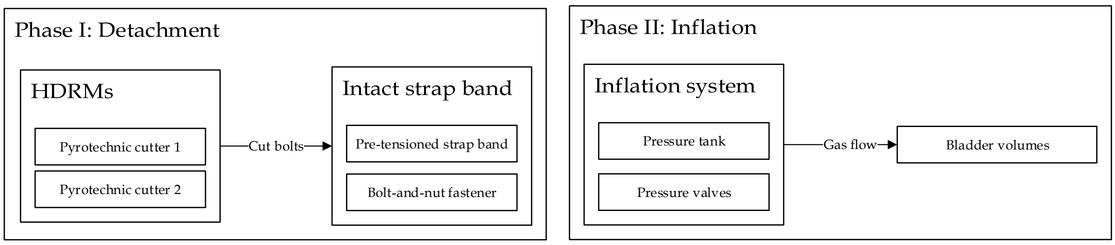

Figure 7.16: Schematic view of deployment sequence

7.3.3 Inflation system

The inflation gas is key to providing the structural stiffness for the inflatable: it is required to bring all members into tension to prevent skin wrinkling under compressive loading. To this end, the CIA will require an inflation system that is reliable, lightweight and fitting within mass and volume constraints. This section details the selection of an inflation gas and design of the inflation system upon which the CIA's deceleration capability hinges.

Gas generator selection Inflation systems can be categorised as tanked-gas systems, phase-change systems and chemical gas-generation systems [51]. These systems have each been considered for their respective advantages, yielding a tanked nitrogen inflation system as outcome.

Phase-change systems have the potential to provide significant mass reductions. The most promising option is a liquid hydrogen inflation system, while other phase-change systems involve subliming powders, although these are incapable of achieving high pressures [54].

[26]URL:`http://www.herberaircraft.com/pdf/117Cat/Clamps/AA33.PDF`. Accessed: 08-06-2015

On the basis of system mass fractions investigated by Brown et al. [39] and the mass estimation tool detailed in Section 6.1.5, a structural mass reduction of nearly 20 $[kg]$ is deemed feasible with a cryogenic liquid hydrogen inflation system following from the mass estimation tool formulated in Section 6.1.5.

This mass reduction comes at the expense of reliability, however. These systems involve a phase-change process, inherently unpredictable and thereby accompanied with reduced inflation system reliability [51]. In addition, cryogenic storage requires profound thermal control to keep it below its required temperature. While this poses a challenge for orbiting satellites, it is even more so an issue in the heated re-entry environment of the CIA. Reliability is further lessened by the absence of successful efforts in the past to accommodate a phase-change inflation system in spaceflight, let alone a high-pressure application like the CIA at hand. As reliability is key for transporting human payload, phase-change systems are deemed ill-suited. Moreover, a liquid hydrogen inflation system poses issues for safety when operating in the Earth atmosphere, in which flammability risk is present by the dual presence of hydrogen and oxygen in a heated environment. Re-entry on Earth should be considered for possible return missions of the CIA.

Chemical gas-generation systems similarly feature a higher level of complexity and thereby lower level of reliability than tanked-gas systems [51]. Moreover, while mass reductions are deemed feasible, these involve the use of hydrazine [51, 54]. Hydrazine poses issues with respect to cost and handling, but most importantly with respect to sustainability. As the decelerator will make contact with a hard surface, leakage of hydrazine into the Martian atmosphere and pollution of the landing site by its toxic nature poses a risk. This risk would violate COSPAR regulations and moreover limit the sustainable dimension of the mission.

Tanked-gas systems are the preferred choice, featuring a significantly higher level of reliability and past application. Most notably, these have seen application in the IRVE missions in the form of a nitrogen blow-down system [55]. Blow-down systems offer controllable gas flow at low development and hardware cost [54]. Moreover, these are excellently suited for high-pressure applications in inflatable structures [51].

Using helium rather than nitrogen would be infeasible. Due to the small size of helium atoms, permeability of the tank and inflatable becomes an issue and pressure leakage a more pronounced phenomenon. Moreover, helium application in spacecraft applications has remained under-investigated in literature and thereby poses significantly higher development risk.

Gas generator design and sizing A nitrogen tank is used for storage and supply of nitrogen gas. The minimum inflation pressure in the toroids is based on the premise that it should counteract the aerodynamic force exerted to bring flexible material into tension, formulated in Equation 11. The volume that is inflated may be approximated as the sum of the volumes of separate toroids summated over the entire sphere cone.

From the structural analysis it followed that a pressure of 169 $[kPa]$ over a total volume of 68 $[m^3]$ is required in the inflatable bladders. This minimum inflation pressure is smaller than that required in IRVE-3 [56], hence it induces smaller loads, which make up most of the flexible wall loading and the structural lay-up can consequently be thinner than in the case of IRVE-3. The inflation pressure brings all members into tension, as illustrated by Figures 7.10 and 7.11.

To account for pressure losses following from a drop in temperature, as observed in the IRVE-II mission [49], a heater is used to heat the tank after partial usage of the inflation gas. The total mass of the inflation gas can be estimated on the basis of the required operating pressure. From a functional perspective the minimum required inflation pressure should be reached at all phases of the deceleration. Thermal loading of the CIA will increase the temperature of the inflation gas and cause a proportional increase in pressure. Pressure increases above the minimum inflation pressure are beneficial as this will increase the stiffness of the CIA. This works up to some point as structural loading has to be taken into account as well. If the pressure increases to much venting may be performed to reduce the pressure, which will be further discussed in the subsequent paragraph. Pressure decreases below the minimum required pressure are however dangerous as the stiffness of the CIA will be lost.

For this reason a minimum operational temperature is considered. Figure 7.17 shows the temperature range in Kelvin for a cylindrical body sideways heated by the sun in an orbit around Mars. The temperature is based on heat flow equilibrium, not considering any of the atmospheric entry effects [8]. A range of absorptivity over emissivity values is considered. This value is dependent on the outer coating of the spacecraft and is an large extend left free to be chosen. Nevertheless a conservative value of 0.5 is chosen which yields a temperature of $202\,[K]$. Lower temperature increases are not envisioned for a threefold of reasons:

- The Martian atmospheric temperature ranges between 100 and $200\,[K]$, but conduction is low and only for the short period within the Martian atmosphere
- Solar radiation will still heat the entry vehicle
- Thermal loading will cause an increase in temperature even behind the heat shield of the inflatable.

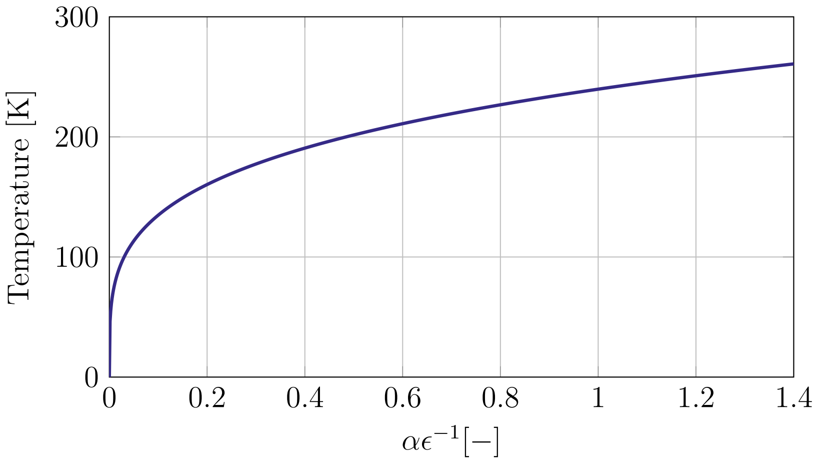

Figure 7.17: Temperature range for a cylinder at Mars as function of the absorptivity over emissivity

Using a temperature of $202\,[K]$ inside the inflatable yields a total gas mass of $90\,[kg]$ that is to be held within the pressure tank, given a molar mass of $22\,[g \cdot mole^{-1}]$ for nitrogen gas [40]. An additional contingency of 20% is included. This contingency accounts for leakage, which requires additional gas to make up for the lost volume, so called make up gas [51].

The ratio of tank and inflatable volume is obtained via the ideal gas law as:

$$\frac{V_{tank}}{V_{inflatable}} = \frac{P_{infl}T_{tank}}{P_{tank}T_{infl}} \tag{14}$$

Initial estimates for the tank pressure and temperature are 27.6 $[MPa]$ and 323 $[K]$ [8, p.545]. Based on the required pressure and a temperature of 202 $[K]$ in the inflatable, by use of the ideal gas law, a total pressure tank volume of 0.27 $[m^3]$ follows. Corresponding to this tank volume is a required tank mass, dependent on the material used. Composite-wrapped pressure vessels offer significant weight advantages with respect to metallic tanks and therefore such a pressure vessel is selected. Tank mass is estimated from empirical relations established by Zakrwski [8, p.546] to be 61 $[kg]$ for the selected tank pressure and volume via Equation 15.

$$m_{tank} = 0.7266 \cdot (P_{tank} \cdot V_{tank})^2 + 2.5119 \cdot (P_{tank} \cdot V_{tank}) + 2.9826 \tag{15}$$

Inflation system integration The inflation system is integrated in the entry vehicle via a number of valves, lines, pressure sensors and temperature sensors. Figure 7.18 shows a schematic representation of the inflation system. The inflation gas is stored in a nitrogen tank. Pressure and temperature sensors are included to monitor the storage conditions. A separate valve is included for filling purposes of the tank, and a release valve is included for emptying the tank outside normal mission operations. An electromechanical valve releases the pressure. An electromechanical valve is used since it allows for multiple uses as opposed to one-time use pyrotechnical valves, used in early IRVE instalments [22]. From the high pressure within the storage tank the controlled the pressure is reduced and more precisely controlled by a set of two pressure regulators (including internal release valves). One of the pressure regulators is located in the high-pressure part of the inflation system in the centre body, the other in the low-pressure part. Duality of pressure regulators accounts for flow adjustment while also taking into account feed losses. A set of check valves, allowing flow only in one direction, connects to the toroid. Purpose thereof is to prevent flow from exiting the bladder volumes.

The toroids are grouped together and inflated with separate bladder volumes. The number of bladder volumes is preferably higher to provide redundancy. A single bladder volume puncture or failure would then be less catastrophic, as part of its function can be taken over by other bladders. Increasing the number of bladder volumes does, however, add additional system complexity and mass. The IRVE missions feature three bladder volumes, taken as a reference number. The current mission features a significantly larger area, however, and since puncture probability is thereby increased due to the larger exposed surface area. To this end four inflatable bladder volumes are selected. The check valves prevent the flow from equilibrating over the toroids in this case.

A final set of check valves is included to connect the toroids to the vent. This allows for reducing the pressure in case it becomes to high. The conditions within the tank are measured by a set of pressure and temperature transducers. If the pressure becomes to high, for example due to the thermal heating, the vent functions to lower the pressure. Pressure transducer however are also important for making sure the minimum pressure is maintained since the pressure can drop due to leakage.

A contingency of 25% of tank mass is included to account for the blow-down system that transfers gas from the tank to the inflatable volumes. For a tank mass of 61 $[kg]$, total inflation system mass is 76 $[kg]$ to support a gas mass of 90 $[kg]$.

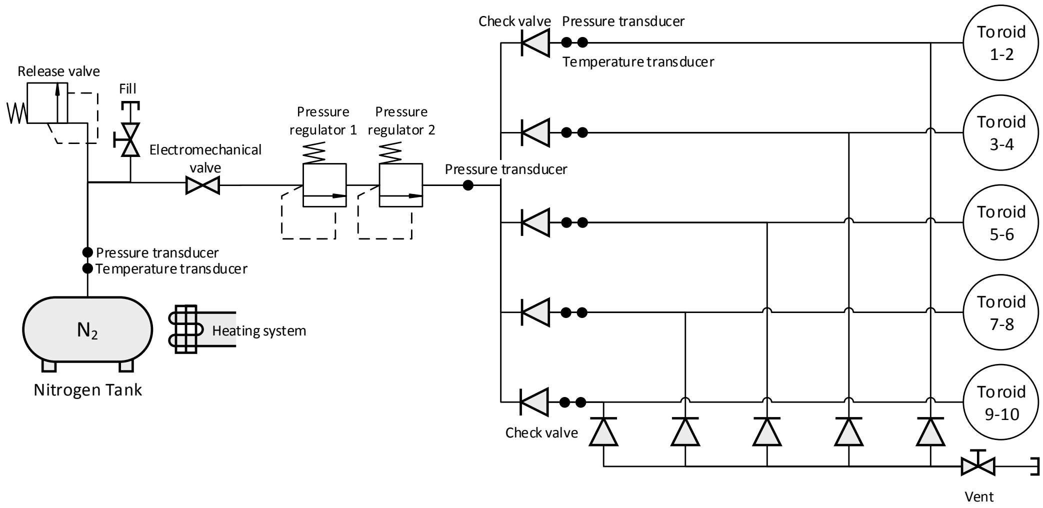

Figure 7.18: Schematic view of the inflation system

7.3.4 Control system

This section will discuss the control system selection procedure and control system design. First the control system downselect is discussed, after which the resultant control system is sized to the mission requirements.

Control actuation selection Based on the arguments for and against certain control actuation concepts given in Section 6.1.3, a selection of suitable control actuation solutions was made. Figure 7.19 shows the CG offset required along the z-axis to trim the spacecraft at certain angles of attack for various CG locations on the x-axis. From Figure 7.19 it

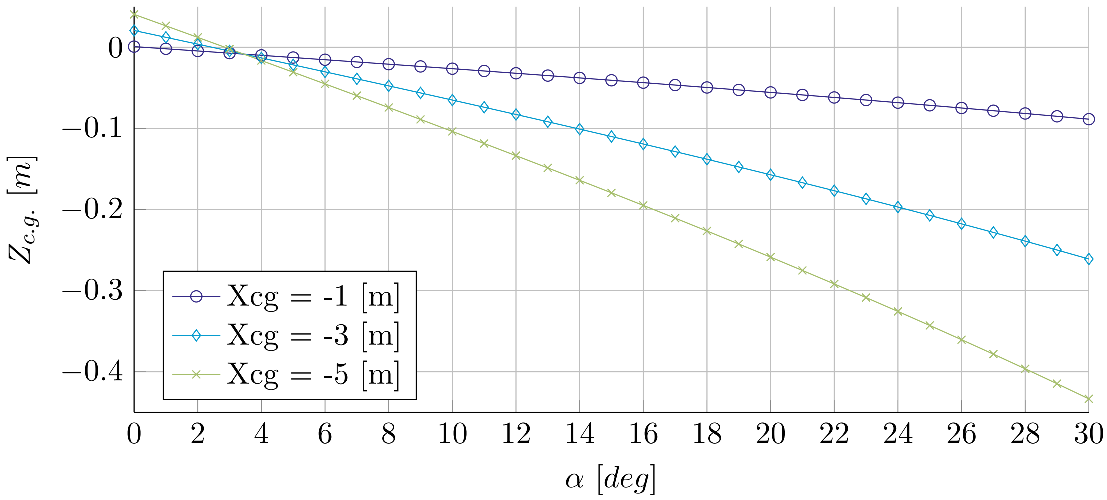

Figure 7.19: CG offset along x-axis required for a trimmed condition at various angles of attack

can be seen that the required CG z-offset grows as the x-offset grows. For an angle of attack change of 2 [deg] corresponding to an x-CG located at -5 [m] a CG shift of 0.2 [m]

is required. Angle of attack-based trajectory control was found to require trimmed α-shifts of $5\,[deg]$ that have to be adjusted with a rate of $1\,[deg \cdot s^{-1}]$. To pull this off would require the actuation system to produce a CG displacement of $0.5\,[m]$ with a required rate of $0.1\,[m \cdot s^{-1}]$. This would require excessively heavy actuators that would also have to be able to operate under $3g_e$ loads. Not only has this never been done before in space at such scale, the reliability of such a system would be questionable as a Single Point of Failure (SPF) would be introduced. Based on these arguments a decision was made against active CG control.

Following the decision to discontinue the consideration of active CG control a selection had to be made between the other two control actuation design options: Body flaps and thrusters. Regarding body flaps some of the same arguments can be made as were used against active CG control. Body flaps can require excessively large actuators that are very heavy. In addition to this the dynamic behaviour of the inflatable structure is difficult to compute and can be very unpredictable. Furthermore the use of body flaps on inflatable structures has a very low TRL, which poses an additional development risk. Based on these and other downsides pertaining to aerodynamic control surfaces mentioned in Section 6.1.3 thrusters are used as control actuators. These thrusters will be located on the edge of the crew capsule in order to maximise their moment arm without resorting to placing them on the inflatable structure.

Control actuation sizing and design The components of the control system providing the actuation can globally be subdivided into two components. The control system mass and its corresponding accuracy.

Mass estimates are based on the required propellant mass, thruster mass and fuel tank mass. The propellant mass can be subdivided into a further two categories: the control within the atmosphere and the control outside of the atmosphere. General equation were previously discussed within Section 6.1.3. An overview of the mass components and their respective masses is provided in Table 7.2.

Control within the atmosphere Within the Martian atmosphere control is performed on the basis of banking. A control system featuring a single bank control reversal manoeuvre is always able to arrive at the landing site with an average accuracy of $1.009\,[km]$ at Mars [57]. The control system accuracy can further be significantly reduced by using multiple bank reversals. Reductions are primarily found in the observed dispersions.

Accuracies using bank control where obtained using dispersions of ± 0.03 C_L, ± 0.06 C_D and mass and atmospheric dispersion of 5% and 30% respectively [57]. Accuracies of up to $10\,[m]$ can be achieved if the staging and final descent are included [36]. These control accuracies were obtained on the basis of sensed accelerations.

It is argued that with an increasing amount of bank reversals, complemented with additional control measures such as extra sensors, higher accuracies can be obtained. The trajectories are budgeted for a total of six bank reversals, three for both the initial aerocapture and the final EDL. Three bank reversals are typical values for single orbit [57, 58]. A very qualitative definition of three bank reversals as defined within the control system analysis is displayed in Figure 7.20.

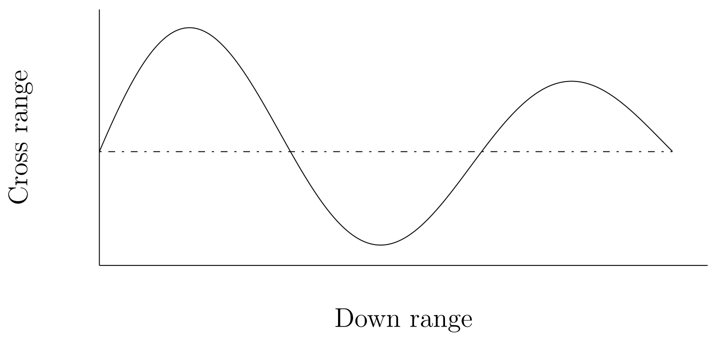

Figure 7.20: Qualitative figure displaying three bank reversals

The mass estimates of the propellant required within the Martian atmosphere are based on peak rotational rates of 20 $[deg \cdot s^{-1}]$ and 5 $[deg \cdot s^{-2}]$ as used by Davis et al. [36].

The inertial moments are based on a homogeneous mass distribution and a simplified geometric shape. The crew module is assumed to be a hollow cylinder with the structural components attached to the in- and outside of this cylinder. The inflatable structure is assumed to be of a circular disc shape, with a homogeneous mass distribution. Within this shape the mass is assumed to be primarily situated on the outside of the spacecraft such that a conservative mass estimates will be achieved.

Control outside the atmosphere Control outside of the Martian atmosphere is required for two purposes: clean-up corrections and orbit (de)-raising. The latter allows for a controlled entry time into the Martian atmosphere for the final EDL operations. The former makes sure that the desired parking orbit can be reached after the aerobraking.

For the purpose of orbit raising it is desired that the consequential orbit no longer covers the Martian atmosphere and that the orbital period fits within a Martian day. For practical purposes and considering the relatively short period in space (i.e. days) after the initial aerocapture the pericentre limit is set at 200 $[km]$.

Clean-up corrections are estimated based on results presented by Cianciolo et al. [58]. The most representative shapes are the 23 meter diameter HIAD and to a lesser extent the rigid aeroshell. On the basis of the former the clean-up velocity are estimated to be 10.47 $[m \cdot s^{-1}]$ (3σ) [58, p.37]. Note that Cianciolo et al. include the orbit raising within the clean-up estimates whereas here they are considered as two separate entities.

Thrusters Inertial moments combined with rotational rates deliver the required control moments via Equation 6. For the most efficient performance the thruster are placed on the outside of the crew module. Although thrusters placed on the outside of the inflatable are able to generate higher torques, multiple disadvantages hinder this placement:

- Thrusters placed on the inflatable will discommode stowage deployment.
- Deformation of the inflatable, and thus thruster performance, is difficult to predict.
- Placement of thrusters on the inflatable may induce undesired vibrations or aeroelastic effects.

Further details on the placement are also discussed in Section 5.2 discussing the packaging of the entry vehicle.

Thruster performance requirements are primarily based on the bank control speed. Apocentre velocity increments may take long but are however also greater in magnitude. The thrusters used for creating the bank control moments require a peak thrust of around $900\,[N]$. Torque is provided by multiple thrusters, thus equipped redundantly, such that other thrusters can take over its function if a thruster fails. Indicative values for a capable thruster are for example given by the MONARC-445 hydrazine mono-propellant thruster[27]. The MONARC-445 thruster delivers a nominal thrust of $445\,[N]$ at a mass of $1.6\,[kg]$. A configuration with eight of these thrusters allows for control around the roll axis and moreover provides partial control in the case of failure of one such thruster.

Specific preference lies in the use of hydrazine as propellant such that it is interchangeable with the remaining propellent requiring systems. The use of a single propellant allows for lower fuel fractions as propellants margins required for the different mission phases can be combined.

Additionally thrusters for the velocity increments in the apocentre are required. Again hydrazine thrusters are considered for interchangeability throughout the various mission phases. This is however combined with a second propellent as bi-propellant thrusters yield significant performance increases (in terms of I_{sp}) [8].

A thruster suitable for such a purpose is the Apogee kick engine by IHI Japan at a mass of $15.7\,[kg]$ and a specific impulse of $321.4\,[s]$. As secondary propellant Nitrogen Tetroxide (NTO) is required [8, p.538]. To ensure sufficient control system reliability two of these thrusters will be employed such that no SPF can occur.

Table 7.1: Overview of thruster properties [8, p.538]

Engine	**Manufacturer**	**Qt.**	**Mass [kg]**	**Length [m]**	**Propellants**	**Nominal Thrust [N]**	I_{sp} **[s]**
MONARC 445	MOOG	8	1.6	0.41	Hydrazine	445	235.0
Apogee kick engine	IHI Japan Company Ltd.	2	15.7	1.03	NTO/ Hydrazine	1700	321.4

Propellant tanks One of the main arguments for the use of hydrazine as the primary propellant is the ability to combine the propellant budgets for multiple mission phases as previously mentioned. This allows for a lower control system mass fractions as well as an equal control system reliability. Nevertheless a mass estimate for the propellant tank is provided to yield a fair mass estimate for the CIA design.

The tank mass is estimated via the empirical Equation 16 [8, p.543].

$$m_{tank} = 2.7086 \cdot 10^{-8} \cdot V^3 - 6.1703 \cdot 10^{-5} \cdot V^2 + 6.66290 \cdot 10^{-2} \cdot V + 1.3192 \qquad (16)$$

[27] URL: http://www.moog.com/literature/Space_Defense/Spacecraft/Propulsion/Monopropellant_Thrusters_Rev_0613.pdf Accessed: 15-06-2015

Component mass overview Table 7.2 provides an overview of the individual mass components discussed above. The propellant masses are given for the bank control, orbit clean-up and apocentre boost manoeuvres. Mass estimates exclude the final contingency factor of 20% applicable for all the CIA components.

Table 7.2: Control system mass components

Component	ΔV	**Mass [kg]**
Bank control	-	66
Clean-up	10.47	33
Orbit (de)raising	18.12	54
Fuel tank	-	12
Thrusters	-	44
Total	28.59	212

Control system method For achieving mission success it is essential that required accuracy can be obtained even under non-nominal conditions. For this purpose a control system is required such that the bank reversal angles and timing can be properly chosen allowing for a reference trajectory to be followed and ensuring mission success.

Similar to the mass estimates the control system can also be subdivided into part within and a part outside of the Martian atmosphere.

Control within the atmosphere Control within the atmosphere is required in two phases of the mission: the initial aerocapture phase and the final EDL. Due to small uncertainties in the CIA's performance, but more importantly due to atmospheric disturbances, deviations from the nominal trajectory can be observed. These deviations are accounted for in the trajectory discussed in Section 7.2 but also need to be recognised during mission operations such that they can be acted upon.

Typical implementations for a control system involve a Numerical Predictor-Corrector (NPC) or Analytical Predictor-Corrector (APC) method and use sensed accelerations to determine the atmospheric properties [36]. These values are used to update the control models such that the same terminal point is reached each time. For this purpose a set of three gyroscopes and three accelerators as Inertial Measurement Unit (IMU) is required [59]. The former is already included in the ADCS as discussed in Section 5.1.1. Recent advances in accelerometers make even the high-accuracy sensors a low mass component. The accelerometers are included in the ADCS mass budget as they are also required for the terminal descent phase.

For achieving the high required landing accuracy it is advised that next to sensed accelerations to determine the control model parameters pressure sensors are included. NPC and APC methods for bank control on Mars do normally not include these sensors and merely rely on sensed acceleration data [36, 57]. Since pressure can not be measured directly during the hypersonic flight, use is made of flush atmospheric data [59].

Such sensors are demonstrated in hypersonic flight in the Mars science laboratory in 2012 [59]. The use of separate sensors for determining the atmospheric properties will allow for easier determination of the atmospheric properties and allow for a higher landing accuracy in order to meet the set requirements. Pressure sensors are included in a redundant manner in the rigid section of the heat shield. This allows for a fault tolerant design [60].

A very schematic overview of the control system within the atmosphere is given in Figure 7.21. Conventional models update frequencies, using only sensed accelerations, are in the order of 10 seconds [36]. The usage of additional pressure sensors allow for more frequent model updates as changes are more easily observed, benefiting the accuracy of the control system.

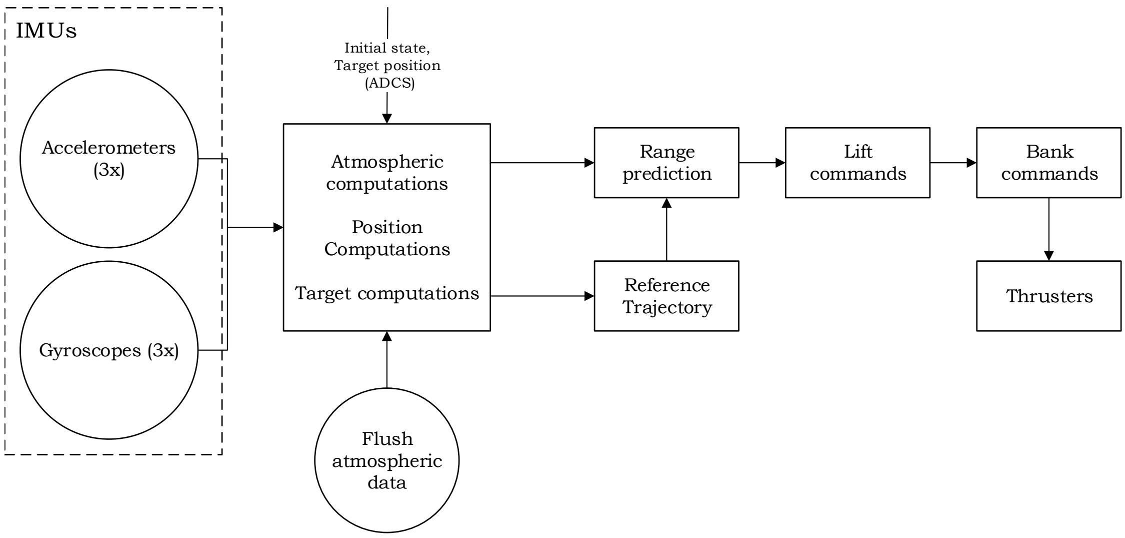

Figure 7.21: A schematic overview of the guidance system functioning

Control outside the atmosphere Outside the Martian atmosphere no additional sensors are required apart form those provided by the ADCS. The period outside the Martian atmosphere however serves as an aid for the final EDL. Unlike the initial aero-capture phase, for which no timing is possible, the period outside the Martian atmosphere in between the two entries allows for additional measurements and control model updates. Moreover the timing of the second re-entry in the Martian atmosphere can be controlled in intervals of single Martian days.

Controlling this entry allows for entries at favourable atmospheric conditions and reduces the risk of the mission. Atmospheric conditions can for example be transmitted via pre-existing base stations. Controlling the timing of the mission allows for much more certainty on the atmospheric conditions which is crucial for the precision of the re-entry. High variations in the atmospheric properties, such as may be the case due to dust storms, can thus be anticipated [61].

7.3.5 Crew module

The crew module has been designed to contain a crew of two during the mission duration of 89 days of interplanetary transfer and adjoining mission segments, comprising of launch and entry. To accommodate this, it requires the subsystems listed in Section 5.1 and it is packaged as described in Section 5.2.

7.4 Design summary

An overview of the design is provided in the following sections. The overview is provided in the form of performance and RAMS characteristics. It is concluded by a compliance matrix to ascertain that the design meets the requirements and close the iteration loop.

7.4.1 Performance characteristics

The mission starts at launch from Earth. A 10 000 $[kg]$ crew module carrying two crew members will be injected into an 89 day high energy transfer orbit to Mars, where it will arrive with a velocity of 7 $[km \cdot s^{-1}]$. Before entering the Martian atmosphere, a Nitrogen inflation system will deploy a stacked toroid inflatable heat shield. This heat shield will be supported by ten toroids made out of PBO Zylon® fibres and will feature a TPS consisting of a silicon carbide heat barrier protecting a Pyrogel® insulator. The vehicle will enter the Martian atmosphere twice. The first entry into the atmosphere will decelerate the vehicle to 4.53 $[km \cdot s^{-1}]$ to enter an elliptic orbit around Mars. At the apoareion of this orbit, the vehicle will perform an orbit raising burn to place itself in a parking orbit around Mars. Once final landing checks have been completed in orbit, the vehicle will perform a de-orbit burn and enter the atmosphere for landing. During both atmospheric manoeuvres, the vehicle will control its trajectory using bank angle adjustments. These adjustments allow the vehicle to ensure the terminal descent stage starts within 500 $[m]$ of its intended location. After landing using a retro propulsion system and carrying out the mission on Mars, the crew will return to Mars orbit using a pre-placed MAV and rendezvous with an ERV already waiting in orbit to take the crew back to Earth. The mission and design parameters are summarised in Tables 7.3 through 7.7.

Table 7.3: Global Mission parameters

Mission Duration	3.75 Years
Total Launches	2
Crew size	2
Time on Mars	2 Years
Estimated mission cost (including development)	44 Billion U.S Dollars

Table 7.4: Hypersonic decelerator parameters

Trajectory characteristics	
Aerocapture entry velocity	$7\,[km \cdot s^{-1}]$
Aerocapture exit velocity	$4.53\,[km \cdot s^{-1}]$
Aerocapture bank reversals	3
EDL entry velocity	$4.53\,[km \cdot s^{-1}]$
EDL bank reversals	3
Parking orbit period	$1\,[sol]$
Parking orbit apocentre altitude	$37\,300\,[km]$
Parking orbit pericentre altitude	$3590\,[km]$
Aerodynamic Characteristics	
Trim angle of attack	$22.5\,[deg]$
Trim CG offset	$0.5\,[m]$
Lift-to-drag ratio at trim	0.35
Drag coefficient at trim	1.3
Moment derivative w.r.t. α	-0.21
CIA outer diameter	$12\,[m]$
CIA height	$1.9\,[m]$
CIA lengthwise offset	$0.98\,[m]$
Structural characteristics	
Number of toroids	10
Toroid structural materials	PBO Zylon®, Upilex
Toroid gas barrier material	$0.050\,[mm]$
Toroid wall thickness (excluding TPS)	$0.125\,[mm]$
Toroid wall thickness (including TPS)	$3.121\,[mm]$
Thermal protection system characteristics	
Peak temperature	$1376\,[K]$
Heat barrier material	Nicalon™
Heat barrier thickness	$0.508\,[mm]$
Insulator material	Pyrogel® 6650
Insulator thickness	$2.438\,[mm]$

Table 7.5: Hypersonic decelerator mass breakdown

Hypersonic Decelerator	**Mass [kg]**
Structure	275
Thermal Protection System	255
Control System (including propellant)	212
Total excluding contingency	742
Total including contingency	928

Table 7.6: Crew module mass breakdown

Crew module	**Mass [kg]**
Power	280
ADCS	225
Thermal control	600
Structure	1300
Operational items	3140
Command & Data Handling	585
Crew	160
Terminal descent system	1445
Total	8550
Margin (5%)	450
Total including contingency	9000

Table 7.7: Propellant mass breakdown

Manoeuvre	**Mass [kg]**
Momentum unloading	20
Orbit clean up	33
Atmospheric control	54
Parking orbit/de-orbit	54
Landing	930
Total	1091

7.4.2 RAMS characteristics

RAMS characteristics are established to address the safety critical functions, redundancy philosophy and expected reliability, availability and maintainability. The four aspects RAMS are discussed hereafter.

Reliability It is key that the system is reliable and thereby the philosophy is that redundant equipment is warranted as long as it is within the mass budgets. To this end, for example inflation and propellant tanks are not redundantly equipped because of the significant mass increase effected thereby. Failure modes of profound impact on the mission have been taken up in Table 7.8. These failure modes give an indication of design reliability and therefore serve as a basis for further design efforts to maximise concept reliability.

On the basis of the failure modes specific to the inflatable design, it can be concluded that it is inherently more susceptible to mechanical failures than conventional rigid (re-)entry vehicles. While inflatables offers a significant decelerator mass decrease and achieve what is incapable of achieving with rigid solutions, reliability is penalised. Part of this increased failure probability is mitigated by increased safety margins in component selection and sizing for reliability.

Availability Availability is dominated by the launch window to Mars rather than production time for entry vehicles. The launch window occurs once every two years, in excess of production time, hence availability is limited.

Maintainability Maintainability of the vehicles is limited to the on-board operations to be performed by the crew. A fail-safe and safe-life approach to design will reduce scheduled maintenance operations to zero within the 100-day time interval of the mission. Any maintenance operations will be incidental and repair limited to crew capability. To this end, the crew module shall allow for (limited) accessibility of critical parts, like the inflation system, such that crew members can take appropriate actions in case of incidental component failure.

Safety Safety is the consequence of reliability, by a highly limited maintainability dimension to the RAMS analysis. As such, the system is roughly as safe as it is reliable: room for failure is limited to the redundancy applied in the system. (Re)-entry missions have demonstrated themselves inherently risky. The Space Shuttle is the most prominent example, with 2 out of 135 missions being a failure and the projected failure rate 1 out of a 100 flights[28].

[28]URL: `http://66.14.166.45/whitepapers/firewalls/ranum/Personal%20Observations%20on%20the%20Reliability%20of%20the%20Space%20Shuttle%20-%20Feynman.pdf`. Accessed:19-06-2015

Table 7.8: Overview of entry vehicle failure modes

#	Failure mode	Effect of failure mode
01	Bladder puncture	Loss of structural rigidity by decreased internal pressure, leading to loss of aerodynamic surface area and deceleration capability
02	Tank leakage	Insufficient pressure in blowdown high-pressure system. Leads to inability to inflate toroids if pressure drops too much and thereby to loss of structural rigidity and deceleration capability
03	Seam failure	De-attachment of inflatable flexible material leads to an unpreserved aerodynamic shape and a loss of deceleration capability
04	Bladder burst	Breaks up structural shape, leading to loss of aerodynamic surface area and deceleration capability
05	Faulty inflatable deployment (strap band or valve failure)	Inflatable cannot enter its deployed configuration, leading to loss of aerodynamic surface area and deceleration capability
06	Sensor misreading	Introduces faulty attitude information leading to a loss of control accuracy
07	Severe environmental conditions (e.g. dust storm)	Induces deviations from nominal trajectory and potentially significantly higher mechanical and aero-thermal loading in excess of (ultimate) sizing loads, causing potential vehicle failure
08	Computer failure	Switch to safe-mode computer; if both fail vehicle command is lost
10	Apocentre boost thruster failure	Inability to enter parking orbit, potentially entering hazardous Martian weather conditions
11	Retro-propulsion thruster failure	Loss of halting force in terminal descent phase resulting in a hard landing
13	Solar panel failure	Loss of power-generating capability and inability to support on-board systems for a prolonged period
14	Life support failure	Inability to support on-board crew, causing mission failure

7.4.3 Requirement compliance matrix

Table 7.9 and 7.10 present the compliance matrix for the top level mission and vehicle requirements. One can note that all requirements are met. For some of the requirements however no explicit values can be named. Nevertheless all required can be argued to be met. This argumentations is provided in the paragraphs below. A full argumentation is provided within the respective chapters and sections of this report.

Table 7.9: Mission requirements compliance matrix

ID	Description	
CIA-M01	The entry vehicle shall decelerate from a velocity of $7\,[km \cdot s^{-1}]$ at $400\,[km]$	✓
CIA-M02	The entry vehicle shall not exert an acceleration greater than $29.4\,[m \cdot s^{-2}]$ on any crew member for the duration of the mission	✓[29]
CIA-M03	The entry vehicle shall attain reach Mach $5\,[-]$ at an altitude of 15 000 $[m]$ MOLA	✓
CIA-M04	The entry vehicle shall reach its final position with a precision of $500\,[m]$	✓
CIA-M05	The entry vehicle shall attain its final velocity within 10 days after entering the Martian atmosphere	✓

Table 7.10: Entry vehicle requirements compliance matrix

ID	Description	Value	
CIA-R01	The entry vehicle shall have an undeployed diameter smaller than $5\,[m]$	4.5-5.0 $[m]$	✓
CIA-R02	The entry vehicle shall have a deployed diameter smaller than $12\,[m]$	$12\,[m]$	✓
CIA-R03	The entry vehicle shall have a mass of 10 000 $[kg]$ at the start of the entry	10 000 $[kg]$	✓
CIA-R04	The hypersonic decelerator shall have a mass fraction of no greater than 10% of the vehicle mass	$928\,[kg]$	✓
CIA-R05	The entry vehicle shall adhere to the COSPAR regulations	-	✓
CIA-R06	The entry vehicle shall have control system reliability of at least 0.9995	-	✓/✗

[29] Under non-nominal trajectories temporarily higher loads may be experienced

Mission requirements

CIA-M01 The entry vehicle has been sized for an entry velocity of 7 $[km \cdot s^{-1}]$ at 400 $[km]$ and final Mach number of 5 at an altitude of 15 $[km]$. No adjustments were required to these values to meet the other requirements and as such these values has been adhered to.

CIA-M02 The trajectories have been sized for peak accelerations of 29.4 $[m \cdot s^{-2}]$. For a nominal trajectory this value is not exceeded. Under non-nominal conditions slightly higher accelerations may be observed (up to +7 $[m \cdot s^{-2}]$).

CIA-M03 The trajectories have been sized for achieving Mach 5 $[-]$ at an altitude of 15 000 $[m]$ under both nominal and non-nominal conditions.

CIA-M04 Using bank control, if all state variables are known, the required control accuracy can be achieved under nominal and non-nominal trajectory conditions. Discrepancy in the final position follow from estimation of state variables. Bank control using only sensed accelerations may not deliver this accuracy under non-nominal conditions. However, the addition of additional pressure sensors can improve this accuracy which is also further discussed in Section 7.3.4. Taking this into account the required accuracy can probably be achieved under non-nominal conditions as well.

CIA-M05 The initial entry into the Martian atmosphere is timed at around 800 seconds as well as the final EDL. A parking orbit in multiples of single Martian days in between the aerobraking and final EDL extends the total mission duration. At least one full orbit is required, but this can be extended further for more favourable atmospheric conditions. As such nine additional windows entries are possible within the ten day limit. This is also further discussed in Section 7.2.

Entry vehicle requirements

CIA-R01 Special care has been taken that the deployed diameter remains below the 5 $[m]$ limit. As such the undeployed outer diameter was constraint to 4.5 $[m]$. The sole exception hereupon is the inflatable structure with the accompanying hold down and release system. This will add slightly in diameter but is merely constraint by how tight the inflatable is folded. This should fit easily within the 0.25 $[m]$ remaining margin on either side considering the thinness of the inflatable structure.

CIA-R02 The outer diameter is sized at 12 $[m]$. No additional components will extend this size in the future as it is merely the size of the inflated structure.

CIA-R03 The structure has been sized with total mass of 10 000 $[kg]$. A crew module analysis discussed in Chapter 5 showed feasibility for such a design with crew count of two.

CIA-R04 The decelerator mass is sized at 928 $[kg]$. This value includes a 20% contingency factor applicable for this phase of the design. As such feasibility of the CIA design within the 1000 $[kg]$ limit is deemed possible.

CIA-R05 The COSPAR regulations have been taken into account in the entry vehicle and mission design where applicable.

CIA-R06 The control system reliability has not been explicitly computed as a value. However, the focus was on reliable design throughout the various design phases. Bank control using thrusters is applied commonly, and thrusters feature a relatively high reliability as compared to more unproven technologies. Moreover redundancies have been used where possible such that possible SPF's are prevented.

8 Recommendations for future work

The mission design requires further design on one hand and testing and design verification and validation on the other hand. To this end, this chapter presents key issues for design improvement in Section 8.1, future work activities in Section 8.2 and verification and validation activities are discussed in more detail in Section 8.3.

8.1 Design improvement

While the CIA offers prominent weight and packaging advantages with respect to conventional rigid solutions, it is inherently more unreliable. The failure modes in Table 7.8 and the risk map in Table 4.1 indicate that risk mitigating actions are to be taken in:

- Deployment
- Inflation
- Terminal descent
- Nicalon^{TM} application in TPS
- Asymmetrically stacked toroids

Prominent design recommendations are therefore an increase in reliability by addressing these issues. For the deployment and terminal descent phases, it is recommended that a trade-off for available methods is performed to yield the most reliable method within mass constraints. For the inflation system, it is recommended that in design of the blow-down system reliability is key. For the application of Nicalon^{TM}, extensive testing is required to ascertain its suitability for application in the CIA. Finally the structural and aero-elastic effects of stacking the toroids asymmetrical needs to be investigated and tested as this can prove to be a high risk factor.

8.2 Project design and development logic

Key steps to be taken for manned missions to Mars for the proposed design are:

- Crew module design and decelerator detailed design
- Ground and unmanned flight testing to further design and component TRL
- Production and integration
- Crew preparation and training
- Establishing infrastructure on Mars

8.2.1 Project Gantt chart

Having finished this preliminary investigation, careful consideration is required on the planning of the rest of the design, production and operation phases. A Gantt chart of the steps following this preliminary investigation is presented in Figure 8.1.

Development times are based on representative missions [8]. Testing requires a considerable amount of time, due to the human-rated nature of the final spacecraft. Acceptance testing is done using a cargo mission, demonstrating the compliance of the spacecraft with the requirements on Mars. After that, potential required cargo missions are flown, including the ERV.

ID	Task Name	Duration	Start	Finish
2	Preliminary design	365 days	Tue 01-09-15	Thu 10-11-16
1	Detailed design	712 days	Fri 11-11-16	Tue 23-10-18
7	Production	712 days	Sat 07-04-18	Wed 18-03-20
10	Testing	3650 days	Mon 05-11-18	Wed 01-11-28
9	Launch of test/cargo mission	0 days	Fri 26-07-24	Fri 26-07-24
8	Launch of cargo missions	0 days	Mon 14-09-26	Mon 14-09-26
13	Crew training	712 days	Sat 21-11-26	Wed 01-11-28
11	Launch preparation	85 days	Thu 02-11-28	Thu 25-01-29
12	Launch	1 day	Fri 26-01-29	Fri 26-01-29
4	Interplanetary transfer	89 days	Sat 27-01-29	Wed 25-04-29
3	Aerocapture and landing	1 day	Thu 26-04-29	Thu 26-04-29
5	Mission on Mars	712 days	Fri 27-04-29	Tue 08-04-31
6	Return to Earth	89 days	Wed 09-04-31	Sun 06-07-31

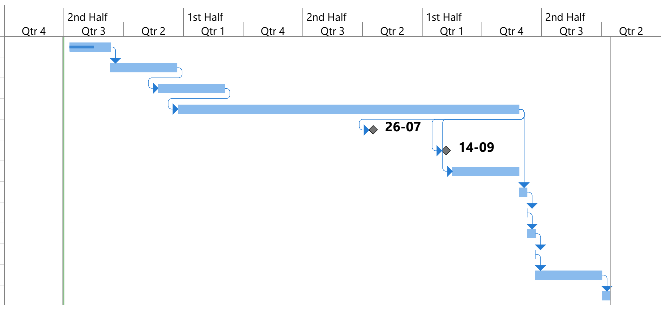

Figure 8.1: Gantt chart of future project activities

8.2.2 Future design activities

The crew module is to be designed. This involves the subsystems as defined in Chapter 5, the crew cabin lay-out and the packaging of the subsystems as outlined in Section 5.2. Moreover, the decelerator requires further detailed design to fully establish its configuration and ready it for production and integration.

8.2.3 Testing activities

Table 8.1 gives an overview of proposed testing activities. In addition, it outlines the articles on which these are performed and the purpose of the tests.

8.2.4 Production and integration

Production and integration of the vehicle commences by a definition and analysis of the most cost-effective manufacturing methods and the most reliable and cost-effective joining methods. Hereafter, production and integration proceed in dedicated facilities with a dedicated work crew to take full advantage of crew experience and learning effect. In view of sustainability, non-value-adding activities are to be minimised in conformance with the lean manufacturing principle.

8.2.5 Crew preparation

Crew members are to be trained and prepared for the 89-day journey and ensuing entry, during which they are exposed to high g-loads. Selection, training and preparation of crew members shall include their physical fitness, capability to perform required on-board activities and mental state for their isolatory condition.

8.2.6 Establishment of a Martian infrastructure

It is proposed that the entry vehicle is first flown unmanned, in the acceptance testing, to Mars to carry cargo required to establish an infrastructure. In addition, an infrastructure shall be laid out on Mars by previous missions. To this end, the required facilities on Mars are to be inventoried, packaged and sent as cargo on these missions.

Table 8.1: An overview of proposed testing activities

Testing activity	Performed on	Purpose
Wind tunnel testing	Scaled decelerator wind tunnel	1) Estimate aerodynamic properties 2) Investigate effect of structure flexibility 3) Investigate aerodynamic phenomena (e.g. aero-elasticity)
Aero-thermal testing	- TPS lay-up samples - Decelerator assembly - Crew module	1) Demonstrate heat-carrying capability and temperature 2) Internal heat transfer (e.g. to structural layers and inflation
Structural testing	- PBO Zylon® samples - Decelerator assembly - Crew module	1) Demonstrate load-carrying capability 2) Investigate decelerator deflection 3) Estimate effect of temperature on mechanical properties 4) Determine effect of (launch) vibrations
Deployment system testing	- Strap-band assembly - Centre body release - Decelerator assembly	Investigate reliability of deployment
End-to-End information system testing	Avionics (C&DH, ADCS and telecommunications)	Ascertain compatibility of data handling systems
Flight testing (Earth)	Prototype scaled-down model (unmanned)	1) Determine control system performance 2) Determine scaled-down vehicle performance 3) Validate analysis models
Flight testing (Earth)	Prototype full-scale model (unmanned)	1) Validate scalability of design 2) Determine integrated vehicle performance
Mission scenario testing (simulation)	Avionics (C&DH, ADCS and telecommunications)	Demonstrate that flight hardware and software can execute the mission in terms of data flow with no time constraints
Operations readiness testing (simulation)	Avionics (C&DH, ADCS and telecommunications)	Demonstrate that flight hardware and software can execute the mission in terms of data flow with real timeline
Acceptance testing (Mars)	Flight full-scale model (unmanned)	Demonstrate system performance under limit loads
Pilot training (simulation)	Crew members	Investigate man-machine interaction during interplanetary flight and entry

8.3 Verification and validation activities

System verification and validation will need to be carried out as the project progresses. An outline of future verification and validation procedures is given in this section. This outline can be used to develop the verification and validation procedures as the project progresses.

8.3.1 Requirement verification

Although compliance to all top level requirements has been shown in Section 7.4.3, further verification will be needed as the design progresses and higher fidelity analysis have been performed.

Mission requirements The mission requirements can be verified by analysis. A high fidelity model of the re entry must be created. This model will require validated aerodynamic, thermodynamic and inertial properties of the final design. This data can be obtained using a mix of computational models and physical tests. It will also require the control logic that will be used during the re entry to be implemented in the trajectory model. This high fidelity model is then used to demonstrate that the proposed design is capable of fulfilling all mission requirements under all reasonable circumstances.

Entry vehicle requirements Entry vehicle requirements can be verified by inspection. Design documentation will provide all the relevant dimensions, procedures and masses to be able to prove that all entry vehicle requirements are met. Despite this, the total vehicle mass should also be verified using the final product to ensure full compliance to launch constraints. It must also be verified that all COSPAR adherence procedures have actually been followed throughout the production of the vehicle.

8.3.2 Product validation

Product validation will be performed by physical testing of part scale and full scale models. These tests have already been mentioned in Section 8.2.3. The tests relating to the complete, integrated product will be expanded on in this section.

Deployment tests It must be demonstrated that the inflatable will deploy under representative conditions. Several critical tests must be passed before the system can be cleared for flight testing and eventually operational status. The first test of the deployment system must demonstrate that the deployment can be achieved without damaging the spacecraft or the inflatable. This is followed by deployment tests under vacuum conditions. The vacuum tests will also be used to validate the expected loss in pressure over time. Several tests will be needed to validate the performance of the deployment system under adverse conditions or malfunctions such as pyro-cutter misfires and incorrect stowage. The final deployment tests will take place during early flight testing. These will validate the ability of the inflatable to deploy under zero-g conditions.

Scaled flight testing After the performance of the deployment mechanism has been validated, scaled flight testing will take place. These tests will focus on the performance of the control system and should prove that the control systems are capable of accurate trajectory control. They will also be used for further refinement and validation of the aerodynamic, thermodynamic and flight control models. The scaled tests will use sounding rockets for suborbital test flights.

Full system flight testing The final validation tests will consist of three stages. After these tests, the performance of the system will have been completely validated and the system will be ready for human missions to Mars. The first stage consists of orbital re-entries of the full scale system. This will prove the system is capable of accurately entering the atmosphere of a planet from orbit for re-entry. The second stage will send the full system on a trip around the moon, and re-enter the Earth's atmosphere using a mission profile comparable to what will be used on Mars (i.e. aerocapture followed by aerobraking). The final test of the system will be to land the cargo required for the mission on Mars. This final landing will prove that the system is ready for operational use.

9 Conclusion

Scientific and commercial interest in extraterrestrial human exploration and habitation call for a feasible and efficient solution to entry. An inflatable aeroshell offers significantly lower mass and higher packaging efficiency than conventional, rigid solutions. Whereas rigid decelerator mass is estimated at over $3000\,[kg]$, preliminary design has yielded a guidable inflatable stacked toroid decelerator of a mere $1000\,[kg]$, capable of bringing two crew members in a $9000\,[kg]$ capsule to Mars.

Aerodynamic deceleration is performed by two passes through the atmosphere: aerocapture, intermitted by a parking orbit, followed by entry. This sequence, taking place in 1 Mars day, and decelerates the vehicle from a $7\,[km \cdot s^{-1}]$ upon entry of the atmosphere to Mach 5 at $15\,[km]$ altitude while keeping crew member loading under $3g_e$. Trajectory adherence and control is provided by bank control, effected by reaction control thrusters and control system estimated at $212\,[kg]$.

A key feature of the CIA design is a skewed shape. The asymmetry follows from aerodynamic optimisation and yields higher lift-generating capability at lower angles of attack to firstly achieve more lift and secondly require smaller angles of attack to keep the crew module from being impinged by the flow. Aerodynamic performance is characterised by a 0.35 lift-to-drag ratio and a $22.5\,[deg]$ trim angle of attack.

The asymmetry is adopted by the structural shape through stitching of ten inflatable toroids at a variable half-cone angle with respect to one another. Structural rigidity under an ultimate aerodynamic pressure of $3500\,[Pa]$ is ensured by the use of a nitrogen blow-down system that inflates five bladder volumes at $169\,[kPa]$, which keeps the flexible bladder material in tension to prevent compressive wrinkling. Resulting loads are carried by woven PBO Zylon® fibres of $0.125\,[mm]$ thickness at a $95\,[kg]$ mass. At a minimum half-cone angle, structural mass is estimated at $300\,[kg]$.

The Thermal Protection System is exposed to a peak heat flux of $21\,[W \cdot cm^{-2}]$ and a peak temperature of $1376\,[K]$ during aerocapture. This thermal loading is withstood by a multi-material lay-up $256\,[kg]$ consisting of a state-of-the-art Nicalon™ (also called Hi-Nicalon™) barrier of $0.51\,[mm]$ thickness and Pyrogel® 6650 insulator of $2.4\,[mm]$ thickness, complemented by dual $25\,[\mu m]$ Kapton gas barriers.

Compatibility of the CIA with a manned Mars mission is ascertained by preliminary crew module and mission design. The crew module accommodates two crew members for an 89-day journey to Mars and its mass is estimated at $9000\,[kg]$. Return from Mars requires an additional launch prior to crew module launch, during which the Mars Ascent Vehicle and an Earth Return Vehicle are brought onto Mars and in an orbit around Mars respectively. Mission cost including development is estimated at 44 billion US dollars.

Recommendations are a propagation of design on decelerator and crew module, testing activities and crew and mission preparation thereafter. Key driver for further design is concept reliability. Deployment, inflation and terminal descent are critical mission phases and inherently unreliable for an inflatable aeroshell design. These therefore require particular attention in future design.

References

[1] J. A. D. Corso, W. E. Bruce, K. A. Liles, and S. J. Hughes, "Thermal Analysis and Testing of Candidate Materials for PAIDAE Inflatable Aeroshell," *AIAA*, no. May, pp. 1–17, 2009.

[2] J. D. Corso, F. Cheatwood, W. Bruce, and Others, "Advanced High-Temperature Flexible TPS for Inflatable Aerodynamic Decelerators," *21st AIAA Aerodynamic Decelerator Systems Technology Conference and Seminar*, pp. 1–23, 2011.

[3] DuPont, "KEVLAR Aramid Fiber: Technical Guide," 2011.

[4] B. P. Smith, I. G. Clark, and R. D. Braun, "Thermal, structural, and inflation modeling of an isotensoid supersonic inflatable aerodynamic decelerator," in *IEEE Aerospace Conference Proceedings*, (Big Sky, MT), 2011.

[5] A. R. Nye, *Ceramic Matrix Composite Characterization Under a.* PhD thesis.

[6] S. Zinkle and L. Snead, "Thermophysical and Mechanical Properties of SiC/SiC Composites," *Journal of Nuclear Materials*, 1998.

[7] L. George and L. Kos, "Interplanetary Mission Design Handbook : Earth-to-Mars Mission Opportunities and Mars-to-Earth Return Opportunities 2009 2024," tech. rep., NASA, 1998.

[8] J. R. Wertz, D. F. Everett, and J. J. Puschell, *Space Mission Engineering: The New SMAD.* Hawthorne: Microcosm Press, first ed., 2011.

[9] National Aeronautics and Space Administration, "Space Launch System (SLS) Program Mission Planner's Guide (MPG) Executive Overview," tech. rep., NASA, 2014.

[10] A. Korzun and R. Braun, "Performance Characterization of Supersonic Retropropulsion for Application to High Mass Mars Entry, Descent, and Landing," in *AIAA Atmospheric Flight Mechanics Conference*, pp. 1–29, 2009.

[11] R. D. Braun and R. M. Manning, "Mars Exploration Entry, Descent, and Landing Challenges," *Journal of Spacecraft and Rockets*, vol. 44, no. 2, pp. 310–323, 2007.

[12] M. S. Anderson, H. L. Bohon, and M. M. Mikalas, "A Structural Merit Function For Aerodynamic Decelerators," Tech. Rep. November, NASA, Washington, D.C., 1969.

[13] S. J. Hoffman and D. I. Kaplan, "Human Exploration of Mars : NASA Mars Exploration," tech. rep., NASA, Houston, Texas, 1997.

[14] M. Warhaut, P. Ferri, and E. Montagnon, "Rosetta ground segment and mission operations," *Space Science Reviews*, vol. 128, no. 1-4, pp. 189–204, 2007.

[15] C. D. Edwards, C. T. Stelzried, L. J. Deutsch, and Others, "NASA's Deep Space Telecommunications Roadmap," tech. rep., NASA, Pasadena, California, 1999.

[16] R. Labelle and D. Rochblatt, "Ka-band high-rate telemetry system upgrade for the NASA deep space network," *Acta Astronautica*, vol. 70, pp. 58–68, 2012.

[17] NASA, "Fiscal Year 2013 President's Budget Request Summary," 2014.

[18] M. H. Masud, M. Akhtaruzzaman, M. S. Bari, and A. Farhat, "Engineers' Obligations towards Sustainable Environment," in *2nd International Conference on Engineering Professional Ethics and Education*, (Kuala Lumpur), International Islamic University Malaysia, 2011.

[19] S. Balasooriyan, B. van Dongen, D. Hage, and Others, "Design Synthesis Exercise Design of a Controllable Inflatable Aeroshell Mid-Term Report," Tech. Rep. 01, Delft University of Technology, Delft, 2015.

[20] United Nations, "United Nations Treaties and Principles on Outer Space," 2008.

[21] M. Crawford, J. Church, and B. Akin, "CPI Detailed Report," Tech. Rep. May, United States Bureau of Labor Statistics, 2015.

[22] S. J. Hughes, R. A. Dillman, B. R. Starr, and Others, "Inflatable Re-entry Vehicle Experiment (IRVE) Design Overview," in *18th AIAA Aerodynamic Decelerator Systems Technology Conference and Seminar*, AIAA, 2005.

[23] National Aeronautics and Space Administration, "NASA systems engineering handbook," tech. rep., NASA, Washington, D.C., 2007.

[24] Carl Christian Liebe, "Star trackers for attitude determination.," *Aerospace and Electronic Systems Magazine, IEEE (Volume:10 , Issue: 6)*, no. June, pp. 10 – 16, 1995.

[25] T.-h. You, E. Graat, A. Halsell, and Others, "Mars Reconnaissance Orbiter Interplanetary Cruise Navigation ," in *20th International Symposium on Space Flight Dynamics*, pp. 1–16, 2007.

[26] G. W. Eger, "Orion s Command and Data Handling Architecture," in *AIAA Space 2008 COnference & Exposition*, no. September, (San Diego, California), AIAA, 2008.

[27] J. Taylor, D. K. Lee, and S. Shambayati, "Mars Reconnaissance Orbiter Telecommunications," *Deep Space Communications and Navigation Series*, vol. 12, 2006.

[28] D. a. Tito, G. Anderson, J. P. Carrico, and Others, "Feasibility analysis for a manned mars free-return mission in 2018," *IEEE Aerospace Conference Proceedings*, pp. 1–18, 2013.

[29] M. Rudisill, R. Howard, B. Griffin, and Others, "Lunar Architecture Team - Phase 2 Habitat Volume Estimation : Caution When Using Analogs ," in *Earth and Space Conference 2008*, (Long Beach), NASA Langley Research Center, 2008.

[30] J. J. Ainsworth, E. A. Gustafson, and C. S. Collier, "Design and Analysis of Alternative Structural Concepts for the Orion Heat Shield Carrier Structure," tech. rep., Collier Research Corp, Newport News, 2014.

[31] R. D. Karam, *Satellite Thermal Control for Systems Engineers.* Reston, Virginia: American Institute of Aeronautics and Astronautics, 1st ed., 1998.

[32] J. D. Anderson Jr., *Hypersonic and High-Temperature Gas Dynamics.* AIAA, 2nd ed., 2006.

[33] M. E. Tauber, G. P. Menees, and H. G. Adelman, "Aerothermodynamics of transatmospheric vehicles," in *AIAA/ASME 4th Joint Thermophysics and Heat Transfer Conference*, (Boston, Massachusetts), AIAA, 1986.

[34] J. A. Mulqueen, "Applications of low lift to drag ratio aerobrakes using angle of attack variation for control," Tech. Rep. June, George C. Marshall Space Flight Center, Marshall Space Flight Center, Alabama, 1991.

[35] N. Allen, *AIAA Aerospace Design Engineers Guide.* Reston, Virginia: American Institute of Aeronautics and Astronautics, Inc., sixth ed., 2012.

[36] J. L. Davis, A. D. Cianciolo, R. W. Powell, and Others, "Guidance and Control Algorithms for the Mars Entry, Descent and Landing Systems Analysis," in *AIAA/AAS Astrodynamics Specialist Conference*, (Toronto), AIAA, 2010.

[37] J. P. Holman, *Heat Transfer.* New York: McGraw-Hill, 9th ed., 2002.

[38] M. C. Lindell, S. J. Hughes, M. Dixon, and C. E. Willey, "Structural Analysis and Testing of the Inflatable Re-entry Vehicle Experiment (IRVE)," in *47th AIAA/ASME/ASCE/AHS/ASC Structures, Structural Dynamics and Materials Conference*, vol. 1699, AIAA, 2006.

[39] G. Brown, "Estimating Minimum Inflation Pressure for Inflatable Aerodynamic Decelerators," in *20th AIAA Aerodynamic Decelerator Systems Technology Conference and Seminar*, (Seattle), AIAA, 2009.

[40] J. A. Samareh, "Estimating Mass of Inflatable Aerodynamic Decelerators Using Dimensionless Parameters," tech. rep., NASA Langley, 2011.

[41] T. Megson, *Aircraft Structures for Engineering Students.* Oxford: Elsevier, 5th ed., 2012.

[42] R. A. Dillman, V. T. Gsell, and E. L. Bowden, "Attitude Control Performance Of IRVE-3," in *36th American Astronautical Society meeting*, NASA, 2013.

[43] S. R. Lewis, F. Foget, and E. Millour, "Mars climate database v5.2 detailed design document," Tech. Rep. February, ESTEC, 2015.

[44] NASA, "Structural Design and Test Factors of Safety for Spaceflight Hardware," 2014.

[45] D. K. Litton, D. M. Bose, F. M. Cheatwood, and Others, "Inflatable Re-entry Vehicle Experiment (IRVE-4) Overview," tech. rep., NASA, 2011.

[46] J. M. Pereira and D. M. Revilock, "FAA Development Of Reliable Modeling Methodologies For Fan Blade Out Containment Analysis Part 2 : Ballistic Impact Testing," *Journal of Aerospace Engineering*, vol. 22, no. July, pp. 240–248, 2009.

[47] R. Dillman, S. Hughes, J. Dinonno, and Others, "Planned Flight Of The Terrestrial Hiad Orbital Reentry (THOR)," tech. rep., NASA, 2014.

[48] S. Hughes, F. Cheatwood, R. Dillman, and Others, "Hypersonic Inflatable Aerodynamic Decelerator (HIAD)Technology Development Overview," in *21st AIAA Aerodynamic Decelerator Systems Technology Conference and Seminar*, (Dublin), AIAA, 2011.

[49] R. A. Dillman, S. J. Hughes, and R. J. Bodkin, "Flight Performance of the Inflatable Reentry Vehicle Experiment 3," in *International Planetary Probe Workshop*, (San Jose, California), NASA, 2013.

[50] M. J. Miller, B. A. Steinfeldt, and R. D. Braun, "Supersonic Inflatable Aerodynamic Decelerators for use on Sounding Rocket Payloads," in *AIAA Atmospheric Flight Mechanics Conference*, no. January, (National Harbor, Maryland), AIAA, 2014.

[51] C. H. Jenkins, *Gossamer Spacecraft: Membrane And Inflatable Structures Technology For Space Applications*. Reston, Virginia: AIAA, 1st ed., 2001.

[52] R. A. Dillman, S. J. Hughes, R. J. Bodkin, and Others, "Flight Performance of the Inflatable Reentry Vehicle Experiment II," tech. rep., NASA, 2010.

[53] S. Dutta, "Fracture toughness and reliability in high-temperature structural ceramics and composites: Prospects and challenges for the 21st century," *Bulletin of Materials Science*, vol. 24, no. 2, pp. 117–120, 2001.

[54] R. Freeland, G. Bilyeu, G. Veal, and M. Mikulas, "Inflatable deployable space structures technology summary," in *49th International Astronautical Congress*, (Melbourne), IAF, 1998.

[55] B. P. Smith, C. L. Tanner, M. Mahzari, and Others, "A Historical Review of Inflatable Aerodynamic Decelerator Technology Development," in *Aerospace Conference 2010*, (Big Sky, MT), pp. 1–18, IEEE, 2010.

[56] D. Jurewicz, G. Brown, L. Lichodziejewski, and Others, "Design and Development of Inflatable Aeroshell Structure for IRVE-3," in *21st AIAA Aerodynamic Decelerator Systems Technology Conference and Seminar*, no. May, (Dublin), AIAA, 2011.

[57] P. Lu, "Predictor-Corrector Entry Guidance for Low Lifting Vehicles," in *AIAA Guidance, Navigation and Control Conference and Exhibit*, no. August, (Hilton Head), AIAA, 2007.

[58] A. M. D. Cianciolo, J. L. Davis, D. R. Komar, and Others, "Entry, Descent, and Landing Systems Analysis Study: Phase 1 Report," tech. rep., NASA, 2010.

[59] S. Dutta and R. D. Braun, "Preliminary statistical trajectory and atmosphere reconstruction of MSL entry, descent, and landing," *Advances in the Astronautical Sciences*, vol. 148, pp. 1595–1612, 2013.

[60] S. a. Whitmore, R. J. Davis, and J. M. Fife, "In-flight demonstration of a Real-Time Flush Airdata Sensing (RT-FADS) system," no. October, 1995.

[61] H. L. Justh, C. G. Justus, and H. S. Ramey, "The next generation of Mars-GRAM and its role in the Autonomous Aerobraking Development Plan," *Advances in the Astronautical Sciences*, vol. 142, no. 1, pp. 533–540, 2012.

[62] A. B. Bailey, "Sphere drag measurements in an aeroballistics range at high velocities and low Reynolds numbers," tech. rep., Arnold Engineering Development Center, Air Force Systems Command, Arnold Air Force Station, Tennessee, 1966.

[63] J. D. Anderson Jr., *Fundamentals of Aerodynamics*. McGraw-Hill Education, 4th ed., 2007.

[64] R. N. Cox and L. F. Crabtree, *Elements of hypersonic aerodynamics*. New York City: Academic Press, 1965.

[65] J. J. Bertin, *Hypersonic Aerothermodynamics*. Washington, D.C.: American Institute of Aeronautics and Astronautics, second ed., 1994.

[66] J. W. Cleary and C. E. Duller, "Effects of angle of attack and bluntness on the hypersonic flow over a 15 degrees semiapex cone in helium," tech. rep., NASA Ames Research Center, Moffett Field, California, 1970.

[67] V. I. Stevens, "Hypersonic Research Facilities at the Ames Aeronautical Laboratory," *Journal of Applied Physics*, vol. 21, pp. 1150–1155, Apr. 1950.

[68] J. J. Bertin, "The effect of protuberances, cavities, and angle of attack on the wind-tunnel pressure and heat-transfer distribution for the Apollo command module," tech. rep., NASA, Houston, Texas, 1966.

[69] K. Yamada, Y. Kimura, D. Akita, and Others, "Study on Low-ballistic-coefficient Atmospheric-entry Technology Using Flexible Aeroshell," *Transactions of the Japan Society for Aeronautical and Space Sciences, Space Technology Japan*, vol. 7, no. 26, 2009.

[70] I. G. Clark, *Aerodynamic Design, Analysis, And Validation Of A Supersonic Inflatable Decelerator Aerodynamic Design.* PhD thesis, Georgia Institute of Technology, 2009.

A Verification and validation

A.1 Trajectory

A.1.1 Discretisation error

Due to the use of a discrete time step an error relative to the real solution is induced. By testing the tool with the same initial conditions using different time meshes the difference between the solutions can be analysed. When the smallest time step is assumed to be exact, the error of the larger time steps can be expressed relative to that. This relative error is shown in Figure A.1. Please also note these errors are calculated running the tool without active control.

Two conclusions can be drawn from this. First the error decreases quadratically with decreasing time step. This means that the system converges. Secondly the error is smaller than $1\,[m]$ for a time step smaller than $0.3\,[s]$. This error is negligible compared to the error that will be induced by the assumptions that were made in Section 6.1.1.

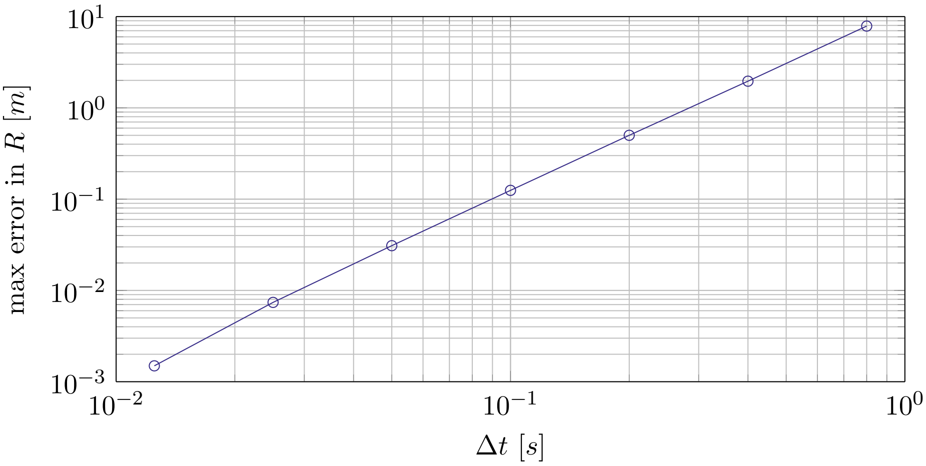

Figure A.1: Discretisation error in radius ($\mathbf{R}$) after one pass through the atmosphere for initial position $[-4\ 143\ 775, 10 \cdot R_m]\,[m]$ and initial velocity $[0, -7167.9]\,[m \cdot s^{-1}]$ at $\alpha = -10\,[deg]$ for the rigid shape

A.1.2 Verification through comparison with Kepler orbit

In this section the results from the numerical simulation, which is usually only used in atmosphere, is compared to a Kepler orbit. For this comparison the density is assumed to be zero, or in other words, it is assumed that there is no atmosphere. This comparison is done for different values of Δt. The error for each Δt is shown in Figure A.2.

The figure shows the error is between 15 and 5 for Δt between 1 and 0.01. The error decreases, but seems to tend to a non-zero constant value. The method used for numerical simulation is thus convergent, but has a small offset from the exact solution. This error is however so small it can easily be accepted. It should also be noted that the numerical simulation is never ran longer than 2000 seconds during the entire mission trajectory calculation. The error calculated here is thus much larger than the error in the actual calculations will be.

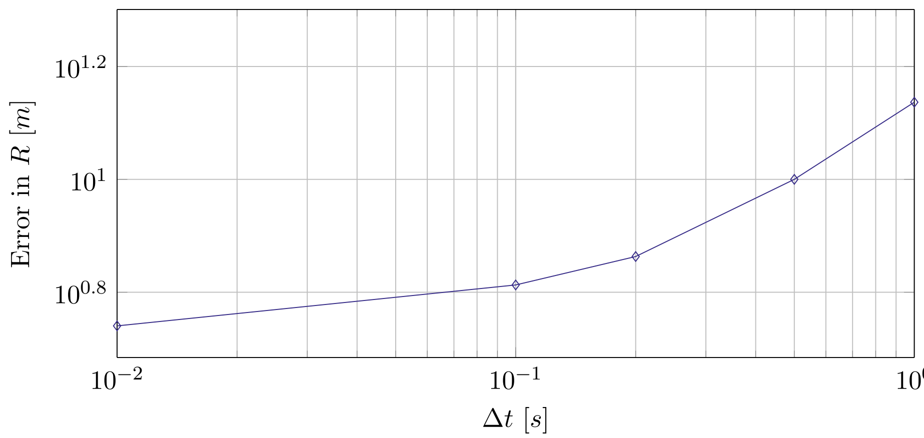

Figure A.2: Error compared to a Kepler orbit after 50 005 $[s]$ for initial position $[-4\ 143\ 775, 10 \cdot R_m]\,[m]$ and initial velocity $[0, -7167.9]\,[m \cdot s^{-1}]$ at $\alpha = -10\,[deg]$ for the shape of the rigid concept

A.1.3 Validation

Validation for a mission as unique as this one is difficult as no reference data is available. Testing is thus the only method to do any validation of the model. Because of budget and time constraints of the conceptual design, testing is not possible. Engineering gut feeling is now the only way to get an idea of the correctness of the model. No final conclusions can be drawn from this, and thus no conclusion will be drawn.

A.2 Aerodynamics

After the model construction verification was carried out to determine whether the model correctly implemented the calculations of the modified Newtonian method. This was done by placing two triangular surface elements in a flow. First at an angle and secondly normal to the flow. The model outputs were verified by also calculating the results by hand.

Following the verification process the model was validated using experimental values of different parameters. Each separate validation case will be treated here.

A.2.1 C_D-validation against experimental drag of a sphere

For the first model validation case a comparison was made the between the C_D-value of a sphere in hypersonic flow that were computed by the model and as found in an experiment. It was found that for hypersonic Mach numbers the experimental C_D-value of a sphere is 0.92 [62–64]. When computing C_D numerically with the modified Newtonian method using more than 10 000 surface elements produces $C_D = 0.916\,[-]$, which coincides with a discrepancy of 0.5% of the experimental value. Since the accuracy of the experimental data is approximately ±1.5% [62] this discrepancy falls within the confidence interval of the measurements.

A.2.2 C_p-validation against experimental data of a sharp cone

Following the C_D-validation for blunt bodies presented in the previous section now C_p-validation will be carried out for sharp bodies. This is performed by comparing C_p at select points on the surface of a cone with half-cone angle θ of 15 $[deg]$. The experimental data was collected for $M = 14.9\,[-]$ and $\kappa = \frac{5}{3}\,[-]$ [65, 66]. Figure A.4 shows the data points that were collected for angles of attack $\alpha = 10\,[deg]$ and $\alpha = 20\,[deg]$ in Figure A.4a and A.4b respectively. On the x-axis the variable β_{cone} is used. This quantity refers to the local cross-sectional surface rotation with respect to an axis that is defined positive in the positive z-direction. Figure A.3 showcases this concept more clearly. Normally the domain of β_{cone} lies between $0\,[deg]$ and $360\,[deg]$, but because the cone is symmetrical only half of the cone surface is plotted here. Furthermore, since the cone in question is a sharp cone with a constant semi-cone angle the C_p-distribution is constant along the cone surface for constant β_{cone}. As can be seen in Figures A.4a and A.4b the modified Newtonian method is the most accurate around $\beta_{cone} = 90\,[deg]$.

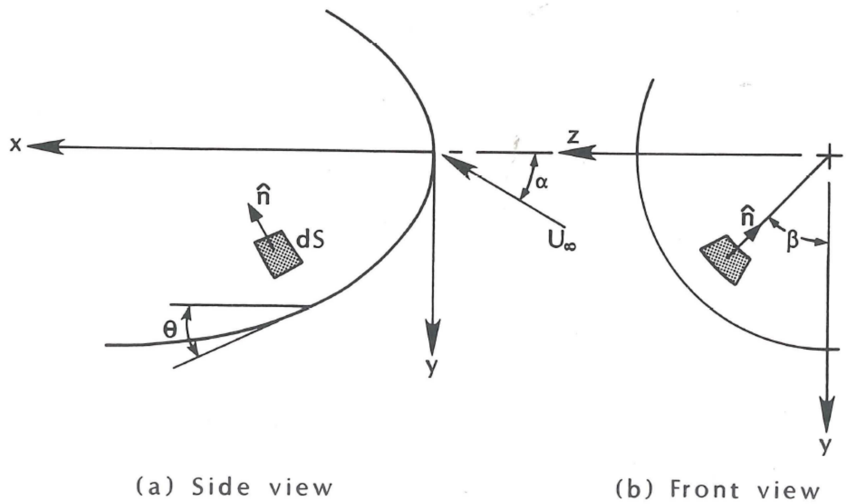

Figure A.3: Definition of β_{cone} [65]

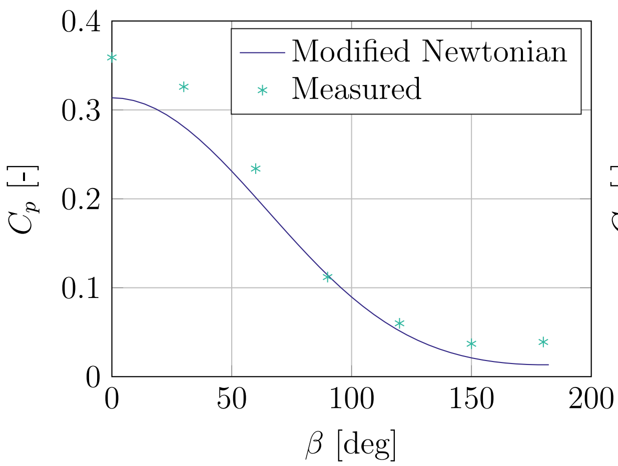

(a) $\alpha = 10\,[deg]$

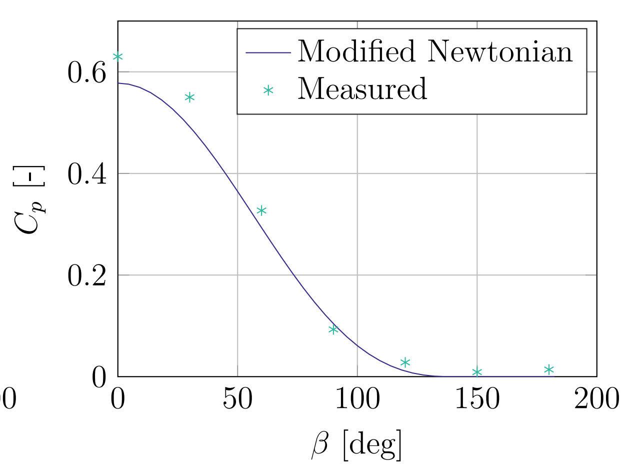

(b) $\alpha = 20\,[deg]$

Figure A.4: Comparisons between experimental and numerical pressure coefficients

A.2.3 C_D-validation against experimental data of a sharp cone

Stevens found that for a sharp cone-cylinder with half-cone angle θ of $30\,[deg]$, $C_D = 0.58\,[-]$ in an air-stream of Mach 8 where angle of attack α and sideslip angle β are zero [63, 67]. The numerical model predicts for this case that $C_D = 0.456\,[deg]$, which coincides with a discrepancy of 21.4% of the experimental value. This is in line with the results of Section A.2.2 where the C_p's predicted by the numerical model were smaller than the experimental values of a sharp cone.

A.2.4 C_p-validation against experimental data of the Apollo re-entry capsule

The data points in Figure A.5 represent pressure coefficients measured at various locations of one of the two axisymmetric axes [68]. The quantity shown on the x-axis is defined in Figure A.6. As can be seen in Figure A.5 the numerical model is most accurate around the centre of the capsule. As the distance to the centreline increases, so does the discrepancy between the experimental and numerical values.

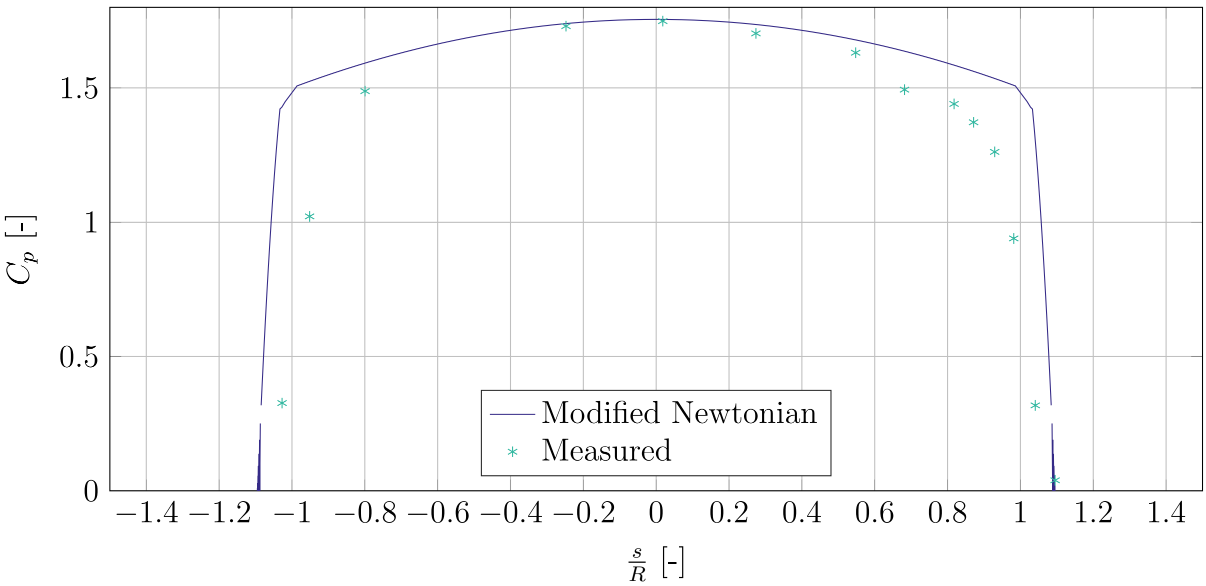

Figure A.5: Comparison between experimental and numerical pressure coefficients for the Apollo re-entry capsule

A.2.5 Maximum heat flux validation against experimental data of the IRVE 3 vehicle

Dillman et al. observed that the maximum heat flux on the Inflatable Re-entry Vehicle Experiment (IRVE) 3 was $14.4\,[W \cdot cm^{-2}]$ during re-entry at an altitude of $50\,[km]$ and Mach 7.0 [49]. The maximum heat flux computed by the numerical tool in the stagnation point for these flow conditions is $11.7\,[W \cdot cm^{-2}]$. This is equal to 81.0% of the experimental value. Thus a discrepancy of 19.0% is present between the experimental and numerical maximum heat fluxes.

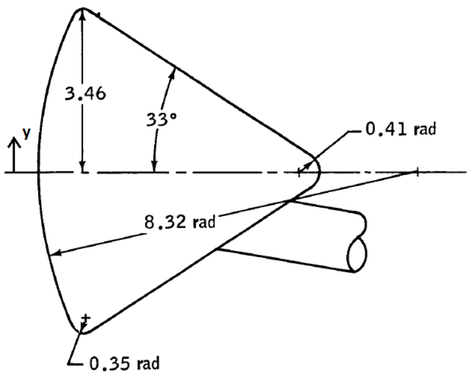

Figure A.6: Definition of unit on the horizontal axis of Figure A.5 [68]

A.2.6 Conclusions after the validation procedure

From the previous sections it can be seen that the accuracy of the modified Newtonian method varies between geometries. The C_D predicted in Section A.2.1 is accurate to within 1% of the experimental value, whereas the accuracy of the C_ps in Section A.2.2 varied over the cone surface. This discrepancy was also seen in Section A.2.3, where the difference between the numerical and experimental C_D was 21.4%, and again for the Apollo capsule in Section A.2.4. These discrepancies are expected, as the Modified Newtonian flow theory is only valid when pressure drag dominates the total drag. At lower incidence angles with the flow, this situation no longer holds. The estimated pressure coefficients are therefore incorrect at high incidence angles. This can be seen around the edges of the Apollo re-entry capsule and on the surface of the sharp cone, where the discrepancies are largest.

After judging the accuracy shown in Figures A.4 and A.5 it was determined that the accuracy of the modified Newtonian method is adequate for the conceptual and preliminary design phases, since the body will be a blunt body at low to moderate incidence angles to the flow. The body therefore operates within the useful range of modified Newtonian flow theory. The model for the maximum heat flux found on a body was validated in Section A.2.5. It was observed that a discrepancy of 19.0% was present between the numerical and experimental maximum heat fluxes. Possible causes for this discrepancy lie in the difference between the atmospheric conditions at the time of the measurement during the IRVE mission and the international standard atmosphere and in the fact that the theory used is an empirical method which is not an exact expression for the heat flux derived from governing flow equations. After consideration this was deemed to be acceptable for conceptual and preliminary design.

A.3 Thermodynamics

The thermal model has been built as described in Section 6.1.4 according to the method explained by Smith et al. [4]. Before the model can be used for the design it has to undergo the verification and validation process. In the first part the verification is done by comparing the analytical and numerical solutions of a copper block. In the second part two papers by Del Corso et al. are used to validate the developed model with experimental data [1, 2]. The last part will explain the differences that were found in the verification and validation.

A.3.1 Verification of the model using a solid copper block

For the verification of the thermal model the analytical solution (Equation (17)) provided by both Smith and Holman is used [4, 37]. Here T_1 is the wall temperature at $t = 0$ and T_2 the temperature at a certain $t\,[s]$ and x.

$$T_2 - T_1 = \frac{2\dot{q}\sqrt{\alpha_d t/\pi}}{kA} \exp\left(\frac{-x^2}{4\alpha_d t}\right) - \frac{\dot{q}x}{kA}\left(1 - erf\frac{x}{2\sqrt{\alpha_d t}}\right) \tag{17}$$

Figure A.7 shows a semi-infinite $0.5\,[m]$ thick copper block subjected to a constant heat flux of $30\,[W \cdot cm^{-2}]$. The block initially has a uniform temperature of $20\,[°C]$. The error at the surface ($x = 0.00\,[m]$), in the middle ($x = 0.25\,[m]$) and at the back ($x = 0.50\,[m]$) between the analytical and numerical solution are 1.55%, 4.32% and 15.92% respectively.

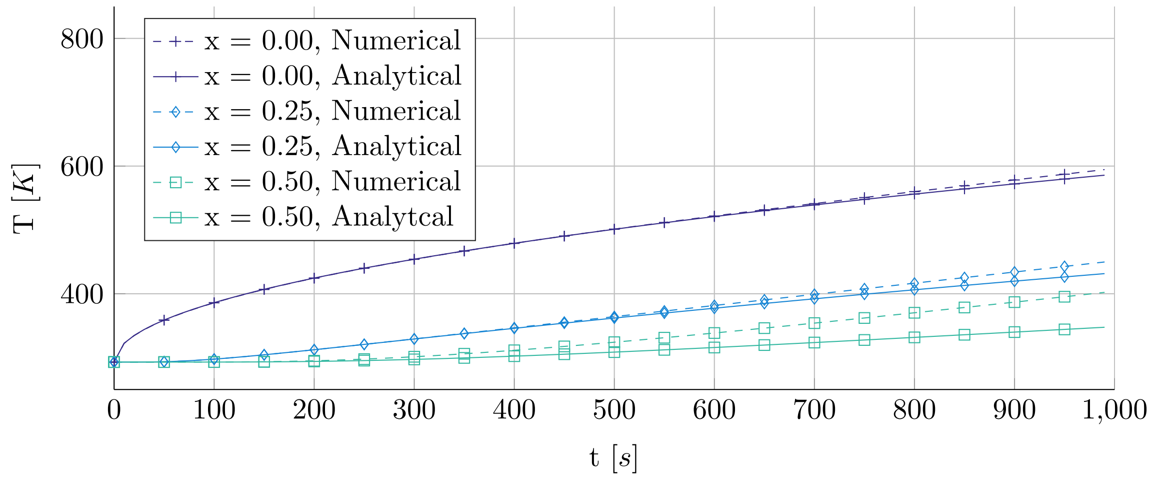

Figure A.7: Comparison of analytical and numerical solution by applying a constant heat flux for $1000\,[s]$ on a copper block with a $0.5\,[m]$ thickness.

A.3.2 Validation against experimental data

As mentioned earlier two papers by Del Corso et al. provide the experimental data [1, 2]. The four lay-ups shown in Figure A.8 have been tested to validate the thermal model. Note that the references do not provide the experimental data for lay-up 1, but give the result of the thermal model they have used. For lay-up 2 and 3 data from both NASA's model and experiments have been provided.

All lay-ups have been compared and validated. Before the model is validated all the contact resistances had to be adjusted such that they match the experimental data as was already mentioned in Section 6.1.4. The reason for this is that it is not possible to determine this value analytically. Lay-up 2 is used to serve as an example of this validation and has been subjected to a heat flux of $6.2\,[W \cdot cm^{-2}]$ for $90\,[s]$. Between every layer a thermocouple was placed during the experiment. With four layers that means that there were three thermocouples. Figure A.9 shows the result of this validation. It is clear that the model works very well during the application of the heat flux in the first $90\,[s]$. The average error for thermocouples TC1, TC2 and TC3 are 3.9%, 3.0% and 4.8%

Nextel AF-14	0.356 mm
Pyrogel 6650	6.350 mm
Kapton	0.025 mm
Kapton	0.025 mm

Lay-up 1

Nextel BF-20	0.508 mm
Pyrogel 6650	6.350 mm
Kapton	0.025 mm
Kapton	0.025 mm

Lay-up 2

Nextel BF-20	0.508 mm
Nextel BF-20	0.508 mm
Pyrogel 3350	2.997 mm
Pyrogel 3350	2.997 mm
Kapton	0.013 mm
Kapton	0.013 mm

Lay-up 3

Nicalon	0.508 mm
Nicalon	0.508 mm
Pyrogel 3350	2.997 mm
Pyrogel 3350	2.997 mm
Kapton	0.013 mm
Kapton	0.013 mm

Lay-up 4

Figure A.8: The four lay-ups used to test the thermal model against experimental data

respectively. However, during the cooling down of the lay-up the error rapidly increases to 60.1%, 66.0% and 68.9%.

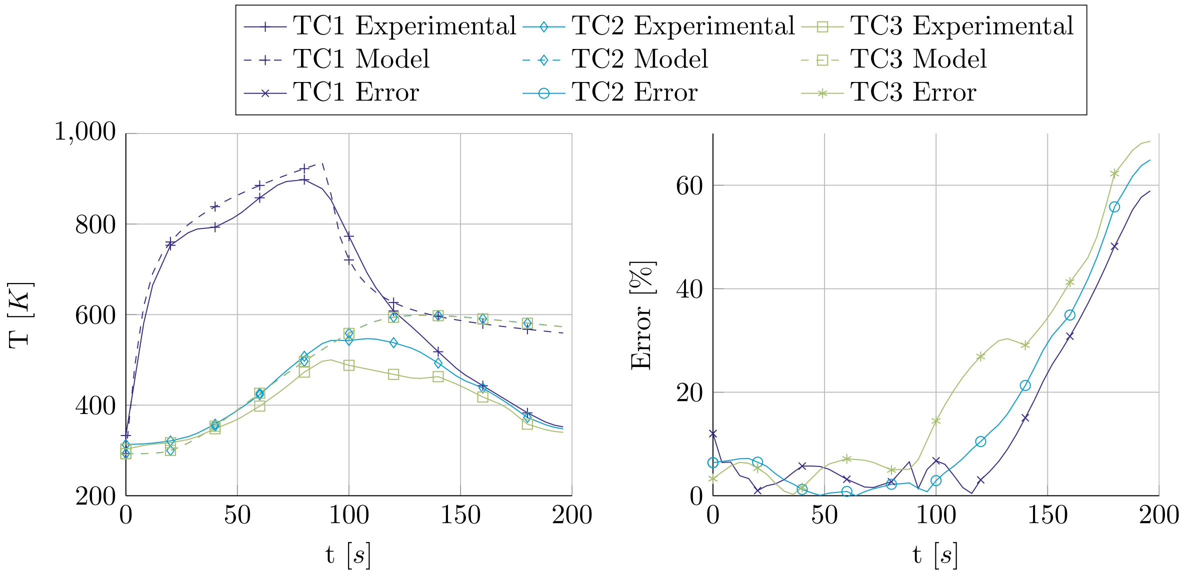

Figure A.9: Thermal model compared to experimental data at three locations

Table A.1 shows the result of all the lay-ups. The thermal model has been compared to NASA's model, the experimental data where possible. For reference NASA's model has been compared to the experimental data to show the performance of the developed thermal model. Note that the maximum error is the average of the maximum errors of the thermocouples. Also for every lay-up the contact resistance must be tweaked in order to match the experimental data. The number used in tweaking is characteristic for the two layers it separates. The table shows that the thermal model is accurate to about 15 to 20%. The fourth layer with Nicalon™ has a high average error, this is due to the relatively high errors in the Pyrogel® and kapton layers. The temperature in the Nicalon™ layer is correctly modelled with the same 15 to 20% accuracy. NASA's model performs better with an accuracy of about 10 to 15%. Not visible in the table, but visible in Figure A.9 is that larger errors in the cooling down phases are overestimates of the temperatures.

Table A.1: Comparison of thermal model, NASA's model and experimental data

	Lay-up 1	Lay-up 2	Lay-up 3	Lay-up 4
Thermal model vs. experimental data				
Avg. error	-	18.28%	16.45%	30.87%
Max. error	-	65.03%	70.90%	56.25%
Avg. error during heat flux	-	3.91%	17.75%	31.37%
Avg. error during cooling down	-	30.05%	8.67%	27.52%
Thermal model vs. NASA's model				
Avg. error	6.72%	10.88%	17.85%	-
Max. error	22.54%	22.42%	55.56%	-
Avg. error during heat flux	7.26%	10.48%	18.19%	-
Avg. error during cooling down	6.62%	11.20%	15.84%	-
NASA's model vs. experimental data				
Avg. error	-	13.79%	10.69%	-
Max. error	-	43.37%	34.22%	-
Avg. error during heat flux	-	8.43%	10.28%	-
Avg. error during cooling down	-	18.18%	13.15%	-

A.3.3 Conclusions after the verification and validation procedure

The verification showed that the numerical solution starts to diverge as the error increases with time and depth. It is expected that this is a result of rounding errors that get multiplied every time step in the discretisation scheme. The reason for this is that refining the mesh produces the same errors. There are two reasons why this is not a significant problem for the design problem. The first is that the TPS shall be a hundred times thinner. The second is that the length of the aerocapture and entry phases are approximately 800 $[s]$, which is within the verified duration.

The validation shows that the thermal model, with an accuracy of 15 to 20%, performs slightly worse than NASA's model with an accuracy of 10 to 15%. It is assumed that errors under 10% should be completely acceptable for a low fidelity model. Larger error should be contributed to the difficulties in contact resistance modelling. When increasing the amount of layers it is increasingly difficult to predict the contact resistance, something Del Corso also experienced in NASA's model [1]. This especially gets worse when there is no heat applied and the lay-up converges to an equilibrium state. For the purpose of the design of the lay-up for an inflatable heat shield this is not a problem, as the heat shield has enough time to cool down in the parking orbit after the aerocapture before it starts its final entry. For these reasons the thermal model is considered validated and safe to use for design while keeping its accuracy in mind.

A.4 Structure

A.4.1 Force estimation method

Verification for the simplified truss model is performed on the basis of simplified load cases. Significant errors were not observed and remained below 3% for various geometries and half cone angles with a minimum of five toroids. The small verification errors followed from the discrete application of the dynamic pressure. Taking the discrete application into account as well the errors disappear.

Validation is performed for the inner root section of the inflatable on the basis of the results presented by Lindell et al. [38]. Lindell presents results for the root section of the first IRVE design by means of FEM analysis and a set of closed-form equations valid at the root of the inflatable. Table A.2 presents the results of this validation effort. Errors considering solely the 2D model are significant causing unacceptable results for the basis of structural analysis. These errors can be attributed to the neglection of the 3D effects.

In the real, 3D, structure lateral loads can be carried in circumferential direction. In the 2D model these loads are however carried through the root section of the inflatable causing steep increases in the loadings of the restraint wrap. This explains the errors as observed in Table A.2. A second model taking into account these 3D effects shows better results. Lateral loads are assumed to be carried in circumferential direction at each of the outside nodes.

Table A.2: Verification data of the inflatable structural model

Method	FEM [38]	Closed form [38]	Truss model 2D	Truss model 3D
Spar $[\mathbf{kN} \cdot \mathbf{m^{-1}}]$	4.69	4.57(-2.6%)	-4.59(2.2%)	3.97(15.4%)
Front restraint wrap $[\mathbf{kN} \cdot \mathbf{m^{-1}}]$	3.85	4.34(12.7%)	24.1(455%)	4.30(11.7%)
Aft restraint wrap $[\mathbf{kN} \cdot \mathbf{m^{-1}}]$	5.03	4.34(-13.6%)	-64.4(1584%)	4.72(-6.16%)

The results of Table A.2 show that the 3D model provides a decent estimate of the structural loads through the inflatable structure. This is in contrast to the closed form equations as provided by Lindell [38], which allow estimates only at the root of the inflatable.

It is important to consider that actual local loading may be significantly higher and should be properly accounted for in further detailed design phases. For now this is accounted for by the use of contingency and safety factors. Moreover, it is assumed that the dynamic pressure acts equally distributed over the inflatable surface. This same assumption is used in the FEM validation data. This distribution is, however, only a rough estimation of reality. Figure A.10 shows the predicted pressure distribution over the CIA for the final design. It can be noted that the actual aerodynamic pressure is significantly higher at the centre of pressure. The highest pressures are still observed within the rigid part of the centre body. Local loads are higher and should be accounted for by the use of appropriate safety factors.

A.4.2 Mass estimation method

In order to verify that the mass estimation method described in Reference [40] has been correctly implemented, results for the nine sample cases presented on page 16 of Reference [40] have been checked. These nine sample cases were implemented by choosing the input

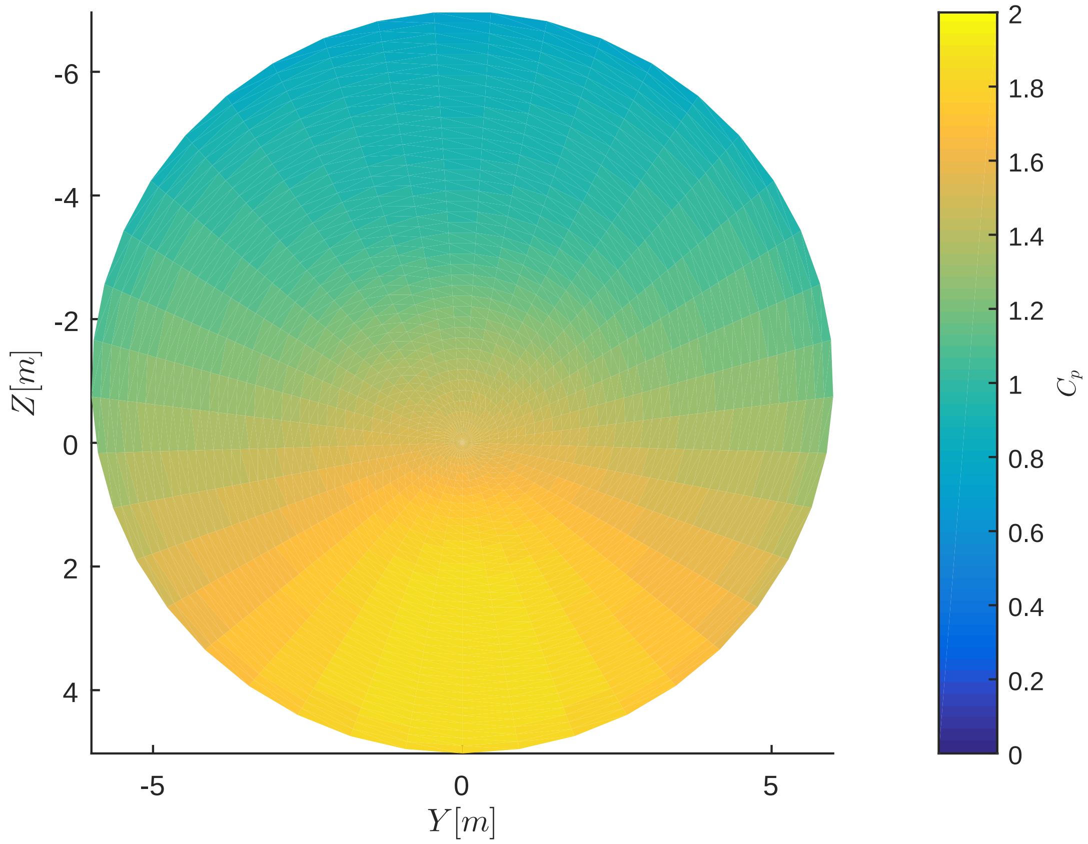

Figure A.10: Pressure distribution at the trimmed angle of attack

parameters as given in tabular form (Tables 4 and 5) on page 16 of Reference [40] and the output parameters, primarily component masses and geometric quantities, were compared. A maximum error of 3% in terms of total mass was obtained; a maximum error of 2% in component masses. These errors are deemed sufficiently small to verify successful implementation of the mass estimation method.

Validation is performed indirectly: the method [40] has been applied in the entry, descent & landing system analysis project [58], where it was shown to yield results conforming well to the outcomes of a high-fidelity FEM. The used FEM is a validated tool [58] and thereby the method outlined in Reference [40] has been validated through comparison with a high-fidelity validated model. Moreover, the expression for minimum inflation pressure obtained by Samareh has been found to be in correspondence with Yamada et al. [69], Clark [70] and Brown [39].

B Thermal properties

In this section a variety of possible TPS materials with their thermal properties are listed below in Table B.1 [1–6].

Table B.1: Flexible Thermal Protection System material properties

Material	**k** $\left[\frac{\mathbf{W}}{\mathbf{m \cdot K}}\right]$	ρ $\left[\frac{\mathbf{kg}}{\mathbf{m^3}}\right]$	$\mathbf{c_p}$ $\left[\frac{\mathbf{J}}{\mathbf{kg \cdot K}}\right]$	$\mathbf{T_{max}}$ $[\mathbf{K}]$	ε $[-]$
Coating					
Viton	0.202	1842	1654	N/A	0.85
Heat Barrier					
Hi-Nicalon™	2.4	2900	1200	2073	0.93
Nextel AF14	0.150	858	1050	1373	0.443
Nextel BF20	0.146	1362	1130	1643	0.443
Nextel XN513	0.148	1151	1090	1673	0.443
Refrasil C1554-48	0.865	924	1172	1533	0.7
Refrasil UC100-28	0.865	890	1172	1255	0.2
Hexcel 282 Carbon	0.5	891	1000	N/A	0.9
Insulator					
Pyrogel® 6650	0.030	110	1046	923	-
Pyrogel® 3350	0.0248	170	1046.0	1373	-
Pyrogel® 5401	0.0248	170	1046	N/A	-
Refrasil 1800	0.085	156	1172	1255	-
Refrasil 2000	0.095	180	1172	1366	-
KFA 5	0.25	98	1250	1473	-
Nomex	0.035	384	1465	N/A	-
Gas Barrier					
Kapton	0.12	1468	1022	673	-
Structural Layer					
Upilex	0.29	1470	1130	773	-
Kevlar	0.04	1440	1420	443	-
Vectran	0.37	1400	1259	N/A	-
PBO Zylon®	20	1540	900	673	-

C Atmospheric model

In this appendix the data from the atmospheric model is presented. The trajectory through the atmosphere is largely influenced by the densities (ρ), and the temperature (T) plays a role in the heat flux and Mach number. Mars-GRAM is used to calculate the temperature and density at different heights, longitudes and latitudes. The properties are acquired at one point in time, leading to errors since the atmosphere changes over time. However, discrepancies are covered by testing the capability of the control system to cope with a scaled density throughout the atmosphere.

The data that is of most importance is the variation of density and temperature with height. These relations are shown in Figure C.1.

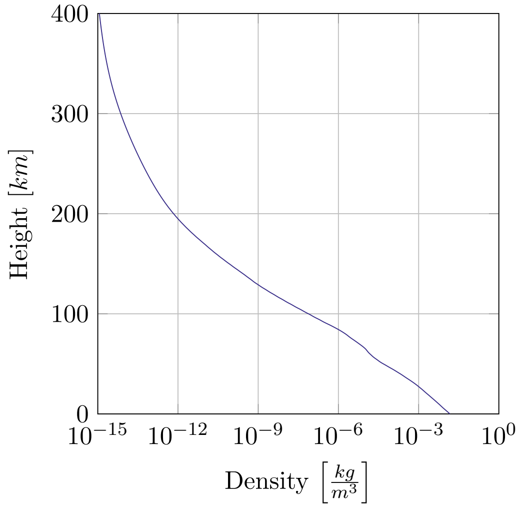

(a) The atmospheric density

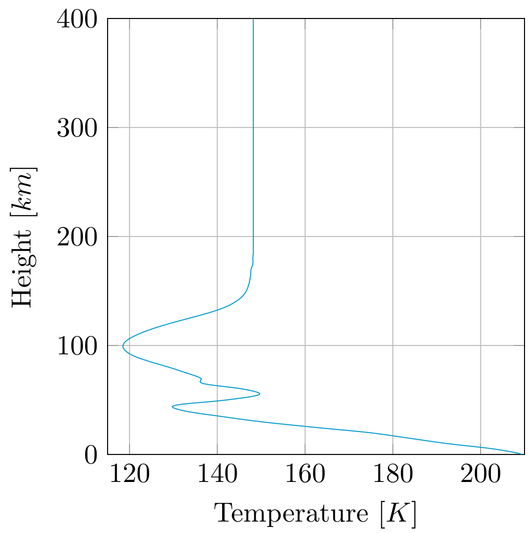

(b) The atmospheric temperature

Figure C.1: The atmospheric properties for different heights

Changes in atmospheric properties also occur across the different longitudes and latitudes. These changes are not used in the analysis of the trajectory through the atmosphere and should be considered in further design stages. The differences in density in lower parts of the atmosphere (lower than approximately 100 $[km]$) can be 30% between the highest and lowest density found at a latitude of 0 $[deg]$. The density at four different heights is portrayed in Figure C.2. In order to reduce the maximum error, in the trajectory calculation the latitude is used for which the density profile most closely mimics the average density over the longitudes. This longitude is chosen to be 180 $[deg]$.

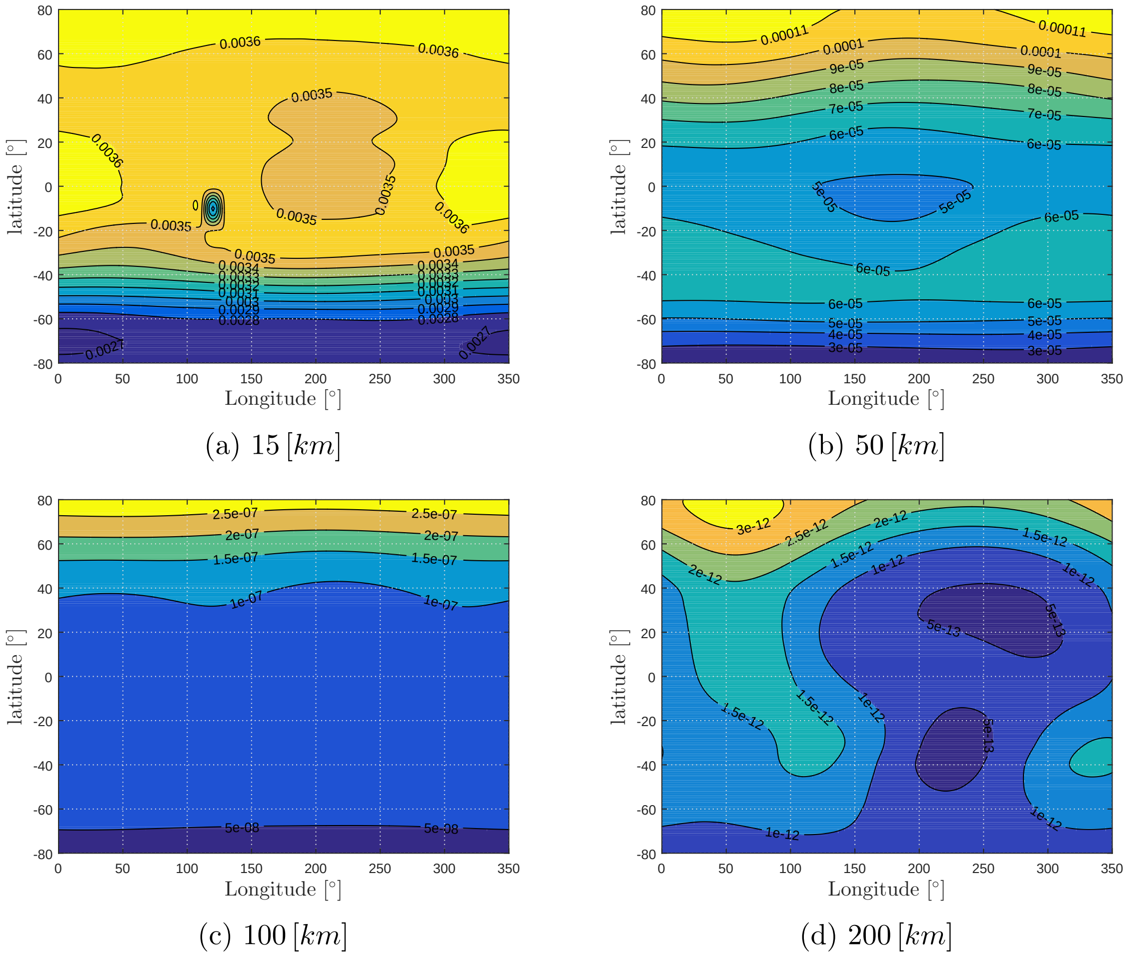

(a) 15 $[km]$ (b) 50 $[km]$

(c) 100 $[km]$ (d) 200 $[km]$

Figure C.2: Atmospheric density as a function of latitude and longitude for different altitudes